THÈSE

En vue de l'obtention du

DOCTORAT DE L'UNIVERSITÉ DE TOULOUSE

Délivré par :

Institut National Polytechnique de Toulouse (INP Toulouse)

Discipline ou spécialité :

Dynamique des fluides

Présentée et soutenue par :

M. SUBHANDU RAWAT

le mercredi 10 décembre 2014

Titre :

DYNAMIQUE COHERENTE DES MOUVEMENTS TURBULENTS A GRANDE ECHELLE

Ecole doctorale :

Mécanique, Energétique, Génie civil, Procédés (MEGeP)

Unité de recherche :

Institut de Mécanique des Fluides de Toulouse (I.M.F.T.)

Directeur(s) de Thèse :

M. CARLO COSSU

M. FRANCOIS RINCON

Rapporteurs :

Mme LAURETTE TUCKERMAN, ESPCI PARISTECH

M. UWE EHRENSTEIN, AIX-MARSEILLE UNIVERSITE

Membre(s) du jury :

Mme LAURETTE TUCKERMAN, ESPCI PARISTECH, Président

M. CARLO COSSU, INP TOULOUSE, Membre

M. FRANCOIS RINCON, CNRS TOULOUSE, Membre

M. YOHANN DUGUET, LIMSI, Membre

Contents

Chapter 1

Introduction

1.1 Streaky motions in transitional wall-bounded shear flows flows

Bypass transition. The 'classical' scenario of transition to turbulence in a number of flows is understood as the onset of a linear instability of the basic flow followed by secondary instabilities and then by transition. For instance in flat plate boundary layers, the primary instability is in the form of 2D Tollmien-Schlichting waves which are exponentially amplified for Reynolds numbers larger than the critical Re_c. However, it has long been known that in the presence of high levels of perturbations, such as e.g. free-stream turbulence, transition occurs below the critical Reynolds number, bypassing the onset of the primary instability. In this transition scenario, called 'bypass transition' the prominent feature of the flow is the presence of 'streamwise streaks' in smoke visualisations of the flow, as shown in figure 1.1 (see e.g. Kendall, 1985; Matsubara & Alfredsson, 2001). The streaks consist of spanwise alternating regions of high and low streamwise velocity which are elongated in the streamwise direction. In transitional flows their characteristic spanwise wavelength is of the order of the shear thickness (the boundary layer thickness in boundary layer flows, the channel half-width in plane channels, etc.) .

Similar phenomena are observed in a number of other wall-bounded shear flows such as the pressure-driven channel flow where transition is observed for values of the Reynolds number ($\mathrm{Re} \approx 1000$, Patel & Head, 1969) much smaller than the critical Reynolds number ($Re_c = 5772$, Orszag, 1971) at which Tollmien-Schichting waves become linearly unstable. In the case of plane Couette and of the Hagen-Poiseuille flow in a pipe, transition to turbulence is observed despite the linear stability of the basic flow. Also in this case streaky structures are observed in the transitional regime. These scenarios of transition to turbulence have long remained basically unexplained. A particularly intriguing issue, for instance, is that critical modes are spanwise uniform with a finite wavelength in the streamwise direction, while the observed streaks have exactly the opposed feature: they are quasi-uniform in the streamwise direction but periodic in the spanwise direction. In the next section we will explain how the solution of this apparent contradiction is now understood.

The lift-up effect. In shear flows the fluid in a region of the flow (e.g. near the wall in Poiseuille flow) moves at a lower speed than the fluid in the other region (e.g. the channel centre in Poiseuille flow). If low-energy spanwise periodic counter-rotating streamwise vortices are introduced in the flow, they redistribute the streamwise velocity by carrying low velocity fluid in the high-speed fluid region and high velocity fluid in the low speed region. This redistribution of streamwise momentum, called 'lift-up effect' leads to the formation of spanwise periodic regions of high and low speed streamwise velocity, i.e. the streamwise streaks (Moffatt, 1967; Ellingsen & Palm, 1975; Landahl, 1980, 1990). The liftup effect has been shown to be associated with the nonnormal na-

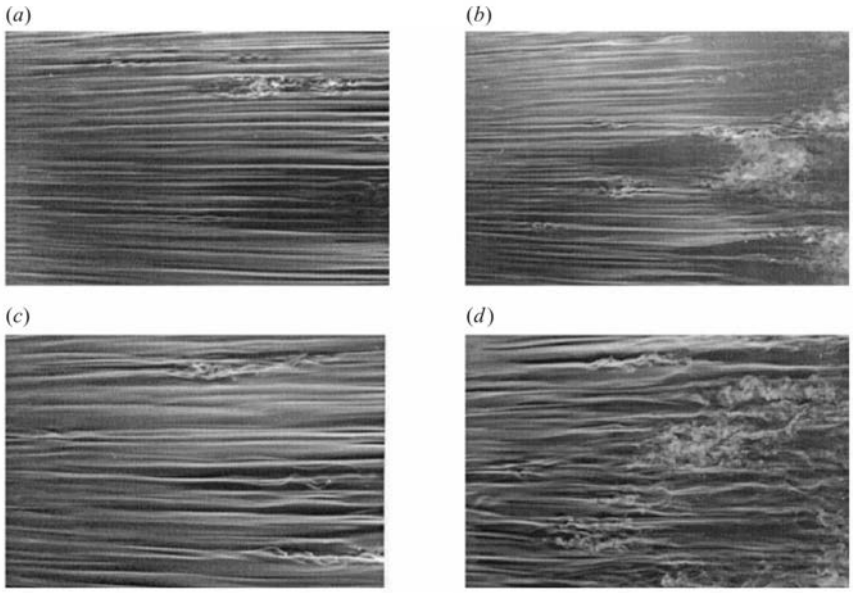

Figure 1.1: Smoke visualization of streaks in transition under the high-level free-stream turbulence in a boundary layer. The level of free-stream turbulence increases in panels *a* to *d* (from Matsubara & Alfredsson, 2001).

ture of the linearized Navier-Stokes operator and optimal perturbations maximizing the energy growth of the streaks have been computed for virtually all the canonical shear flows in the initial value problem (Butler & Farrell, 1992; Reddy & Henningson, 1993; Trefethen *et al.*, 1993; Schmid & Henningson, 1994; Hristova *et al.*, 2002), the harmonic forcing problem (Reddy & Henningson, 1993; Reddy *et al.*, 1993; Trefethen *et al.*, 1993) and for stochastic excitation (Farrell & Ioannou, 1993*a*,*b*, 1996; Bamieh & Dahleh, 2001; Jovanović & Bamieh, 2005). The optimal input perturbations consist of streamwise vortices and the most amplified perturbations in streamwise streaks, with typical spanwise wavelengths of the order of the shear layer thickness. In the linear context the growth of the streaks is only transient as they are modally stable, but the maximum energy growths reached at finite times are proportional to the square of the Reynolds number (Gustavsson, 1991) and therefore can be very large (see e.g. Schmid & Henningson, 2001, for a summary of the main results).

Streak instability and self-sustained process. When the streaks reach sufficiently large amplitudes they become unstable to secondary perturbations via an inflectional, typically sinuous, instability (Waleffe, 1995; Reddy *et al.*, 1998; Andersson *et al.*, 2001). As this secondary instability is subcritical small finite amplitude perturbations can also develop on top of streaks of amplitude smaller than the critical one (Schoppa & Hussain, 2002; Cossu *et al.*, 2011). A key feature of the secondary (linear or nonlinear) instability is that is amplifies streamwise non-uniform perturbations in a particular streamwise waveband. The breakdown of streamwise streaks leads to the regeneration of streamwise vorticity via nonlinear mechanisms. Under particular conditions, related to the streamwise and spanwise wavelength of the perturbations and to the Reynolds number, the process can be self-sustained. This concept has been investigated by Hamilton *et al.* (1995) who studied it in a small periodic domain (the minimal flow unit of Jiménez & Moin, 1991) for plane Couette flow. The flow visualization and careful analysis of the energy associated with various Fourier modes enabled them to identify a three step process, as shown in figure 1.2. First, spanwise fluctuation in streamwise velocity i.e., streaks, are generated through the lift-up effect.

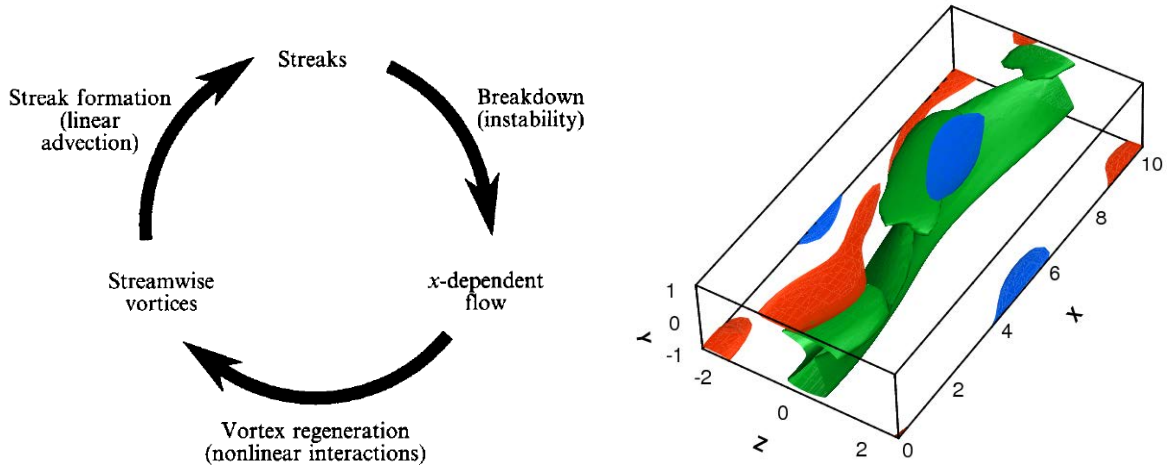

Figure 1.2: The self-sustaining mechanism (SSP). Left panel: schematic representation (from Hamilton *et al.*, 1995). Right panel: SSP-based equillibrium solution in plane Couette flow recomputed here (from Waleffe, 1997). Green is the iso-surface of streamwise velocity component at $u^+ \approx -2.9$, whereas red and blue represent iso-surface of positive and negative streamwise vorticity at $\omega_x \approx \pm 0.65 max(\omega_x)$.

This streaky flow has inflection points which results in their breakdown after the introduction of streamwise dependent disturbances. They close the regeneration cycle by showing that the non-linear interaction of the unstable eigen modes of opposite y-symmetry self-interact to reenergize streamwise vorticity and restart the whole regeneration cycle again. For the process to be self-sustained the Reynolds number and the spanwise length of the box need to be large enough to allow for sufficient energy amplification by the lift-up effect and the streamwise length needs to be large enough to allow the secondary instability to be sufficiently amplified.

Subcritical transition. From the perspective of the theory of nonlinear dynamical systems, the bypass transition is understood as a subcritical transition where the laminar solution is linearly stable but only conditionally (nonlinearly) stable and some perturbations with sufficiently large amplitude, lying outside the basin of attraction of the laminar flow, lead to other solutions. For a subcritical transition to be possible the linear stability operator evaluated on the laminar basic flow must be non-normal (Reddy & Henningson, 1993; Schmid & Henningson, 2001) and non-trivial finite amplitude solutions must exist in phase space. A notable challenge when investigating subcritical transitions is to be able to compute these non-trivial solutions around which the dynamics in phase space is organized. In subcritical instability analysis, these solutions are tracked down from the subcritical primary transition of the basic flow. This approach has for instance been used in plane Poiseuille flow by Orszag & Patera (1983) and Ehrenstein & Koch (1991). However, in flows like the plane Couette or Hagen-Poiseuille flow, such a primary instability does not exist. An ingenious solution has been, in this case, to first obtain unstable solutions in a different system and then track them to the desired flow by following a suitable path in the physical parameters space (homotopy). For instance Nagata (1990) has been able to continue unstable solutions of the centrifugally unstable Taylor-Couette flow to the plane Couette solution by continuation in the rotation parameter in the limit of vanishing curvature while Clever & Busse (1992) have reached a similar solution starting from an unstable Rayleigh-Bénard-Couette flow.

Non-trivial Navier-Stokes solutions based on the self-sustained process and transition. Based on the physics of the self-sustained process, Waleffe (1998, 2001, 2003) proposed a new technique

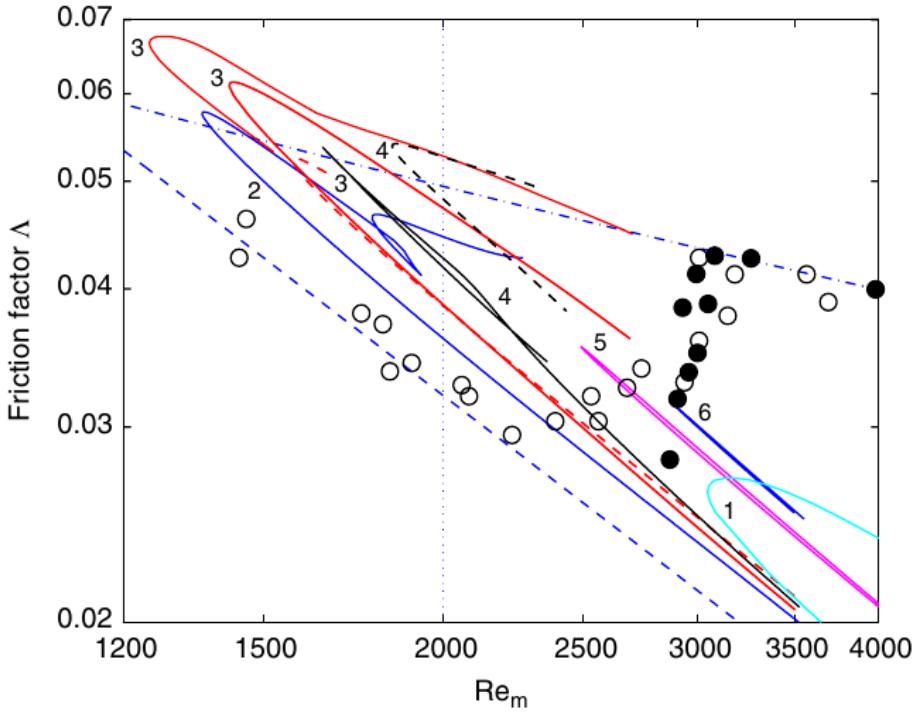

Figure 1.3: Dependence of the friction factor on the Reynolds number in Hagen-Poiseuille (pipe) flow. The solid lines correspond to travelling waves (TW) solutions and are labelled by their azimuthal wavenumber. The symbols correspond to experimental data from Schlichting (1979) (empty circles) and McKeon *et al.* (2004) (filled circles) while the dashed blue lines correspond to the drag of the laminar Poiseuille solution (lower line) and to the log-law parametrization of the mean turbulent drag. Figure reproduced from Kerswell (2005).

to compute non-trivial Navier-Stokes solutions in linearly stable laminar flows. The idea is to artificially force streamwise vortices, which induces streamwise streaks that become unstable at a critical forcing amplitude. The (linear, artificially induced) streak instability coincides with the bifurcation to a nonlinear solution which can then be tracked down to a zero forcing amplitude, where it is self-sustained. The solution typically found is a 'lower branch' solution generated via a saddle-node bifurcation at a lower Reynolds number (or negative forcing amplitude). The lower branch solution can therefore be continued in Reynolds number or in the forcing amplitude in order to find the corresponding upper branch solution. This method has proven successful to recover the Nagata-Clever-Busse solutions in plane Couette flow, and to compute non-trivial solutions in plane Poiseuille or in pipe Hagen-Poiseuille flow (Wedin & Kerswell, 2004; Kerswell, 2005; Pringle & Kerswell, 2007; Duguet *et al.*, 2008*a*).

These early investigations discovered (nonlinear) travelling wave (TW) solutions, which are steady solutions in a reference frame travelling at their phase speed. These solutions, which represent saddles in phase space, have been shown to appear at Reynolds numbers much lower than the transitional ones. Lower branch solutions are related to the laminar-turbulent transition boundary, while upper branch solutions display features consistent with the turbulent flow issued from the transition process (see figure 1.3). It was initially believed that turbulent solutions may spend a significant time in the neighbourhood of relevant NTW, but was later shown that these visits last only 10-20%, on average, of the total time (Kerswell & Tutty, 2007; Schneider *et al.*, 2007). Attention has therefore also been given to unstable periodic (in time) solutions (periodic orbits or relative periodic orbits), both for their potentially very important role in the transition process and because they might provide the missing building blocks to predict the statistics of the chaotic attractor or repellor itself (Artuso *et al.*, 1990). Periodic solutions have been computed in plane Couette (Clever & Busse, 1997; Kawahara & Kida, 2001; Viswanath, 2007), plane channel (Toh & Itano, 2003) and pipe flows (Duguet *et al.*, 2008*a*) and in the asymptotic suction boundary layer (Kreilos *et al.*, 2013). It has recently been confirmed that unstable periodic orbits and their stable and unstable manifolds play an important role in the transition to chaos of linearly stable shear flows in small spatially periodic domains, both in hydrodynamic plane Couette flow (Kreilos & Eckhardt, 2012), and in a similar problem of magnetohydrodynamic transition in Keplerian shear flow (Herault *et al.*, 2011; Riols *et al.*, 2013).

1.2 Streaky motions in turbulent wall-bounded shear flows

Streaks are observed not only in transitional regimes, but also in fully developed turbulent flows where they are ubiquitous. In fully developed wall-bounded turbulent shear flows the dynamics is ruled by the presence of two different scales of the motions: inner units are used in the (viscous) near-wall region while outer units are relevant in the outer region. In the intermediate logarithmic region, the only relevant scale is the distance from the wall. Historically, streaky motions have been first detected in the viscous layer of turbulent shear flows with dimensions scaling in inner units. The relevance of large and very large-scale structures, which scale in outer units, has only recently been recognised.

Turbulent streaky motions in the viscous layer. The flow visualizations of Kline *et al.* (1967) (see figure 1.4) revealed the near region of turbulent boundary layers is very active and is populated by streamwise streaks in a spanwise quasi-periodic pattern (see figure 1.4). In the viscous sublayer the streaks have a regular pattern and sinuously oscillate. In the buffer layer, however, the pattern is less regular. The streaks are seen to breakdown in an intermittent way associated with 'bursts'. The data of Kline *et al.* (1967) and Smith & Metzler (1983) indicate that the average spanwise streak-spacing corresponds approximately to $\lambda_z^+ = 100$, in wall units in the near-wall region. This

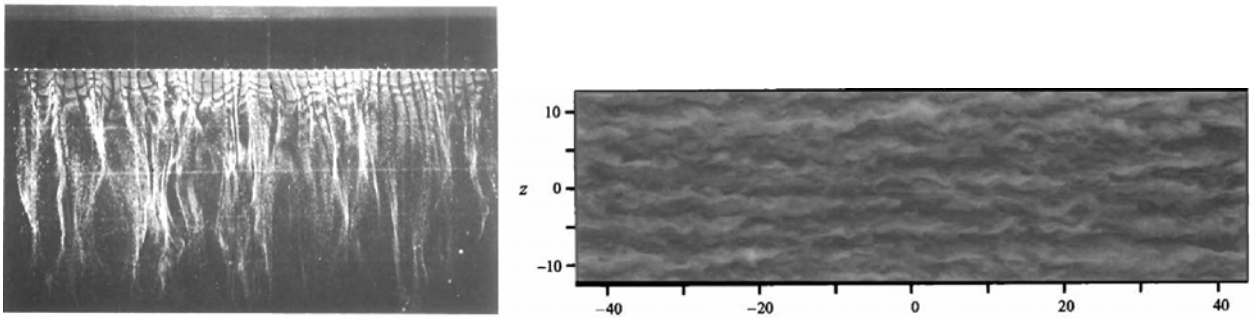

Figure 1.4: Streaks in developed turbulent flows. Left panel: hydrogen bubbles visualization of streaks in the viscous sub-layer of turbulent boundary where the mean streaks spanwise spacing is $\lambda_z^+ \approx 100$ (from Kline *et al.*, 1967). Right Panel: large-scale coherent streaks in plane Couette flow at Re = 750 ($Re_\tau = 52$) with mean streak spacing $\lambda z \approx 4 - 5h$ (from Komminaho *et al.*, 1996).

spacing has been confirmed by the first direct numerical simulation of channel flow at $Re_\tau \approx 180$ by Kim *et al.* (1987). This first DNS also revealed the existence of counter-rotating quasi-streamwise vortices, and that the mean spanwise spacing λ_z^+ increases with the distance from the wall.

Turbulent large (LSM) and very large (VLSM) scale motions. It has long been known that in turbulent flows the outer region is dominated by large-scale structures with dimensions of the order of the outer length scale h (e.g. the channel half-width or the boundary layer δ_{99} thickness) often separated by regions of non-turbulent fluid. These structures are called large-scale motions (LSM) and they have typical streamwise and spanwise size of $\approx 2 - 3h$ and $\approx 1 - 1.5h$ respectively (Corrsin & Kistler, 1954; Kovasznay *et al.*, 1970; Blackwelder & Kovasznay, 1972).

More recently it has been realized that in addition to large-scale motions, 'very large-scale motions' (VLSM) with even longer scales extending up to $\lambda_x \simeq O(10h)$ exist[1] in plane Couette flow (Lee & Kim, 1991; Komminaho *et al.*, 1996; Kitoh *et al.*, 2005; Kitoh & Umeki, 2008; Tsukahara *et al.*, 2006), in plane channels (Jiménez, 1998; del Álamo & Jiménez, 2003; del Álamo *et al.*, 2004) and pipe flows (Kim & Adrian, 1999; Guala *et al.*, 2006) as well as in boundary layers (Tomkins & Adrian, 2005; Hutchins & Marusic, 2007*a*,*b*). Motions at large and very large-scale account for a significant amount of the turbulent kinetic energy and Reynolds stress in the outer region and they modulate the near-wall cycles (Hutchins & Marusic, 2007*b*; Mathis *et al.*, 2009).

The autonomous near-wall cycle The understanding of the origin of streaky motions in the viscous region has progressed along lines similar to those followed to understand the nature of subcritical transition with, often, a risk of confusion between the two mechanisms. Jiménez & Moin (1991) provided a seminal contribution by showing that near-wall turbulence can be sustained in spanwise and streamwise periodic numerical domains as small as $\lambda_z^+ \approx 100$,$\lambda_x^+ \approx 250 - 300$. In this way it was shown that the motions in the viscous region are sustained independently from motions at larger scales. A great effort followed to elucidate the nature of the self-sustained mechanism in 'minimal flow units'. Hamilton *et al.* (1995) studied the weakly turbulent dynamics in a minimal flow unit in plane Couette flow and proposed the self-sustained process (as already discussed in §1.1). Jiménez & Pinelli (1999) modified the evolution equation to include a filtering mechanism to damp the fluctuation above a certain distance from the wall. They found that the near-wall turbulence is sustained by an autonomous cycle in the range of $y^+ \approx 20 \sim 60$ which is independent of the core region. The process of streak generation via lift-up effect, streak instability leading to breakdown and vortex regeneration via nonlinear process is found to be the essential feature of this autonomous cycle.

[1]These motions are also known as 'superstructures' or, sometimes, 'global modes'.

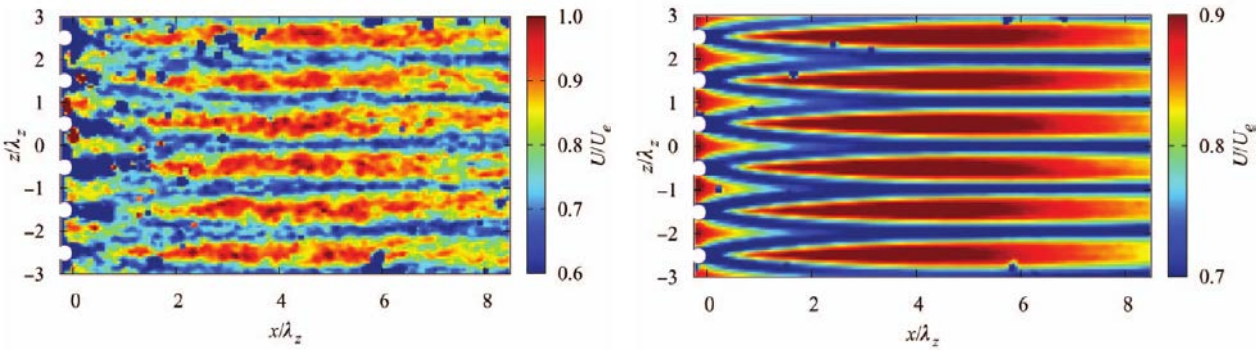

Figure 1.5: Experimental measures of large-scale coherent streaks produced using an array of cylindrical roughness elements. Left panel: Instantaneous streamwise velocity field: large-scale structures with superimposed small-scale fluctuations. Right panel: Time-averaged streamwise velocity revealing the structure of large-scale, coherent streaks. Note the transient downstream growth of the streaks amplitude (the amplitude of the spanwise velocity modulation). Figure from Pujals *et al.* (2010*b*).

Origin of LSM and VLSM: earlier interpretations. Large scale motions have been shown to contain a number of smaller scale structures which have been interpreted as hairpin vortices (Falco, 1977; Head & Bandyopadhyay, 1981) generated by the mutual vortical induction (Zhou *et al.*, 1999; Adrian *et al.*, 2000) and merger and growth of hairpins (Tomkins & Adrian, 2003; Adrian, 2007). A first attempt at explaining the origin of the very large-scale streaks was made by Kim & Adrian (1999) and Guala *et al.* (2006) who conjectured that they result from the concatenation of LSM. From a different perspective, Itano & Toh (2005) conjectured the existence of a co-supporting cycle where near wall structures sustain large-scale structures in plane Poiseuille flow. According to these explanations, large-scale streaky motions in the outer layer would not exist in the absence of the near-wall cycles. However, Flores & Jiménez (2006); Flores *et al.* (2007) showed that the outer motions are not significantly influenced by a drastic change of the near wall dynamics obtained by high roughness elements placed on the wall.

The coherent lift-up effect An alternative conjecture about the formation of large-scale motions is that they are sustained by a mechanism similar to the self-sustained process identified in transitional flows. An essential ingredient of this mechanism would be a sort of lift-up effect for large scale motions to be able to extract energy from the mean flow. This is exactly what del Álamo & Jiménez (2006), later corrected by Pujals *et al.* (2009), and Cossu *et al.* (2009) did by computing the optimal transient growth sustained by fully-developed turbulent channel and boundary layer flows, using the linear model of Reynolds & Hussain (1972) who model small coherent motions with an eddy viscosity. This approach was pursued by Hwang & Cossu (2010*a*,*b*); Willis *et al.* (2010), who computed the optimal response to harmonic and stochastic forcing and considered also the turbulent Couette and Hagen-Poiseuille flow cases. These investigations showed that coherent streaks are amplified by a *coherent lift-up effect*. The most amplified perturbations display two amplification peaks, which scale in outer and inner units respectively. The dominant optimal wavelengths have been shown to be in good agreement with the spanwise spacing of large-scale streaks in the outer region. The maximum amplification associated to this peak increases with the Reynolds number. The secondary optimal wavelength is found at $\lambda_z^+ \approx 100$, in agreement with the spanwise spacing of the near-wall streaks, the associated maximum amplification is relatively small and does not increase with the Reynolds number. Pujals *et al.* (2010*a*) experimentally confirmed the existence of spatial coherent transient growth in the turbulent boundary layer (see figure 1.5).

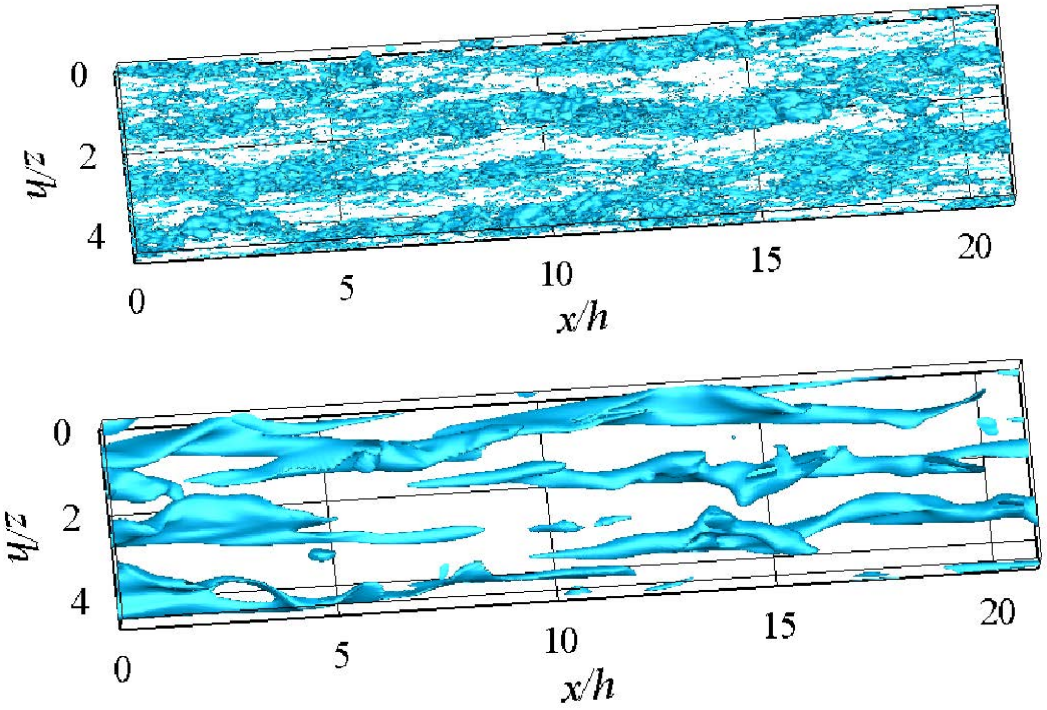

Figure 1.6: Iso-surface of instantaneous streamwise velocity fluctuations (from Hwang & Cossu, 2010*c*). Left Panel: at $C_s \approx 0.05$, large-scale streaks are populated with small-scale structure. Right Panel: Small-scale structures are quenched with artificial damping using $C_s \approx 0.2$ and large-scale streaks becomes more visible.

A self-sustained process at large scale and in the logarithmic layer. The existence of a robust coherent lift-up effect and the stability analysis of Park *et al.* (2011), who found that large-scale coherent streaks can undergo secondary instabilities, were strong indications that a self-sustained process might be at work at large scale in turbulent flows. A strong confirmation of this conjecture has been given by Hwang & Cossu (2010*c*) who have shown that large scale motions can self-sustain even in the absence of small-scale structures. In order to suppress the small-scale motions while preserving the dissipation associated with them, Hwang & Cossu (2010*c*) used a large eddy simulation (LES) filter and artificially increased its cutoff characteristic length. They were able to prove that when the motions associated to the near wall are artificially quenched, motions with the usual scales of large scale motions survive, as shown in figure 1.6. These conclusions have been later extended by Hwang & Cossu (2011) to intermediate flow units, characteristic of motions in the logarithmic layer.

1.3 Objective of this thesis

An impasse in the invariant solutions approach. The analysis of invariant solutions of the Navier-Stokes equations using methods borrowed from dynamical systems theory has led to important progress in our understanding of subcritical transition in shear flows. This progress can be appreciated in figure 1.3. From that figure it is also apparent that while the lower branch solutions explain well the departure from the laminar state to attain the turbulent one, the understanding of the turbulent state itself needs improvement. The original hope was that turbulent solutions spend a significant time in the neighbourhood of relevant saddle points (NTW) in phase space, but this has been later shown not to be the case (Kerswell & Tutty, 2007; Schneider *et al.*, 2007). The current hope is that turbulent statistics could be captured by expansions based on the

properties of unstable periodic solutions (Artuso *et al.*, 1990). However, to this date, attempts to prove the relevance of this approach have not been completely successful (see e.g. Chandler & Kerswell, 2013). One may therefore question the relevance of invariant solutions in the fully turbulent regime developing at high Reynolds numbers. It could well be that the number of solutions needed to describe the flow increases with the Reynolds number, in accordance with the Richardson-Kolmogorov energy cascade picture.

Scope of this thesis. A possible, practical way out of this impasse is to model small-scale motions, in order to take only their averaged effect into account, and to concentrate on large-scale motions which contain most of the energy and do carry most of the turbulent Reynolds stresses. This is exactly the approach taken by Hwang & Cossu (2010*c*, 2011) in using a large eddy simulation approach to investigate self-sustained processes at large scales. Furthermore, the most recent results indicate that these motions at large scale play an increasingly important role at high Reynolds numbers (see e.g. Guala *et al.*, 2006; Marusic *et al.*, 2010). **The main goal of this thesis is to compute invariant solutions corresponding to these large-scale motions and understand their relevance to the fully developed turbulent flows.** Such an understanding could also help to better assess the relevance of upper branch invariant solutions computed for the Navier-Stokes equations mainly at transitional Reynolds numbers. Are they really relevant in fully developed turbulent flows? Do they evolve into near-wall or large-scale structures when the Reynolds number is raised sufficiently for scale separation of these structures to exist ?

Plan of the thesis. In chapter 2 and in appendix A and B, we introduce the mathematical and numerical tools used in this work. We then proceed, in chapter 3, to verify if large and very large-scale motions self-sustain in plane Couette flow in very wide and long numerical integration domains. In chapter 4 we then investigate the dynamics of large-scale motions in a 'LSM-Box', which is a sort of minimal flow unit for these motions. In this domain we are able to compute self-sustained coherent steady solutions and establish their relation to the Nagata-Clever-Busse-Waleffe Navier-Stokes solutions. We also investigate if the Nagata-Clever-Busse-Waleffe solutions can be continued into near-wall cycle solutions. Chapter 5 is dedicated to plane Poiseuille flow where we are able to compute relative periodic orbit solutions of the Navier-Stokes equations. We show that these periodic orbits are connected to travelling wave (TW) solutions via a global bifurcation (a saddle-node-infinite period bifurcation). We show that the lower branch of these TW solutions evolve into spanwise localized states when the spanwise size of the domain is increased while the upper branch solution displays features consistent with large-scale motions. These upper branch solutions are then continued to a turbulent coherent regime at Re = 2000. The main conclusions of this study are summarized and discussed in chapter 6.

Chapter 2

Background

2.1 Navier-Stokes equations, direct and large eddy simulations

Navier-Stokes equations. In this study the fluid is modelled by the usual Navier-Stokes equations for incompressible flows which, in Cartesian coordinates, read:

$$\frac{\partial u_i}{\partial x_i} = 0 \tag{2.1}$$

$$\frac{\partial u_i}{\partial t} + u_j \frac{\partial u_i}{\partial x_j} = -\frac{\partial p}{\partial x_i} + \nu \frac{\partial^2 u_i}{\partial x_j^2} \tag{2.2}$$

where u_i is the i-th velocity component, t is time, x_i is the spatial coordinate and p is the pressure and ν is the viscosity.

Direct numerical simulations. Direct numerical simulations (DNS) are used to solve eq. (2.2) with the aim of resolving the whole range of spatial and temporal scales of the turbulence. The Kolmogorov length scale $\eta = (\nu^3/\epsilon)^{1/4}$, where ϵ is the rate of dissipation, is often used as a reference size of the smallest scale to be resolved by the DNS. The memory and CPU requirements of DNS can become quickly prohibitive even at moderate Reynolds numbers because motions with decreasing scale must be resolved when the Reynolds number is increased. For instance, DNS of turbulent channel or Couette flows at $\mathrm{Re}_\tau = O(10^3)$ in sufficiently large domains have been performed only very recently (see e.g. Jiménez & Hoyas, 2008; Avsarkisov *et al.*, 2014).

Large eddy simulations with the static Smagorinsky model. In large eddy simulations (LES), scales larger than the grid size are resolved both temporally and spatially, while the effect of subgrid scales (SGS) are modelled. The equations governing the evolution of large-scale motions are derived from the Navier-Stokes equations by using an appropriate low-pass filter[1] (see e.g. Deardorff, 1970; Pope, 2000):

$$\frac{\partial \overline{u}_i}{\partial x_i} = 0 \tag{2.3}$$

$$\frac{\partial \overline{u}_i}{\partial t} + \overline{u}_j \frac{\partial \overline{u}_i}{\partial x_j} = -\frac{\partial \overline{q}}{\partial x_i} + \nu \frac{\partial^2 \overline{u}_i}{\partial x_j^2} - \frac{\partial \overline{\tau}_{ij}^r}{\partial x_j} \tag{2.4}$$

where the overhead bar denotes the filtering action, the residual stress tensor is defined as

$$\overline{\tau}_{ij}^R = \overline{u_i u_j} - \overline{u}_i \overline{u}_j, \tag{2.5}$$

[1]The large-scale motions are then also called 'filtered' motions.

the anisotropic residual stress tensor is

$$\overline{\tau}^r = \overline{\tau}^R - \frac{tr(\overline{\tau}^R)}{3}\mathbf{I}, \tag{2.6}$$

and $\overline{q} = \overline{p} + tr(\overline{\tau}^R)/3$. The anisotropic residual stress tensor $\overline{\tau}_{ij}$ is modelled choosing an appropriate subgrid model in terms of eddy viscosity ν_t:

$$\overline{\tau}^r_{ij} = -2\nu_t \overline{S}_{ij}, \tag{2.7}$$

where $\overline{S}_{ij}$ is the rate of strain tensor of filtered motions:

$$\overline{S}_{ij} = \frac{1}{2}\left(\frac{\partial \overline{u}_i}{\partial x_j} + \frac{\partial \overline{u}_j}{\partial x_i}\right) \tag{2.8}$$

For the eddy viscosity we choose the *static* Smagorinsky (1963) model:

$$\nu_t = D(C_S\overline{\Delta})^2\overline{\mathcal{S}}, \tag{2.9}$$

where $\overline{\Delta} = (\overline{\Delta}_x\overline{\Delta}_y\overline{\Delta}_z)^{1/3}$ is the average length scale of the filter based on the grid spacing in the simulation, $\overline{\mathcal{S}} \equiv (2\overline{S}_{ij}\overline{S}_{ij})^{1/2}$. and C_S is the *Smagorinsky constant*. To avoid non-zero residual velocity and shear stress at the wall we use the wall (damping) function $D = 1 - e^{-(y^+/A^+)^2}$ proposed by Kim & Menon (1999). The use of static Smagorinsky model ensures that the residual (unsolved) motions cannot transfer energy to the (resolved) filtered motions, i.e. there is no 'backscatter' of energy. This is essential in our approach of proving that large-scale motions can also be sustained in the absence of forcing by smaller-scale motions. The absence of backscatter can be verified by considering the rate of change of kinetic energy of the filtered velocity field[2]:

$$\underbrace{\frac{\partial}{\partial t}\left(\frac{1}{2}\overline{u}_i^2\right) + \overline{u}_j\frac{\partial}{\partial x_j}\left(\frac{1}{2}\overline{u}_i^2\right)}_{\frac{dE_f}{dt}} = \underbrace{\frac{\partial}{\partial x_j}\left[\overline{u}_i\left(\overline{q}\delta_{ij} + 2\nu\overline{S}_{ij} - \overline{\tau}^r_{ij}\right)\right]}_{transport} - \underbrace{2\nu\overline{S}_{ij}\overline{S}_{ij}}_{\epsilon_f} + \underbrace{\overline{\tau}^r_{ij}\overline{S}_{ij}}_{\mathcal{P}_r} \tag{2.10}$$

The second term on the right hand side ϵ_f represents viscous dissipation due the filtered velocity field. The third term, $\mathcal{P}_r$, is the rate of production of kinetic energy due to the work of subgrid scale motions against the filtered shear. Energy backscatter is associated to a positive production term $\mathcal{P}_r$. However, by using the static Smagorinsky model, the production term is transformed into a (eddy viscosity) viscous dissipation term $\mathcal{P}_r = -2\nu_t\overline{S}_{ij}\overline{S}_{ij}$ and is therefore always negative.

The Hwang & Cossu (2010*c*) overdamping. In chapter 3 and chapter 4 we will use the technique used by Hwang & Cossu (2010*c*, 2011) to quench small scale motions and investigate if the large scale motions survive despite this quenching. The technique simply consists in increasing the value of the Smagorinsky constant C_s which is equivalent to an increase of the 'Smagorinsky mixing length' $l_0 = C_s\Delta$, as shown by Mason & Callen (1986). When C_s is increased, an increasing range of small-scale motions shifts from resolved to unresolved and therefore becomes inactive as they are modelled with a (positive) eddy viscosity.

[2]Equation (2.10) is obtained by multiplying eq. (2.4) with $\overline{u}_i$ and rearranging the right hand side.

2.2 Considered flow configurations

In this study we consider the flow of a Newtonian incompressible viscous fluid confined by two parallel rigid walls situated at $y = \pm h$, where y denotes the wall-normal coordinate.

In the case of the plane Couette flow the two walls move in opposite directions with speed $\pm U_w \mathbf{e}_x$, where $\mathbf{e}_x$ is the unit vector of the x (streamwise) axis, and no external pressure gradient is enforced. In this case the Navier-Stokes equations are made dimensionless using h as reference length and U_w as reference velocity. The Reynolds number is thus defined as $U_w h/\nu$, where ν the kinematic viscosity. In dimensionless units, the (laminar flow) Couette solution is $\{u, v, w\} = \{y, 0, 0\}$,where y and z denote the (dimensionless) wall-normal and spanwise coordinates and u, v, w the (dimensionless) velocity components along x, y and z, respectively.

In the case of Poiseuille flow the walls are fixed but a constant streamwise pressure gradient dP/dx is enforced along the x axis. If h is used as reference length and $U_P = (h^2/2\rho\nu)|dP/dx|$ is used as reference velocity, the (laminar) Poiseuille solution is $\{1 - y^2, 0, 0\}$ and the Reynolds number is defined as $Re = U_P h/\nu$. Thus, the reference velocity is the maximum velocity attained by the laminar Poiseuille solution.

2.3 Turbulent statistics

Average. Many of the results presented in the following chapters describe mean properties of turbulent flows. Here we briefly recall the definitions that will be used in the remainder of this thesis. We denote by $\overline{\mathbf{a}}$ the average of a vector field $\mathbf{a}(\mathbf{x}, t, n)$ which, in general, depends on the spatial coordinate $\mathbf{x}$, on time t and on the specific realization n. While, in principle, the use of ensemble average based on n would be highly desirable, in practice this approach is very rarely followed due to the often limited number of realizations of the flows we describe. In the following, therefore, as a general rule, we will use a spatio-temporal average based on a single realization, which is justified by the stationarity and $x - z$ spatial homogeneity of turbulent processes in the considered parallel flows:

$$\overline{a}(y) = \frac{1}{|t_2 - t_1| L_x L_z} \int_{t_1}^{t_2} \int_0^{L_x} \int_0^{L_z} a(x, y, z, t)\, dz\, dx\, dt. \tag{2.11}$$

Mean and rms velocity profiles. In the considered turbulent plane Couette and Poiseuille flows, the mean velocity field is of the form:

$$\overline{\mathbf{u}} = U(y)\mathbf{e}_x. \tag{2.12}$$

Velocity fluctuations are defined as $\mathbf{u'} = \mathbf{u} - \overline{\mathbf{u}}$. The root mean square (*rms*) perturbation velocity fields are defined as the square root of the variance of the fluctuations $u_{i,rms} = \left[\overline{(u_i')^2}\right]^{1/2}$ and therefore:

$$u_{rms} = \left[\overline{(u - U)^2}\right]^{1/2}; \quad v_{rms} = \left[\overline{v^2}\right]^{1/2}; \quad w_{rms} = \left[\overline{w^2}\right]^{1/2}; \tag{2.13}$$

Two-point correlation and energy spectra. The two-points velocity correlation is defined as:

$$R_{ij}(y, \mathbf{r}) = \overline{u_i'(\mathbf{x}, t) u_j'(\mathbf{x} + \mathbf{r}, t)} \tag{2.14}$$

Suppose we have computed two-point correlations along the streamwise direction (x) for a selected y, then one-dimensional spectra $\Phi_{ij}(y, k_x)$ are defined to be the one-dimensional Fourier

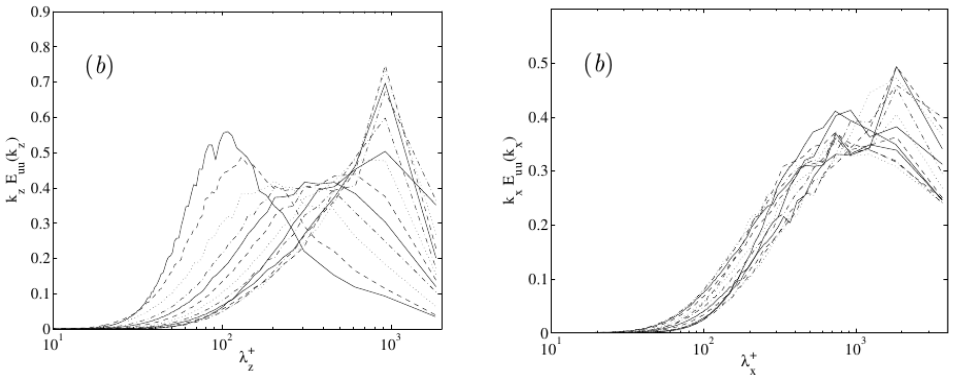

Figure 2.1: One-dimensional pre-multiplied spectra of the streamwise velocity at selected distances from the wall in turbulent Poseuille flow at $Re_\tau = 590$. Left panel: spanwise premultiplied spectrum. Right panel: streamwise premultiplied spectrum. Figure from Jiménez (1998).

transform of $R_{ij}(y, r_x)$:

$$\Phi_{ij}(y, k_x) = \frac{1}{\pi} \int_{-\infty}^{\infty} e^{-i k_x r_x} R_{ij}(y, r_x) dr_x \tag{2.15}$$

$R_{ij}(y, r_x)$ is the inverse Fourier transform of Φ_{ij}:

$$R_{ij}(y, r_x) = \frac{1}{2} \int_{-\infty}^{\infty} \Phi_{ij}(y, k_x) e^{i k_x r_x} dk_x. \tag{2.16}$$

The local velocity variance can be expressed in terms of Φ:

$$u_{i,rms}^2(y) = R_{ii}(y, 0) = \int_0^{\infty} \Phi_{ii}(y, k_x)\, dk_x. \tag{2.17}$$

Thus, $\Phi_{ii}(y, k_x)dk_x$ represents the average contribution to the variance $u_{i,rms}$ of motions with wavenumber in the range $[k_x - dk_x/2, k_x + dk_x/2]$. The same rationale can be applied to compute the velocity spectra in the spanwise direction z. The following notation is used in the remainder of the manuscript, in accordance with standard notation used in the literature: $\Phi_{11} \rightarrow E_{uu}$, $\Phi_{22} \rightarrow E_{vv}$, $\Phi_{33} \rightarrow E_{ww}$.

Premultiplied spectra. Due to the large range of spatial scales involved in the considered turbulent motions, when representing the spectra as a function of the wavenumbers k_x or k_z, a logarithmic scale is used for the wavenumber axis. In this case, to preserve the property that the area $Ed \log k$ below the curve in the range $[k, k + dk]$ is proportional to the energy content in this range, it is customary (see Bullock *et al.*, 1978; Jiménez, 1998) to plot the *premultiplied* energy spectra $k\,E$ which respects this property.[3] The same rationale applies when the energy is displayed against wavenumbers in log-scale.[4]. The pre-multiplied spectra are often used to determine the scales of motion present in a turbulent flow. Jiménez (1998) plotted pre-multiplied spectra to determine the relevant scales of motion in a turbulent channel flow at $Re_\tau = 180, 590$. He indeed showed the existence of the $\lambda_z^+ \approx 100$ peak in spanwise premultiplied spectra in the near wall region and of large-scale structures in the bulk of the flow (see figure 2.1).

[3]Indeed $kEd \log k = Edk$.
[4]Indeed $d \log(\lambda) = -d \log(k)$

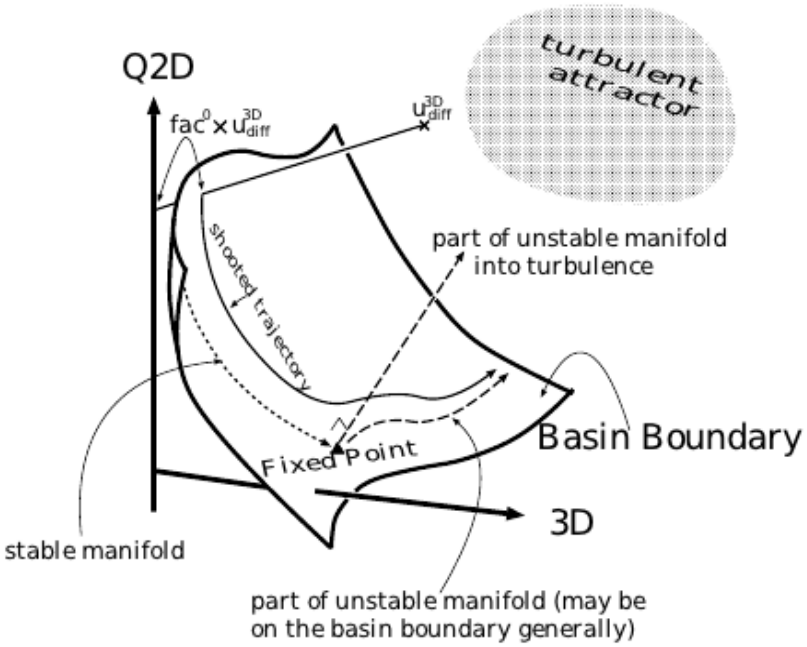

Figure 2.2: Sketch, reproduced from Toh & Itano (2003), of the edge of chaos surface with an embedded edge state fixed point (the attractor within the edge of chaos).

2.4 Edge-tracking

Langton (1990), a leading scientist in the field of artificial life, while studying one dimensional cellular automata problems, found out two states of automation one "dead" and the other "alive". The dead states are highly organized and extreamly ascertainable, while alive states seem almost chaotic. In between the border of dead and alive state, he discovered a third state that displayed complex, almost lifelike behaviour. He defined a parameter λ, whose value if 0 leads to "dead" state and if 1 leads to "alive" state and for a particular value in between $0-1$ the system settle down to a border state. The mathematician J. Doyne Farmer coined the term 'Edge of Chaos' to describe this 'border state'. The idea of edge of chaos has been extended to various other fields like economics, social and biological systems and physical sciences. The basic idea of studying the objects confined on edge surface remains the same irrespective of the field of applicability.

In dynamical systems theory applied to subcritical transition in fluid dynamics, the edge of chaos is defined as a surface in phase space which separates regions leading to a fast decay to the laminar state from regions with chaotic dynamics (see e.g. Skufca *et al.*, 2006; Eckhardt *et al.*, 2007; Schneider *et al.*, 2007, 2008). Edge states are attractors within the edge of chaos and can be equillibrium points (Schneider *et al.*, 2008), nonlinear travelling waves (Viswanath, 2008), periodic or relative periodic orbit (Itano & Toh, 2001; Kreilos *et al.*, 2013; Rawat *et al.*, 2014). In cases where the dimension of the edge of chaos is $N-1$, N being the dimension of the phase space, it is possible to constrain the solution to remain in a neighbourhood of the edge of chaos by a one parameter bisection technique (see e.g. Itano & Toh, 2001; Toh & Itano, 2003), sometimes labelled 'edge tracking'.

In this thesis we apply the edge-tracking technique to approach travelling wave or relative periodic orbit solutions that typically are 'lower branch' solutions. In its most basic form, the edge tracking is realized by adding some initial perturbation to the linearly stable laminar basic flow

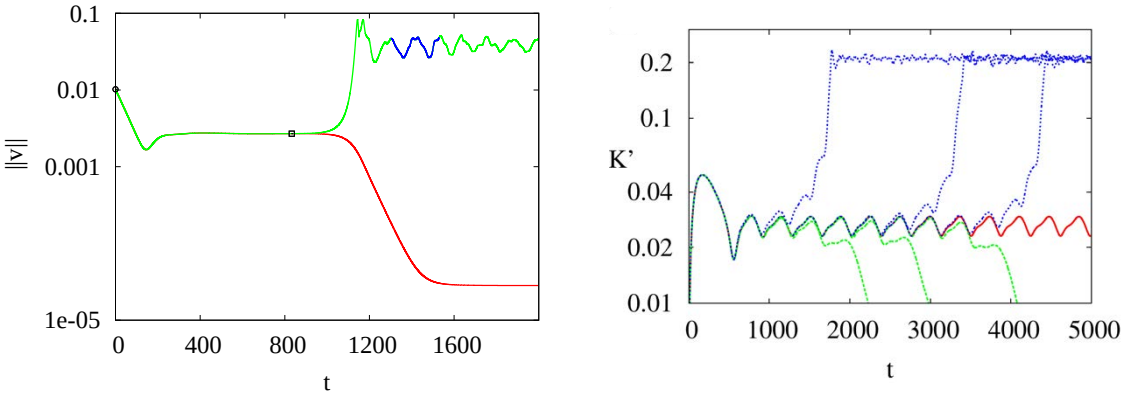

Figure 2.3: Examples of edge-tracking on the laminar-turbulent boundary where the edge state is, respectively a nonlinear travelling wave (left panel, Couette flow, see chapter 4 for further details) and a relative periodic orbit (right panel, Poiseuille flow, see chapter 5 for further details).

premultiplied with a control amplitude λ:

$$\mathbf{u}_0 = \mathbf{U} + \lambda \mathbf{u}_0' \tag{2.18}$$

Assume that we know two values λ_L and λ_T for which the initial condition relaxes to $\mathbf{U}$ or evolves towards a chaotic behaviour respectively. A standard bisection is performed in the interval $[\lambda_L, \lambda_T]$ to determine if the value $\lambda = (\lambda_L + \lambda_T)/2$ will be the new λ_L or the new λ_T, halving the length of the new interval. The bisection is performed iteratively to compute the threshold value for λ which separates the two regions (see figure 2.2). In practice, iterations are stopped when the relative variation of the control parameter is less than a predefined tolerance $2|\lambda_T - \lambda_L|/(\lambda_T + \lambda_L) < \varepsilon_{edge}$. Tolerances as low as $\varepsilon_{edge} = 10^{-10}$ can be used to produce solutions lying on the edge for long times, which may be required to approach sufficiently the edge state. Examples of edge-trackings are given in figure 2.3.

2.5 Finding steady, TW and RPO solutions

Finding steady solutions. Steady solutions of the Navier-Stokes equations (2.2) or of the LES equations (2.4) can be found by looking for solutions having $\partial \mathbf{u}/\partial t = 0$ and $\partial \overline{\mathbf{u}}/\partial t = 0$ respectively. These solutions, which are often unstable, can be computed using a Newton-based method. The Newton methods we use in this thesis are based on calls to the `diablo` and `channelflow` LES and DNS codes. In this approach one is typically led to compare solutions at a given time T (obtained by DNS or LES) to the initial condition given to the simulation. A velocity field is a steady solution if $\mathbf{u}(x, y, z, T) = \mathbf{u}(x, y, z, 0), \forall T$ (and similarly for $\overline{\mathbf{u}}$ in the LES case). As one of the velocity components and the pressure can be computed from the other two velocity components, or in an equivalent way from the wall-normal velocity and vorticity, only two scalar fields are stored in the state vector $\mathbf{\Phi}(x, y, z, t)$ describing the state of the system. The function that must be set to zero by the Newton-based method therefore is $\mathbf{\Phi}(x, y, z, T) - \mathbf{\Phi}(x, y, z, 0)$ where T is a given final time which is assigned usually to small but finite values.

Finding travelling waves (TW). Travelling waves are solutions which travel at a given phase speed C_x, C_z in the streamwise-spanwise directions without changing shape. They correspond to steady solutions in a reference frame travelling at their phase speed and therefore satisfy $\mathbf{u}(x + C_x T, y, z + C_z T, T) = \mathbf{u}(x, y, z, 0), \forall T$. The solutions, in this case, are of course defined up to arbitrary

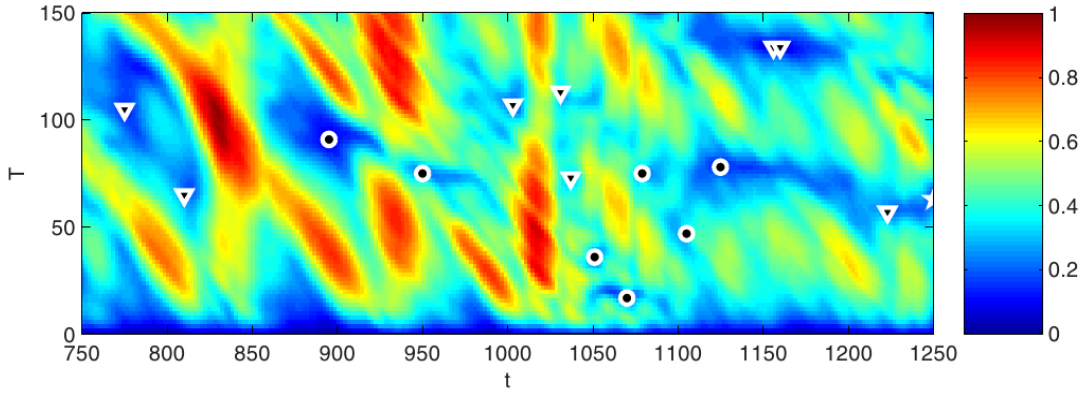

Figure 2.4: Relative distance between the velocity field at time t and the one at time $t+T$. Dark blue region indicated close recurrences (potential good initial guesses for Newton searches). Circles correspond to the initial guesses successfully converged to periodic orbits while triangles denote a convergence failure (figure from Cvitanovic & Gibson, 2010).

translations in x and z because of the continuous $x-z$ translational invariances of the system. There is therefore a double infinite number of solutions which physically represent the same solution translated in space by the streamwise and spanwise phase. When looking for these solutions, it is therefore customary to add to the system two additional scalar conditions to be satisfied by the solutions, which have the effect of fixing the spatial phases of the solution. The phase speeds C_x and C_z are the two additional unknowns associated with these equations (see §B.3 for more details).

Finding relative periodic orbits (RPO). A periodic solution is such that $\mathbf{u}(x,y,z,t+T) = \mathbf{u}(x,y,z,t), \forall t$ for the specific value of the temporal period T. Periodic solutions are defined up to a temporal phase. A relative periodic (RPO) solution is periodic in the reference frame travelling at its phase speed $\mathbf{u}(x+C_x(t+T),y,z+C_z(t+T),t+T) = \mathbf{u}(x,y,z,t), \forall t$. RPO solutions are therefore defined up to arbitrary translations in x and z and t. When looking for these solutions, it is therefore customary to add to the system three additional scalar conditions to be satisfied by the solutions and that have for effect to fix the spatial and temporal phases of the solution. The three additional conditions are needed to solve also for the temporal period T and the phase speeds C_x and C_z. The implementation of these conditions, used e.g. by Viswanath (2007) and Duguet *et al.* (2008*a*), is detailed in §B.3.

Initial guess for finding TW and RPO solutions. One of the main difficulties inherent to the computation of travelling waves or relative periodic solutions is to provide a suitable initial guess which is sufficiently close to the solution. When looking for 'lower branch' solutions (TW or RPO) a good idea is to converge to a genuine edge state or to an edge state within a particular symmetric subspace of the solutions (Duguet *et al.* (2008*b*)). This is the approach we mainly use in the following. A second technique, which in practice is almost equivalent, is the one introduced by Waleffe (1998, 2001, 2003) and then widely used in other flows is to artificially force streamwise vortices which induce streamwise streaks which become unstable at a critical forcing amplitude. The streak instability coincides with the bifurcation to a TW which can then be tracked down to zero forcing amplitude, where it is self-sustained. The TW found this way is typically a lower branch solution, which can then be continued in Reynolds or in the forcing amplitude in order to find the corresponding upper branch solutions. Finally, another technique based on the analysis of the solution correlations in the chaotic regime, can be used to provide upper branch TW or

RPO solutions. In this method a reference velocity field $\mathbf{u}(t)$ is initially selected in order to plot the relative 'distance' from solutions at other times using the function

$$d(C_x, C_z, t, \tau) = \frac{\|\mathbf{u}(x + C_x\tau, y, z + C_z\tau, t + \tau) - \mathbf{u}(x, y, z, t)\|}{\|\mathbf{u}(x, y, z, t)\|}.$$

Typically the function $d(C_x, C_z, t, \tau)$ is first minimized with respect to the phase speeds to give the function $d_{opt}(t, \tau)$ which is then plotted in the t, τ plane (see figure 2.4). The minima of this function are used as initial guesses for Newton-based iteration to look for TW or RPO solutions, depending on the structure of d_{opt} in the neighbourhood of the considered minimum.

Chapter 3

Self-sustained large and very large-scale motions in turbulent Couette flow

In this chapter we investigate the nature of coherent large (LSM) and very large-scale motions (VLSM) in plane Couette flow. The main goal here is to understand if these motions are forced by motions at smaller scales or if they self-sustain by an intrinsic mechanism. To this end we first summarize the main results previously obtained by other groups using direct numerical simulations. Some of these results are reproduced by LES with a suitable Smagorinsky constant. We then investigate, following the method of Hwang & Cossu (2010*c*), if large and very large-scale motions survive when the near-wall cycle is artificially quenched by increasing C_s. We finally briefly summarize the main results.

3.1 Previous results on LSM and VLSM in plane Couette flow

Lee & Kim (1991), in an early direct numerical simulation of fully developed turbulent Couette flow, discovered quasi-steady vortical structures at the centre of the channel. They used a computational box of $4\pi h \times 8\pi h/3$, at $Re = 3000$. They reported that these structures are uniform in streamwise direction and contribute about 30% of the turbulent kinectic energy.

Bech & Andersson (1994), who performed a DNS in a domain of $4\pi h \times 2\pi h$, found large-scale structures similar to those of Lee & Kim (1991). They also investigated the effect of box size and found by increasing the spanwise domain by 2 the structure have a non-zero inclination to the mean flow direction.

Tillmark & Alfredsson (1994) used particle image velocimetry to show the existence of large-scale structures in Couette flow. They observed that these structures have spanwise spacing of more than twice the channel height.

Komminaho *et al.* (1996) investigated the effect of an increase of the computational domain on these large-scale structures. They used a domain of $28\pi h \times 8\pi h$ and argued that the computational domain of Lee & Kim (1991) and Bech & Andersson (1994) was too small, which results in the overprediction of the two-point correlation for large streamwise separation. They examined in detail the effect of box length on the two-point velocity correlation with streamwise and spanwise separation. They reported that due to the symmetry properties of the correlation function $R_{uu}(\Delta x)$ its value is always overpredicted at half box length. They further pointed out that they needed sufficiently long simulation time to obtain a fairly converged statistics. The flow visualisation and the correlations showed that the large-scale structure have streaky nature with a weak streamwise vorticity. In accordance with Tillmark & Alfredsson (1994) they also observed that the vortical structures fill the entire gap but in contrast to Lee & Kim (1991), who found out that vortex structures are stationary in time and fixed in space, they concluded that neither of this holds in larger

Reference	L_x	L_z	N_x	N_z	N_y	Re	Re_τ	Δx^+	Δz^+
Lee & Kim (1991)	12.56	8.38	128	129	192	3000	170	16.6	7.41
Komminaho *et al.* (1996)	31.4	12.56	125	85	55	750	52	19	15.6
Tsukahara *et al.* (2006), $Re_\tau = 52$	89.6	24.0	1024	512	96	750	52	4.54	2.60
Tsukahara *et al.* (2006), $Re_\tau = 127$	130	12.0	2048	256	96	2150	127	8.015	5.90
VLSM-Box, $Re_\tau = 52$	130	12.5	650	64	48	750	52	10.4	10.1
VLSM-Box, $Re_\tau = 127$	130	12.5	650	64	48	2150	127	25	24

Table 3.1: Computational domains and discretization parameters used in previous investigations compared to the ones used in the present chapter (VLSM-Box).

domains. If a Gaussian filter is applied to the fluctuating field, the large-scale structure is seen to qualitatively follow the break-up regeneration cycle as reported by Hamilton *et al.* (1995) for minimal domains.

More recently Tsukahara *et al.* (2006) argued that most of the previous DNS used too small domains due to the computational constraints and, as a consequence, the two-point correlation seldom drops to zero. Tsukahara *et al.* (2006) therefore used very long and wide domains, such as e.g. $124h \times 16h$ at Reynolds numbers as high as 2150 which corresponds to $Re_\tau = 127$. They analyse the pre-multiplied spectra and two-point correlation and marked out a peak at $\lambda_x \approx 64h$ and $\lambda_z \approx 4.2 - 5\,h$, suggesting the scale of very large-scale structures. They also implied that these structure influence the near wall structures and noticed that near-wall low-speed streaks are located below the large-scale low-speed structure in the core region. In the present study we use the Tsukahara *et al.* (2006) results as reference case.

3.2 Validation of reference large eddy simulations

Reference simulations. As a first step, we tried to reproduce the results of Tsukahara *et al.* (2006) in very large and wide numerical domains using large eddy simulations with a static Smagorinsky filter. The Tsukahara *et al.* (2006) data are posted online and are an excellent source for testing the LES algorithm. The numerical parameters considered are reported in Tab. 3.1, from which it can be seen that at the two Reynolds numbers considered the grid spacing in the LES is such that the near wall cycle, with characteristic lengths $\lambda_z^+ \approx 100$ and $\lambda_x^+ \approx 600$ can be roughly captured. This will be important in the following, where the near wall cycle will be artificially quenched.

Kim & Menon (1999) have shown that setting the Smagorinsky constant to $C_s \approx 0.055 - 0.06$ along with the use of a wall-damping damping function (see §2.1 and §B.2) gives LES results in agreement with DNS data. We followed their approach and performed a fairly long simulation to gather converged statistics. The simulation is initialized with a random initial condition with arbitrary phase. The effect of initial transients are removed while calculating the turbulent statistics. Komminaho *et al.* (1996) explained that the time scales for integral quantities are longer than the instantaneous ones and that therefore long simulation times are needed to get converged statistics for correlation quantities. The simulations are stopped when the mean flow and *rms* velocity profiles change by less than 0.1%.

Mean and *rms* velocity profiles. Figure 3.1 shows the mean velocity profile and turbulent fluctuation for the present case compared against the direct numerical simulation of Tsukahara *et al.* (2006) at $Re_\tau = 52$ and $Re_\tau = 127$. The mean velocity profile $U^+(y)$ is in excellent agreement with the DNS data for both Reynolds numbers, while the turbulent fluctuation are in good agreement

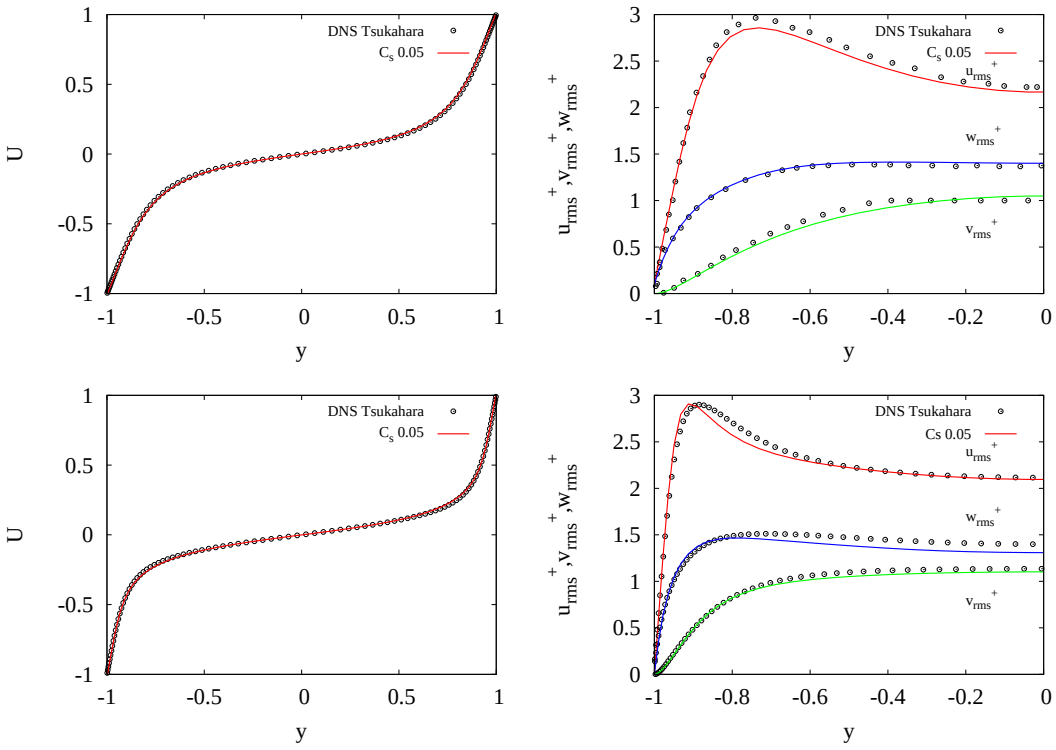

Figure 3.1: LES-DNS comparison in a VLSM-Box for $Re_\tau = 52$ (top row) and $Re_\tau = 127$ (bottom row). Panels on the left compare the mean flow profiles $U^+(y)$, while the panels on the right show the variance of the three velocity components u'^+, v'^+ and w'^+ as a function of wall-normal coordinate (y). The data of our LES is compared to the data of the DNS of Tsukahara *et al.* (2006).

at $Re_\tau = 52$ and in acceptable agreement at $Re_\tau = 127$. This is probably due to the fact that, in addition to a coarser grid, a *static* Smagorinsky model is used which is known for avoiding energy backscatter from unresolved to resolved scales. We therefore probably loose a part of the energy of the near-wall cycle, but this is exactly what we want to do next.

Premultiplied spectra. We now verify if the essential features of large-scale and very large-scale motions are captured by computing the one-dimensional streamwise and spanwise energy spectra at several selected wall-normal locations y for the three velocity components. We denote by E_{uu}, E_{vv} and E_{ww} the streamwise, wall normal and spanwise velocity energy spectra respectively, and plot them in premultiplied form (see §2.3 and Bullock *et al.*, 1978; Jiménez, 1998). The positions of maxima in the pre-multiplied spectra indicate the wavelengths containing significant energy.

Let us begin by considering the streamwise velocity spectra, which denote the characteristic size of streaky structures. From figure 3.2*a* and figure 3.3*a*, corresponding to $Re_\tau = 52$ and $Re_\tau = 127$ respectively, two well defined peaks can be observed in the spanwise premultiplied spectra $k_z E_{uu}$. The first, obtained near the wall, scales in wall units and corresponds to $\lambda_z^+ = 80 \sim 100$, while the second, which scales in outer units, is obtained at $\lambda_z/h = 4.2$. These two peaks correspond to streaky motions of the near wall cycle and to the large-scale motions and are in very good agreement with the values found in all previous investigations and in particular that of Tsukahara *et al.* (2006). The corresponding streamwise premultiplied spectra $k_x E_{uu}$ are reported in figure 3.2*b* and figure 3.3*b* and are associated to the length of the streaky structures and are in very good agreement with those reported by Tsukahara *et al.* (2006). At $Re_\tau = 52$, a single peak is found for $\lambda_x/h \approx 11$, corresponding to $\lambda_x^+ \approx 600$. At $Re_\tau = 127$, three peaks of $k_x E_{uu}$ have

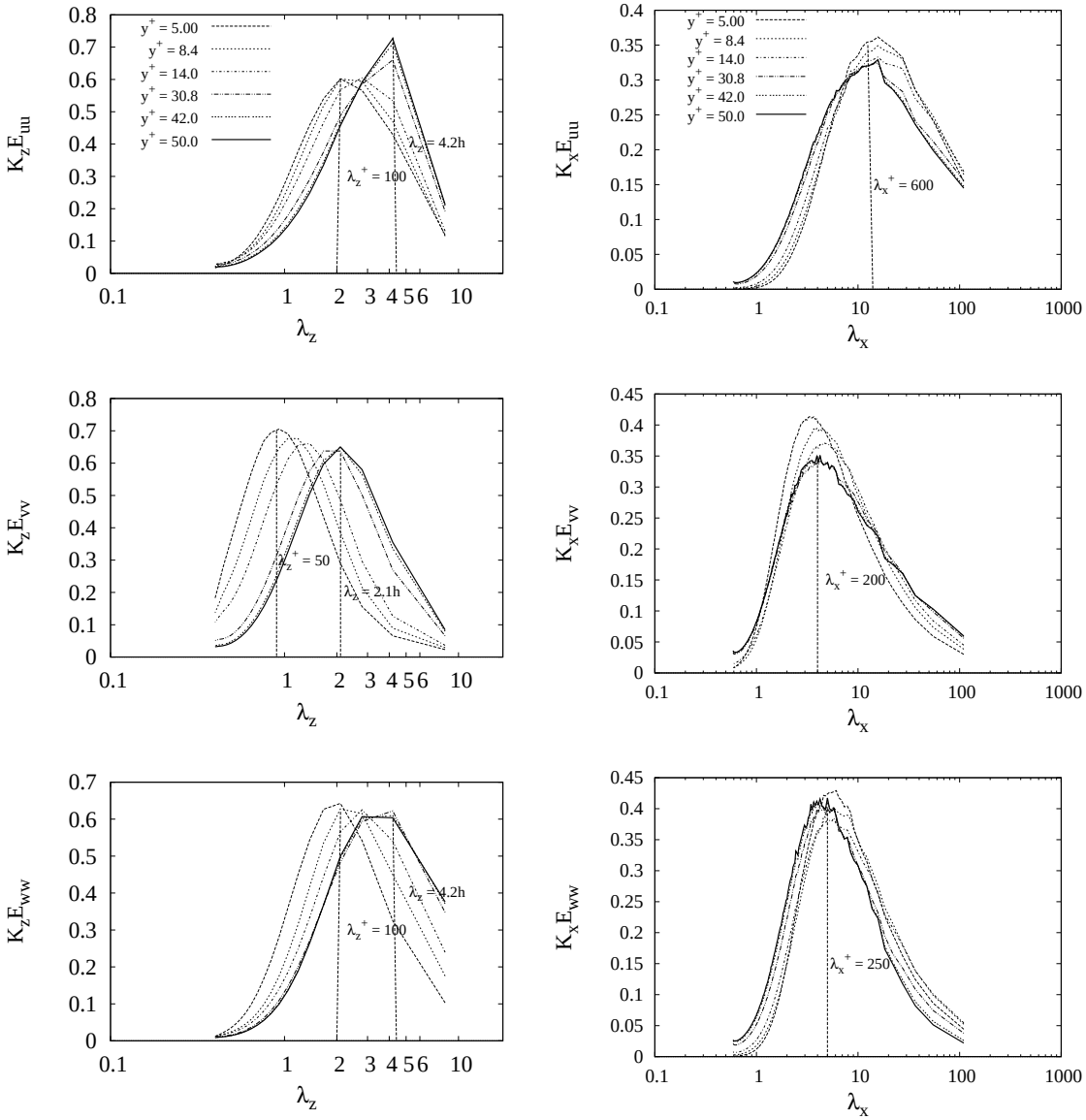

Figure 3.2: One-dimensional premultiplied spectra at $Re_\tau = 52$: Left panel shows spanwise spectra k_zE_{uu}, k_zE_{vv} and k_zE_{ww} (top to bottom) as a function of λ_z. Right panel shows streamwise spectra k_xE_{uu}, k_xE_{vv} and k_xE_{ww} (top to bottom) as a function of λ_x.

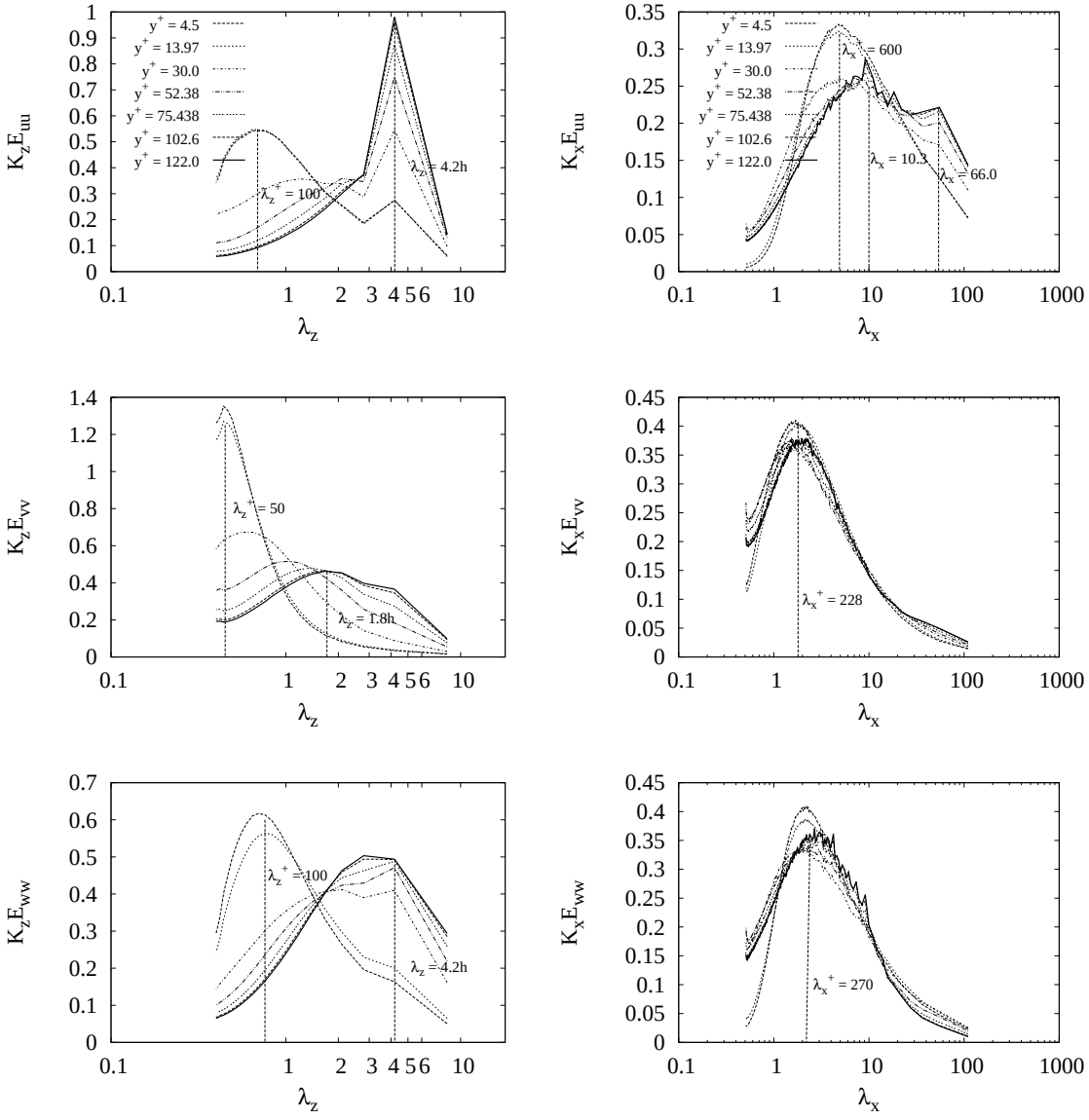

Figure 3.3: One-dimensional premultiplied spectra at $Re_\tau = 127$: Left panel shows spanwise spectra k_zE_{uu}, k_zE_{vv} and k_zE_{ww} (top to bottom) as a function of λ_z. Right panel shows streamwise spectra k_xE_{uu}, k_xE_{vv} and k_xE_{ww} (top to bottom) as a function of λ_x.

appeared, the one near the wall at $\lambda_x^+ \approx 600$, and two others in the outer region respectively at $\lambda_x \approx 10h$ (large-scale motion) and $\lambda_x \approx 66h$ (very large-scale motions or superstructures).

The premultiplied spectra pertaining to the two other velocity components are also in good agreement with those found by Tsukahara *et al.* (2006). In particular, the wall-normal velocity spanwise premultiplied spectra ($k_z E_{vv}$) near the wall has a peak at $\lambda_z^+ \approx 50$, which is half the wavelength of other two components, exactly as for the second peak, at $\lambda_z/h \approx 2$ which also corresponds to half of the length associated to the streamwise velocity (see Kim *et al.*, 1987, for an interpretation of this).

Discussion. Our LES reproduce the essential features isolated in previous DNS. In particular, in addition to finding the well-known near wall cycle, we also reproduce the same bimodal behavior of spectra found in boundary layers (Hites (1997), Marusic (2001), Hutchins & Marusic (2007*a*)), channel flow (Jiménez (2007), del Álamo & Jiménez (2003), Jiménez *et al.* (2004), Hwang & Cossu (2010*b*)) and turbulent pipe flow (Bullock *et al.* (1978) and Guala *et al.* (2006)) with large and very large-scale motions of spanwise size $\lambda_z \approx 4.2 - 5h$ and respective length $\lambda_x \approx 10$ and ≈ 66 respectively.

3.3 Artificial quenching of the small-scale structures

In the previous section we have shown that 'reference' large eddy simulations in very large and wide boxes are able to capture the spectral energy peaks associated with the three important types of motions observed in turbulent Couette flow: the near-wall cycle ($\lambda_z^+ \approx 100$, $\lambda_x^+ \approx 600$), the large-scale motions (LSM, $\lambda_z \approx 4 - 5h$, $\lambda_x \approx 10h$) and the very large-scale motions (VLSM, $\lambda_z \approx 4 - 5h$, $\lambda_x \approx 65h$). It is important to understand the relation between these different motions.

It is now well accepted that the near-wall cycle is 'autonomous' because it also exists in minimal flow units, in the absence of motions at larger scale (Jiménez & Moin, 1991). It is however currently unclear if the motions at larger scales are forced by the near-wall cycle or if they could be sustained in the absence of these other motions. To ascertain if motions at large scale are or are not forced by those at smaller scales we use the method introduced by Hwang & Cossu (2010*c*, 2011) in turbulent channels. The idea is to quench motions at small scales by artificially increasing their dissipation by means of a LES filter. This is in practice realized by increasing the value of the Smagorinsky constant C_s in the static Smagorinsky model. The *static* Smagorinsky model is used because it avoids any positive energy flux from unresolved (small) to resolved (large) scales. When this model is used, one is therefore sure that large-scale motions are not forced by unresolved small-scale motions.

Results are obtained for $Re_\tau = 127$ where the separation of scales is clear and therefore the intepretation of the results is straightforward. The velocity field obtained for a given C_s is used to initialize the simulation at higher value of C_s. The 'adaptation' transients are then removed to compute the flow statistics and to analyze instantaneous fields. The increase in C_s has little effect on the friction Reynolds number eg $Re_\tau \approx 127$ at $C_s = 0.05$, $Re_\tau \approx 125$ at $C_s = 0.10$ and $Re_\tau \approx 121$ at $C_s = 0.14$.

Instantaneous flow fields. The instantaneous velocity fields obtained in the converged reference LES with $C_s = 0.05$ display an abundance of different scales characteristic of turbulent flows. Figure 3.4*a* shows an instantaneous flow field arbitrarily selected from the simulation data. We report, in particular, slightly negative levels of streamwise perturbation velocity (where the mean flow is removed) in half of the simulated numerical box. From the figure, two large-scale low speed streaks and small-scale motions are very evident. From figure 3.4 it is clearly seen that when the Smagorinsky constant is gradually increased ($C_s = 0.10$ in panel *b*, and $C_s = 0.14$ in

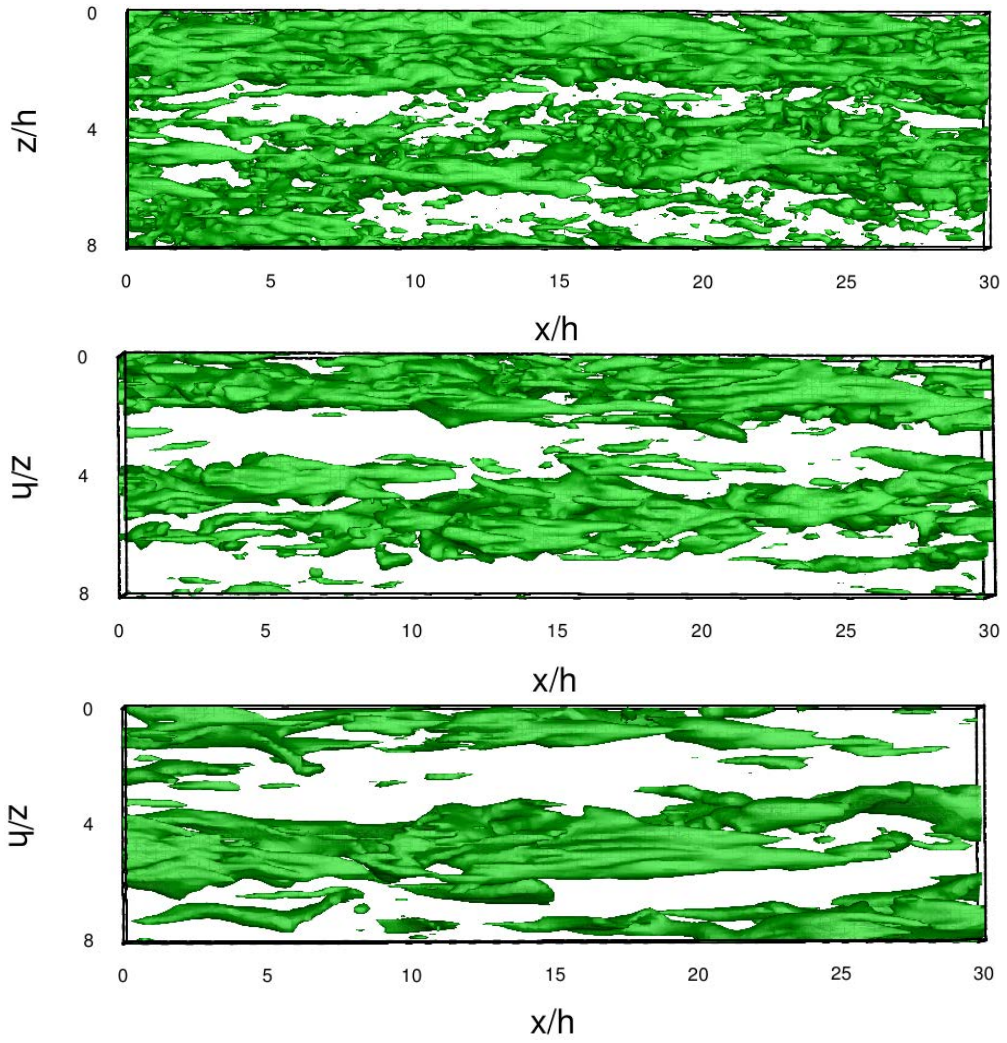

Figure 3.4: Iso-surface of instantaneous streamwise velocity fluctuations ($u^+ = -2.5$) at $Re_\tau = 127$ at $C_s = 0.05$, $C_s = 0.10$ and $C_s = 0.14$ (from top to bottom).

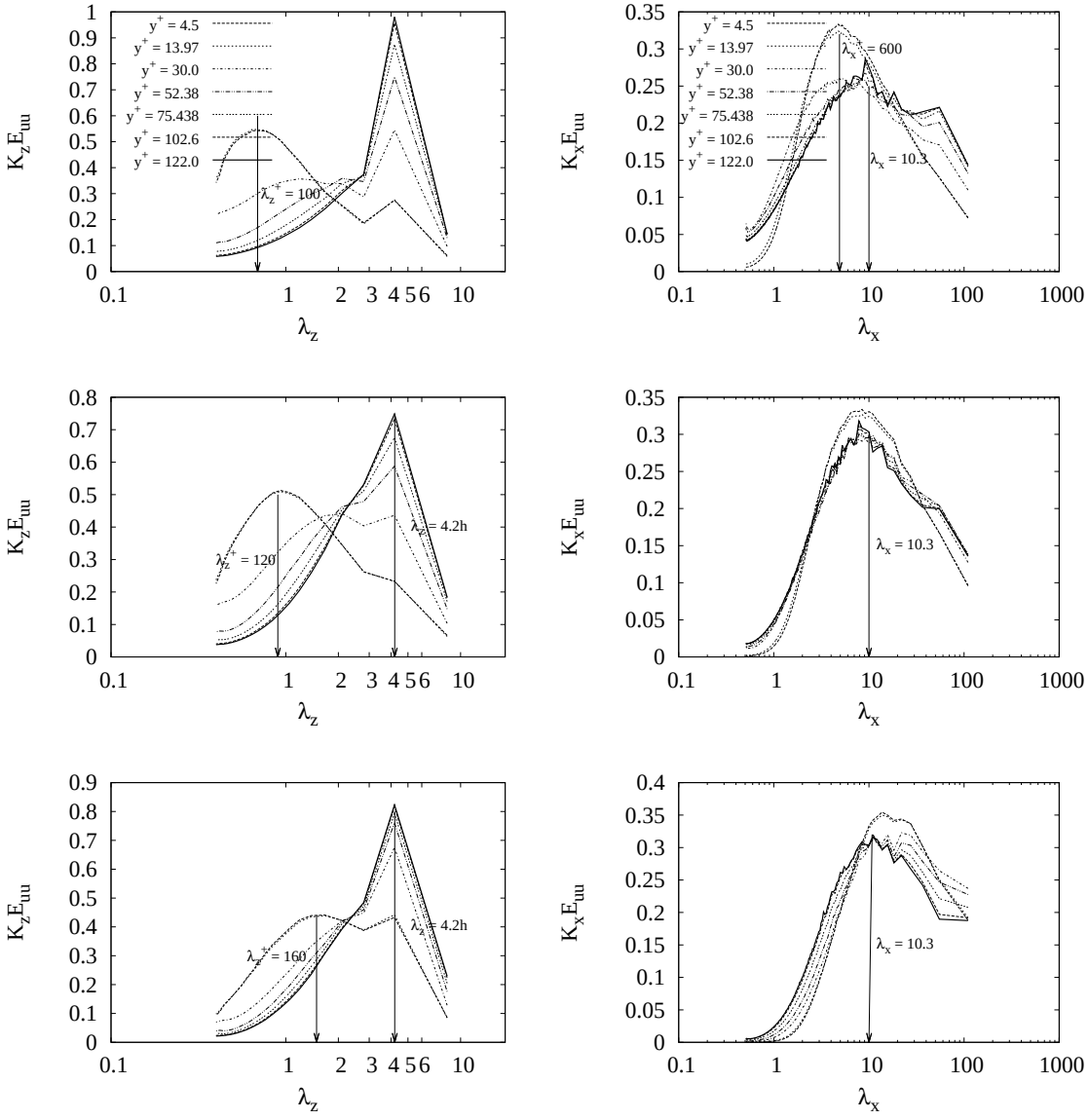

Figure 3.5: One-dimensional premultiplied spectra at $Re_\tau = 127$: Left panel shows spanwise spectra $k_z E_{uu}$ as a function of λ_z for increasing values of the Smagorinsky constant ($C_s = 0.05$,$C_s = 0.1$ and $C_s = 0.14$ top to bottom). Right panels shows the corresponding streamwise spectra $k_x E_{uu}$ as a function of λ_x. The selected values of the Smagorinsky constant are the same as in figure 3.4.

panel *c*), small-scale structures are gradually quenched while the structure (spacing, wavelength) of the large-scale streaks is essentially unaffected and becomes more clear.

Spanwise pre-multiplied energy spectra. The effects observed in flow snapshots are confirmed by the analysis of spanwise one-dimensional premultiplied spectra of the streamwise velocity shown in the left panels of figure 3.5. As C_s is increased from its reference value the peak at $\lambda_z \approx 100$ starts shifting towards larger wavelengths but, at the same time, the outer peak remains unchanged at $\lambda_z \approx 4.2h$. At $C_s = 0.14$ the near-wall cycle is suppressed and only the outer peak corresponding to the large and possibly very large-scale structures survives.

Streamwise premultiplied spectra. Streamwise premultiplied spectra corresponding to increasing values of C_s are reported in the panels on the right in figure 3.5. In the reference simulation ($C_s = 0.05$, panel *b*) peaks corresponding to LSM and VLSM are respectively visible at $\lambda_x \approx 10$ and $\lambda_x \approx 66$ while the one corresponding to the near wall cycle is at $\lambda_x^+ \approx 600$, corresponding to $\lambda_x \approx 5h$ at the Reynolds number considered. When C_s is increased the near wall cycle peak migrates towards higher wavelengths finally merging with the LSM peak at $\lambda_x \approx 10$. This essentially confirms what was already visible in the spanwise spectra: motions at large scale survive even when the near-wall cycle is suppressed, so that they must rely on a self-sustained mechanism. However, the more interesting effect detected from streamwise spectra is that the VLSM peak at $\lambda_x \approx 66$ is gradually quenched as C_s is increased. However, for $C_s = 0.14$, we observe a slight increase of the energy contained in the longest available wavelength $\lambda_x = 130$. It may therefore be possible that the VLSM peak is shifting to higher λ_x.

3.4 Discussion

Previous investigations have revealed the existence of large and very large-scale motions (LSM & VLSM) in turbulent plane Couette flow in addition to the well understood near-wall cycle. Here we have used the approach introduced by Hwang & Cossu (2010*c*) to show that:

- Large eddy simulations in very large and wide boxes at moderate Reynolds numbers are able to capture the most important features of turbulent Couette flow, namely the near-wall cycle and the large and very large-scale motions (LSM & VLSM).
- When the near-wall cycle is artificially quenched, the large-scale motions (LSM) do survive but not the very large-scale motions (VLSM).

As far as large-scale motions (LSM) are concerned, these results confirm those obtained by Hwang & Cossu (2010*c*) in the turbulent channel. The motions at large scale sustain also in the absence of the near-wall cycle. This further confirms that a self-sustained mechanism must be at work also at large scale. This mechanism is probably based on the non-modal amplification of large-scale coherent structures (del Álamo & Jiménez, 2006; Pujals *et al.*, 2009; Cossu *et al.*, 2009; Hwang & Cossu, 2010*a*,*b*; Willis *et al.*, 2010) and on the instability of large-scale coherent streaks of sufficiently large amplitude (Park *et al.*, 2011).

As for the very large-scale motions (VLSM), our results suggest that they are unable to self-sustain when motions at smaller scales are artificially quenched, implying that these motions probably receive some energy from smaller-scale motions. However, it is also possible that the VLSM characteristic scale moves to longer wavelengths in overdamped simulations. Additional investigations in longer numerical domains are therefore needed to clarify this issue.

In the next chapter, we focus on the self-sustained mechanism of large-scale motions, leaving the question of VLSM for future work.

Chapter 4

Nontrivial steady solutions and large-scale coherent motions in turbulent Couette flow

4.1 Scope of this chapter

In chapter 3 it has been shown that large-scale motions (LSM) with the characteristic size $\lambda_z \approx 4{-}5h$ and $\lambda_x \approx 10 - 12h$ are self-sustained, while the much longer very large-scale motions, having $\lambda_x \approx 60h$ are not self-sustained. The primary focus of this chapter is the analysis of the nature of the self-sustained mechanism supporting large-scale motions (LSM). We therefore consider a domain, that we label LSM-Box whose size $L_x \times L_z = 10.9h \times 5.3h$ roughly corresponds to the fundamental wavelength of LSM. This domain is also the 'optimum' domain considered by Waleffe (2003), as detailed in table 4.1. First, we analyze the turbulent dynamics in this domain and compare the results of reference large eddy-simulations to those of direct numerical simulations in the same domain and in larger domains. Then we verify that large-scale motions survive in these domains when the near wall motions are artificially quenched. Finally, and this is the main novelty of this chapter, we look for coherent large-scale steady solutions in the LSM-Box. These solutions are exact solutions of the filtered (LES) equations and not of the Navier-Stokes equations. The small-scale motions are not directly included in the solutions but only their averaged dissipative effect is included in the wave. This is important because it allows to capture the coherent part of large-scale motions without the need to solve the details of small-scale structures. As mentioned, the domain sizes we consider are very similar to the optimum domain sizes in which 'transitional' exact solutions have been found by Nagata (1990); Clever & Busse (1992) and Waleffe (2003) (see table 4.1). We will see in the following that this is not a mere coincidence and that those solutions are indeed much more related to self-sustained LSM motions than to near-wall cycles as initially believed.

4.2 Turbulent dynamics in a LSM-Box

Reference LES simulations. As a first step we performed direct numerical simulations and large eddy simulations at $C_s = 0.05$ and compared the turbulent mean and *rms* velocity profiles against those of Tsukahara *et al.* (2006) pertaining to DNS conducted in larger domains. Results obtained at Re=750 ($\mathrm{Re}_\tau = 52$) and Re=2150 ($\mathrm{Re}_\tau = 127$) are reported in figure 4.1 (top panels and bottom panels respectively).

Reference	L_x	L_z	N_x	N_y	N_z	Re	Re_τ	Δx^+	Δz^+
Nagata (1990)	7.9	4.2	-	-	-	300	27	-	-
Clever & Busse (1992)	8.4	4.0	-	-	-	400	33	-	-
Waleffe (2003), $\mathrm{Re}_\tau = 33$	10.9	5.5	31	32	32	400	33	11.6	5.8
DNS LSM-Box, $\mathrm{Re}_\tau = 52$	10.9	5.3	48	81	48	750	52	11.8	5.8
LES LSM-Box, $\mathrm{Re}_\tau = 52$	10.9	5.3	32	61	32	750	52	17.7	8.2
DNS LSM-Box, $\mathrm{Re}_\tau = 127$	10.9	5.3	96	81	96	2150	127	14.3	7.0
LES LSM-Box, $\mathrm{Re}_\tau = 127$	10.9	5.3	32	61	32	2150	127	43.2	21.0

Table 4.1: Computational domains and discretization parameters used in previous investigations where TW were computed compared to the parameters used in the present study. The highest Reynolds number at which results have been presented by Nagata (1990), Clever & Busse (1992) and Waleffe (2003) is reported.

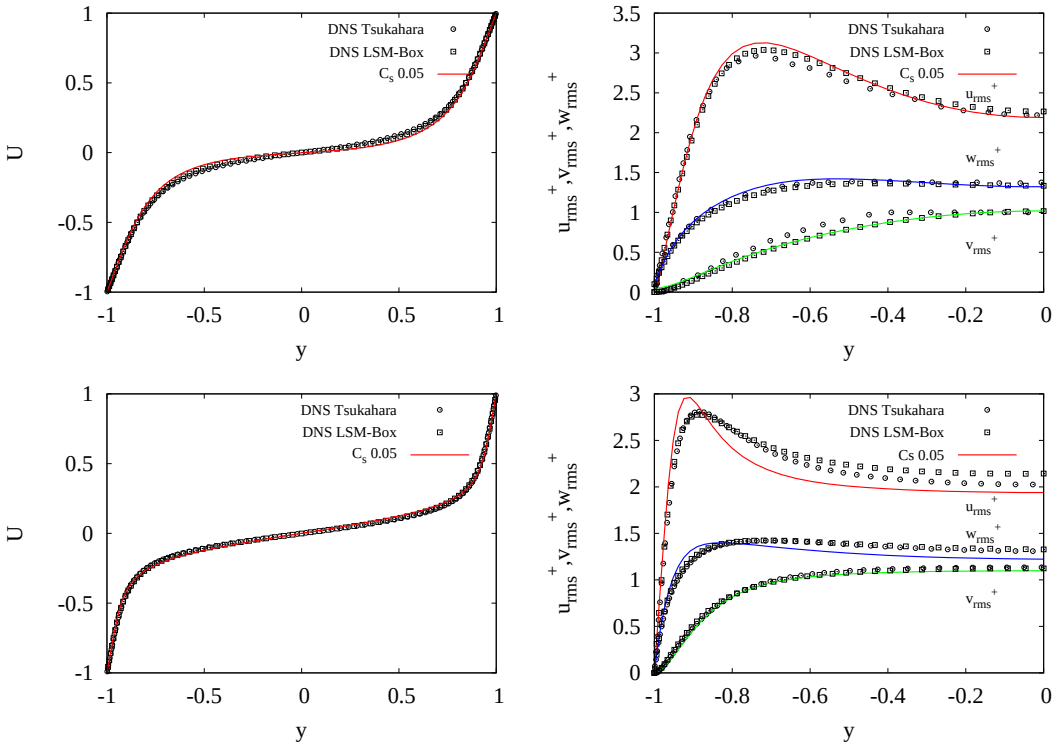

Figure 4.1: Mean flow (panels on the left) and turbulent fluctuations (panels on the right) profiles computed for $\mathrm{Re}_\tau = 52$ (top row) and $\mathrm{Re}_\tau = 127$ (bottom row) in a LES box. The reference LES data ($C = 0.05$) are compared to DNS in the same LSM-Box and to the DNS data of Tsukahara *et al.* (2006) obtained in very wide and long domains.

Mean and rms velocity profiles of reference simulations. The mean velocity profiles are in good agreement between the LES, the DNS and the DNS in large domains. The agreement of the *rms* profiles is good at $Re = 52$ but deteriorates at $\mathrm{Re}_\tau = 127$ especially for the LES results which are probably too dissipative with the chosen static Smagorinsky model and the large grid spacing. Indeed, at $\mathrm{Re}_\tau = 127$ the grid spacing used in the LES fails to accurately resolve the energy-producing near-wall motions and the static Smagorinsy model filters out the 'physical' energy backscatter and at the reference value $C_s = 0.05$.

Premultiplied spectra of reference simulations. The streamwise ($k_x E_{uu}$) and spanwise ($k_z E_{uu}$) pre-multiplied spectra of streamwise velocity are reported in the top row of figure 4.2 and figure 4.3 at $\mathrm{Re}_\tau = 52$ and $\mathrm{Re}_\tau = 127$, respectively. The peaks associated to the near wall cycle are well captured even in this LSM-Box and correspond to those observed in the VLSM-Box (see figures 3.2 and 3.3). The peaks corresponding to LSM correspond, in the LSM-Box, to the largest length observable in the box and are therefore locked to the box size $\lambda_x = 5.3h$ and $\lambda_x = 10.88h$ for both Reynolds numbers. Of course, the VLSM peak is out of the picture in this box.

Quenching the near wall cycle. Similarly to what was already done in the VLSM-Box, as discussed in section 3.3, we verify if the large-scale motions survive when the near-wall cycle is artificially quenched by increasing the Smagorinsky constant C_s. We investigate the issue at both Re=750 ($\mathrm{Re}_\tau = 52$) and Re=2150 ($\mathrm{Re}_\tau = 127$) by increasing C_s from its reference value $C_s = 0.05$ to $C_s = 0.10$ and finally to $C_s = 0.14$. The streamwise ($k_x E_{uu}$) and spanwise ($k_z E_{uu}$) pre-multiplied spectra of streamwise velocity are reported in figure 4.2 and figure 4.3 for $\mathrm{Re}_\tau = 52$ and $\mathrm{Re}_\tau = 127$, respectively. Following the usual trend, the $\lambda_z^+ \approx 100$ peak in $k_z E_{uu}$ corresponding to the near wall cycle is quenched for increasing C_s, while the peak corresponding to LSM, $\lambda_z = 5.3h$ in this box, survives the quenching of the near wall cycle. Similarly, at $\mathrm{Re}_\tau = 127$, the $\lambda_x^+ \approx 600$ peak in $k_x E_{uu}$ corresponding to the near wall cycle is quenched when C_s is increased, while the peak corresponding to LSM, $\lambda_x = 10.8h$ in this box, survives the quenching of the near wall cycle. This is not observed at $\mathrm{Re}_\tau = 52$ because the two streamwise peaks are not separated at this low Reynolds number, exactly like what observed in the VLSM-Box. These results confirm that the restriction to a LSM box does not affect qualitatively the LSM self-sustained process.

4.3 Coherent large-scale steady solutions at Re=750

Motivation. We now turn to one of the most important questions motivating this thesis: is there a 'skeleton' of large-scale invariant coherent solutions associated to the large-scale motions? In other words, is it possible to compute e.g. steady solutions for the resolved motions in the LES equations similarly to what has been done for the Navier-Stokes equations in the transitional regime?

Finding the edge state in the overdamped simulations ($C_s = 0.14$). It is observed from the one-dimensional premultiplied spectra that for $C_s = 0.14$ the near-wall cycle is damped and only the large-scale dynamics survives. In the transitional case ($Re = 400$), using the Navier-Stokes equations Viswanath (2007) and Schneider *et al.* (2008) had shown that the edge state of plane Couette flow is a nonlinear-steady states, which corresponds to the lower branch of the Nagata-Clever-Busse-Waleffe solutions. The edge was found using a standard 'edge-tracking' technique based on bisections. We therefore apply the same technique to find the edge state in the overdamped LES simulations at $C_s = 0.14$ and at a Reynolds number in the low-turbulent regime at Re=750 ($\mathrm{Re}_\tau = 52$). The initial condition given to the LES simulations consists of the mean turbulent

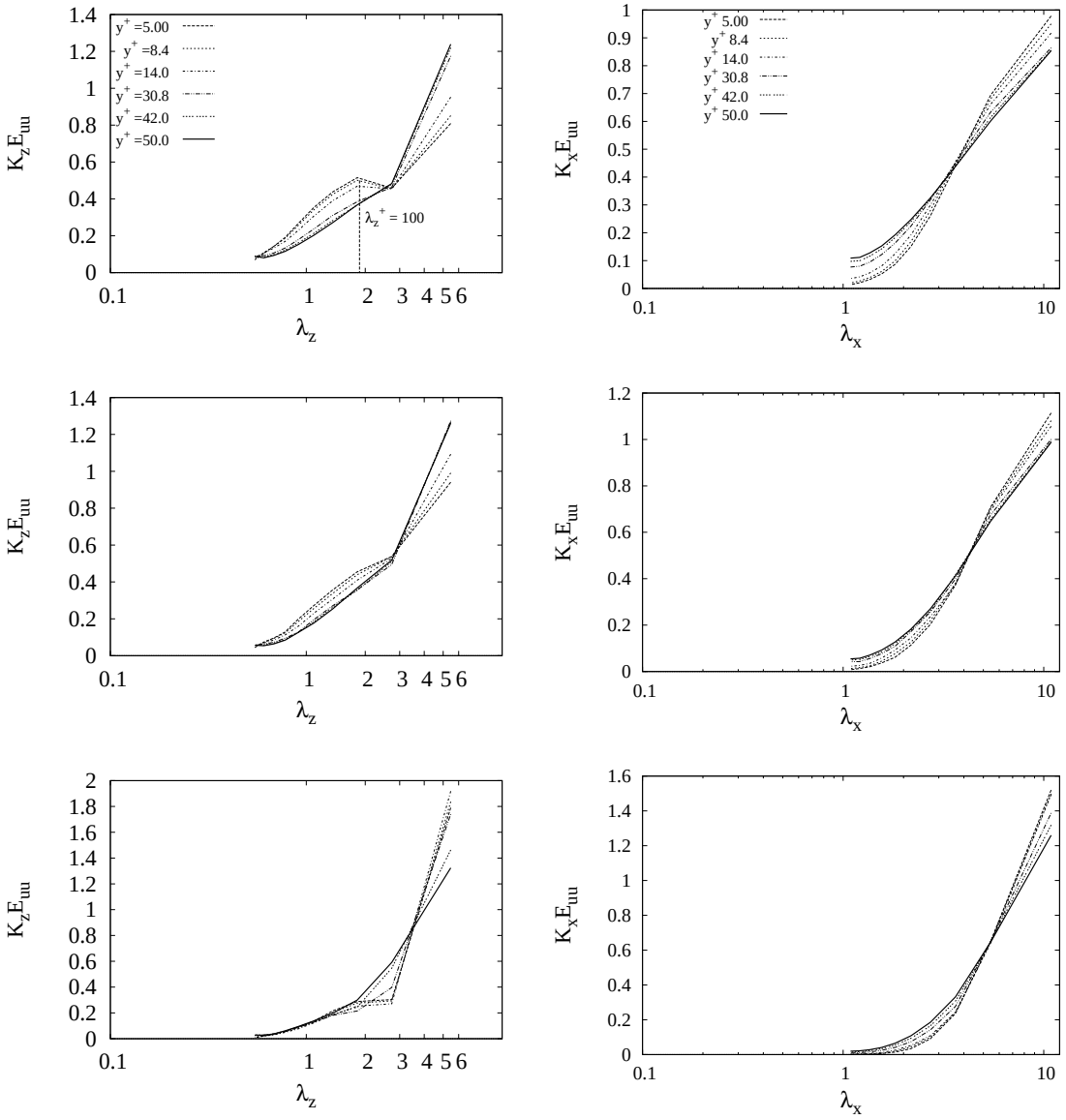

Figure 4.2: One-dimensional premultiplied spectra at Re=750 ($\mathrm{Re}_\tau = 52$). Left panels: spanwise premultiplied spectra $k_z E_{uu}(\lambda_z)$. Right panels: streamwise premultiplied spectra $k_x E_{uu}(\lambda_x)$. The values of the Smagorinsky are (top to bottom): $C_s = 0.05$, $C_s = 0.10$ and $C_s = 0.14$.

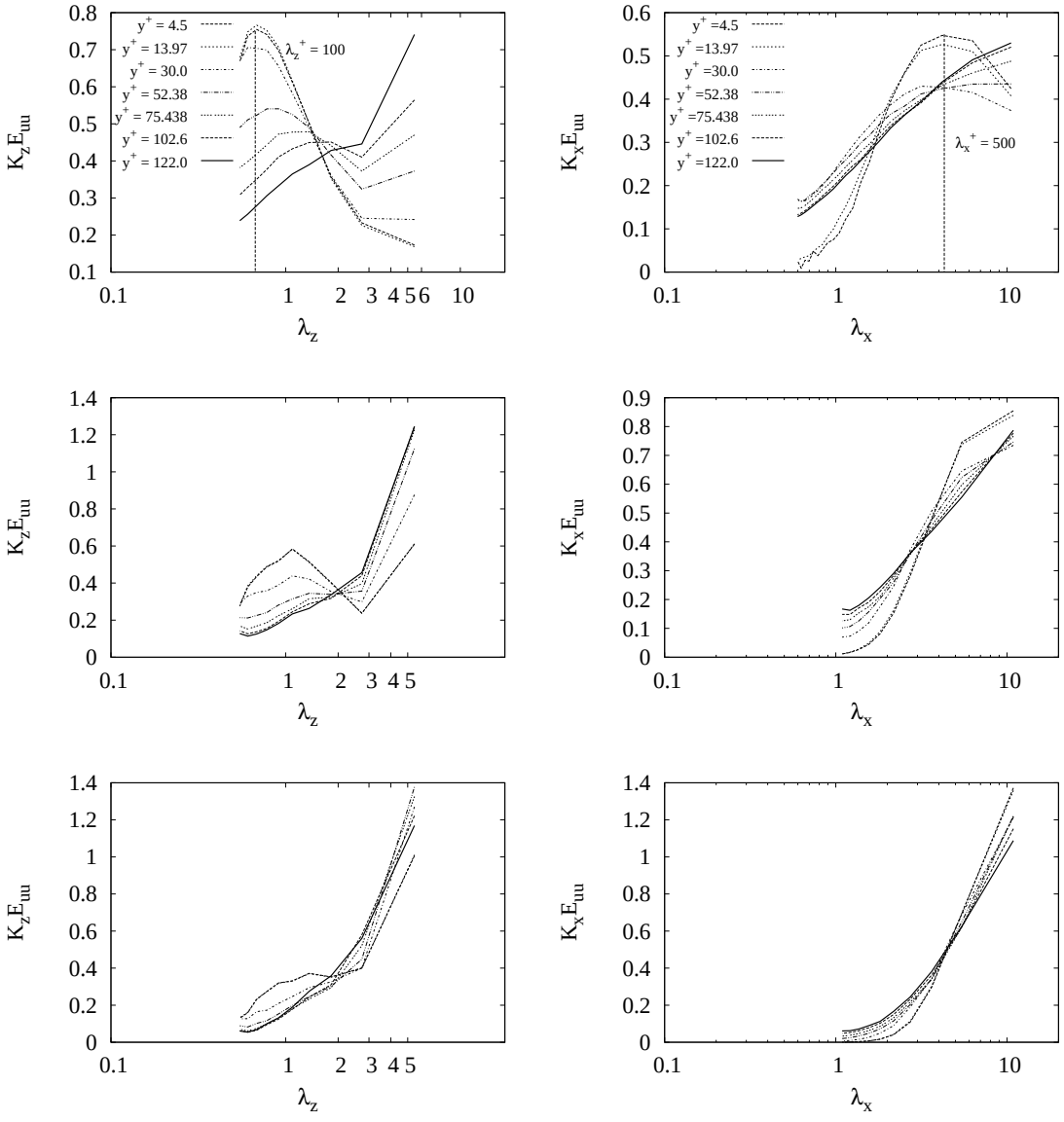

Figure 4.3: One-dimensional premultiplied spectra at Re=2150 ($\mathrm{Re}_\tau = 127$). Left panels: spanwise premultiplied spectra $k_z E_{uu}(\lambda_z)$. Right panels: streamwise premultiplied spectra $k_x E_{uu}(\lambda_x)$. The values of the Smagorinsky are (top to bottom): $C_s = 0.05$, $C_s = 0.10$ and $C_s = 0.14$.

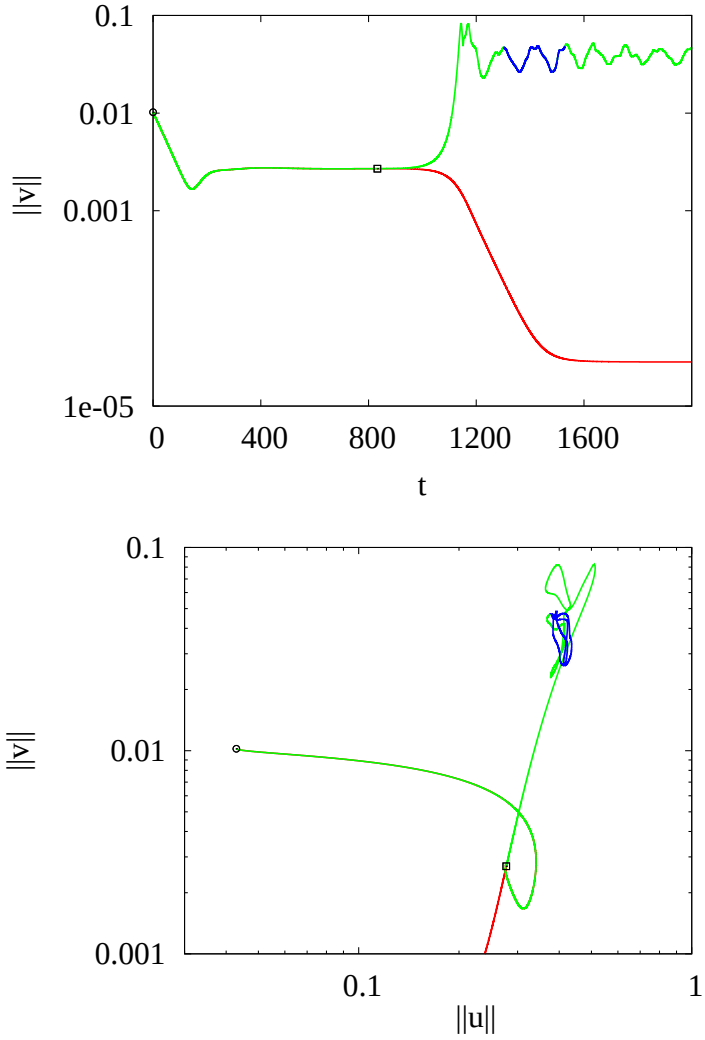

Figure 4.4: Edge tracking at Re=750 ($\mathrm{Re}_\tau = 52$) and $C_s = 0.14$. Two initial conditions (triangle symbol) lying almost on the edge of chaos surface initially remains near the surface while being attracted to the TW edge state (square symbol). The solution lying on the laminar side of the edge is then quickly attracted to the laminar solution (solid, red line) while the other one goes to the non-trivial state (green line, dotted). The trajectories are shown in both the $\|v\| - t$ (top panel) and in the $\|u\| - \|v\|$ plane (bottom panel) displaying the streaks-vortices dynamics.

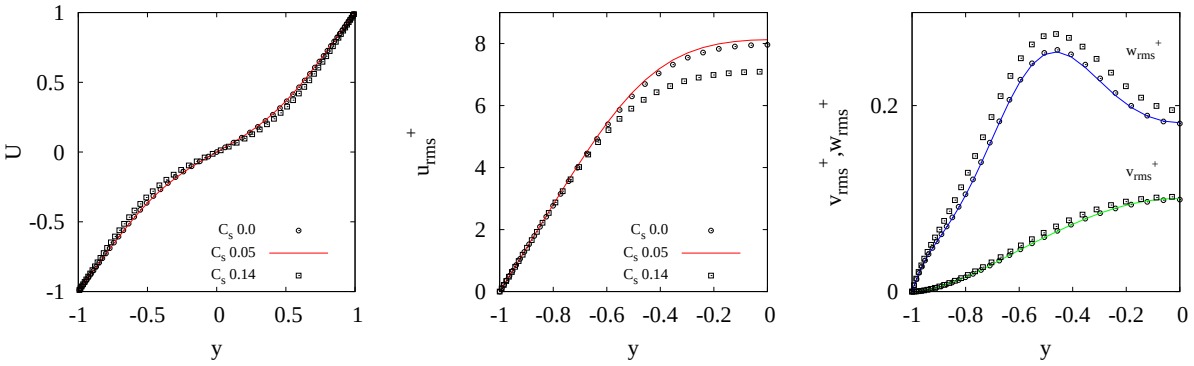

Figure 4.5: Lower branch steady solutions in the LSM-Box at $\mathrm{Re}_\tau = 52$: mean flow (panel *a*), streamwise (panel(*b*) and cross-stream (panel *c*) *rms* velocity profiles corresponding to the cases $C_s = 0.14$, for which the initial guess was obtained from edge-tracking), $C_s = 0.05$ corresponding to a reference LES and $C_s = 0$ corresponding to the Navier-Stokes steady solution. The last two solutions where obtained by continuation in C_s.

flow to which is added a pair of streamwise uniform counter-rotating rolls along with a sinuous perturbation of the spanwise velocity, which is similar to the one used by Cossu *et al.* (2011):

$$\mathbf{v}_0 = \{U(y), 0, 0\} + A_0 \left\{0, \frac{\partial \psi_0}{\partial z}, -\frac{\partial \psi_0}{\partial y}\right\} + 0.1\, A_0 \{0, 0, w_{sin}\} \tag{4.1}$$

where

$$\psi_0(y,z) = \left(1-y^2\right) \sin\left(\frac{2\pi z}{L_z}\right); \quad w_{sin}(x,y) = \left(1-y^2\right) \sin\left(\frac{2\pi x}{L_x}\right). \tag{4.2}$$

with $L_z = 5.3$ and $L_x = 10.88$. The bisection is performed by adjusting the amplitude A_0 of the perturbations. After an initial transient, the solution on the edge converges to a non-trivial steady state, as shown in figure 4.4. The pseudo-periodic oscillations of the weakly 'turbulent' solution do not correspond to a cycle, as can be seen from the blue line in the figure. We have confirmed that the edge state found is a nonlinear-steady solution by converging it by means of Newton-Krylov iterations with `Peanuts` initialized with the edge state. The solution has zero phase speed and is therefore a steady solution of the Navier-Stokes equations. The mean and *rms* velocity profiles of the lower branch solution are reported in figure 4.5, from where it is seen that this is a typical lower branch solution with most of the energy concentrated in the streaky motions which are forced by low-amplitude quasi-streamwise vortices.

Relation between the lower branch LSM-TW and the corresponding Navier-Stokes solution. The 'coherent' lower branch LSM solution is very similar to the lower branch Nagata-Clever-Busse-Waleffe solutions found in similar boxes using the Navier-Stokes equations. It is therefore interesting to investigate the relation between these solutions. This is done by continuing the steady solution in C_s by first decreasing from $C_s = 0.14$ to the reference value $C_s = 0.05$ and by then reducing it to $C_s = 0.0$ which corresponds to the Navier-Stokes equation as clear from eq. (2.4). The continuation is performed by reducing C_s in small steps[1] using an automatic continuation method as explained in §A.1. The mean and *rms* velocity profiles corresponding to $C_s = 0.14$, $C_s = 0.05$ and $C_s = 0$ are shown in figure 4.5. From this figure it is seen that these three solutions are very similar.

[1]Five intermediate steps have been used to go from $C_s = 0.14$ to $C_s = 0.05$ and 3 steps to go from $C_s = 0.05$ to $C_s = 0$

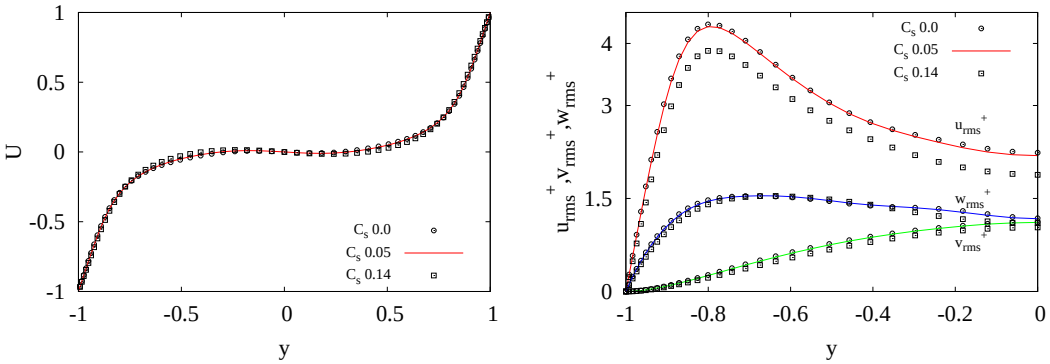

Figure 4.6: Upper branch TW in the LSM-Box at Re=750 ($Re_\tau = 52$): mean flow (panel *a*), streamwise and cross-stream *rms* velocity profiles (panel *b*) corresponding to the cases $C_s = 0.14$, $C_s = 0.05$ corresponding to a reference LES and $C_s = 0$ corresponding to the Navier-Stokes steady solution.

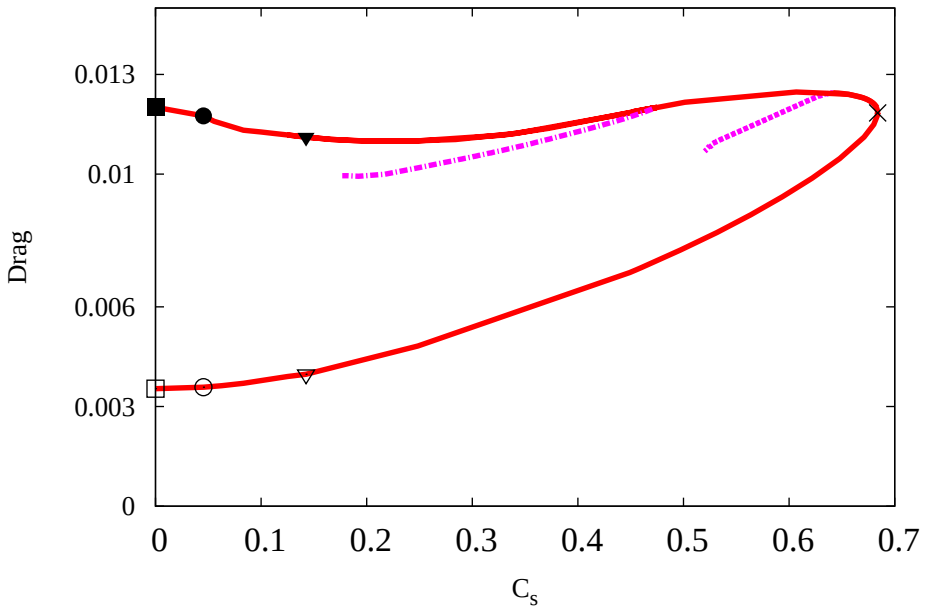

Figure 4.7: Continuation diagram of steady solutions in the parameter C_s (Smagorinsky coefficient) at Re = 750 ($Re_\tau = 52$). The red (solid) line corresponds to the symmetric solutions while the dashed (magenta) lines correspond to non-symmetric branches. The symbols denote the solutions found at $C_s = 0$ (Navier-Stokes), $C_s = 0.05$ (reference LES) and $C_s = 0.14$ (overdamped LES where the edge-tracking has been performed.

Continuation to larger C_s. Having found that lower branch LSM solutions are essentially a continuation of the Navier-Stokes solutions into the coherent turbulent regime, we now investigate if the same happens for upper branch solutions. This is done by first recomputing the Navier-Stokes upper branch steady solutions ($C_s = 0$) in the LSM-Box and by then continuing these solutions to higher C_s using pseudo arc-length continuations (as described in §A.1). This is very important because the vast literature on the Navier-Stokes transitional regime indeed shows that upper (and not lower) branch solutions are the ones around which the turbulent state is organized (Waleffe, 2003; Kerswell, 2005; Eckhardt *et al.*, 2007).

As for the lower branch, the solutions found for the mean and *rms* velocity profiles corresponding to $C_s = 0.14$, $C_s = 0.05$ and $C_s = 0$, shown in figure 4.6 are very similar. Pushing the continuation of the upper and lower branches to higher values of C_s we find that the upper and lower branch are connected in C_s through a saddle-node bifurcation, as shown in figure 4.7. This means that the turbulent coherent self-sustained states are based on essentially the same process of the transitional structures which appear at low Reynolds number. The main effect of small-scale motions is essentially to provide additional (spatially non-uniform) dissipation and not to sustain the LSM motions.

Mathematically, the continuation to larger C_s is a well-suited procedure to obtain e.g. upper branch solutions from lower branch ones which can be obtained starting from edge-tracking simulations. Physically, however, it should be kept in mind that while solutions at moderate values of C_s (e.g. $C_s = 0.14$) still have some resemblance to the 'real' large scale motions because the unphysical overdamping of small-scale motions does not affect too much the solution, solutions at larger C_s, such as the one in the saddle-node bifurcation point, are too overdamped to be compared to real motions. This is why we do not discuss in details these solutions in the high C_s regime, despite their mathematical convenience.

Non-symmetric additional upper branch steady solutions While continuing the solutions from the upper to the lower branch, if no symmetry conditions are enforced, the continuation algorithm may capture non-symmetric solutions, shown as dashed-dotted (magenta) lines in figure 4.7. The continuation of these additional solutions to lower, more 'realistic' values of C_s, has however been impossible and we therefore do not discuss them in details.

4.4 Reynolds continuation of large-scale steady solutions

Continuation to lower Reynolds numbers and relation to the Nagata-Clever-Busse-Waleffe solutions In the previous section we have seen that the large-scale steady solutions obtained using a LES modelling of subgrid scales can be continued to Navier-Stokes solutions at the same Reynolds number and that these solutions are very similar to the Nagata-Clever-Busse-Waleffe solutions. As a first additional step we have therefore continued our steady Navier-Stokes solutions ($C_s = 0$) obtained at Re=750 to lower Reynolds numbers. As shown in figure 4.8, we find the well-known saddle-node bifurcation at $Re = 127$ already found by (Nagata, 1990) and Waleffe (2003) and the solutions at Re=400 are identical to those computed in these previous investigations. This definitively confirms that the large-scale steady solutions found with LES subgrid scale modelling are continuously linked to the transitional Nagata-Clever-Busse-Waleffe solutions of the Navier-Stokes equations.

Continuation to higher Reynolds numbers The steady solutions described in §4.3 have been computed at Re=750 ($\mathrm{Re}_\tau \approx 52$), which, while larger than the transitional value $Re \approx 350$, is not sufficiently large to display a well-defined scale separation between the near-wall and large-scale structures (see also all the discussion in chapter 3). It therefore would be desirable to compute

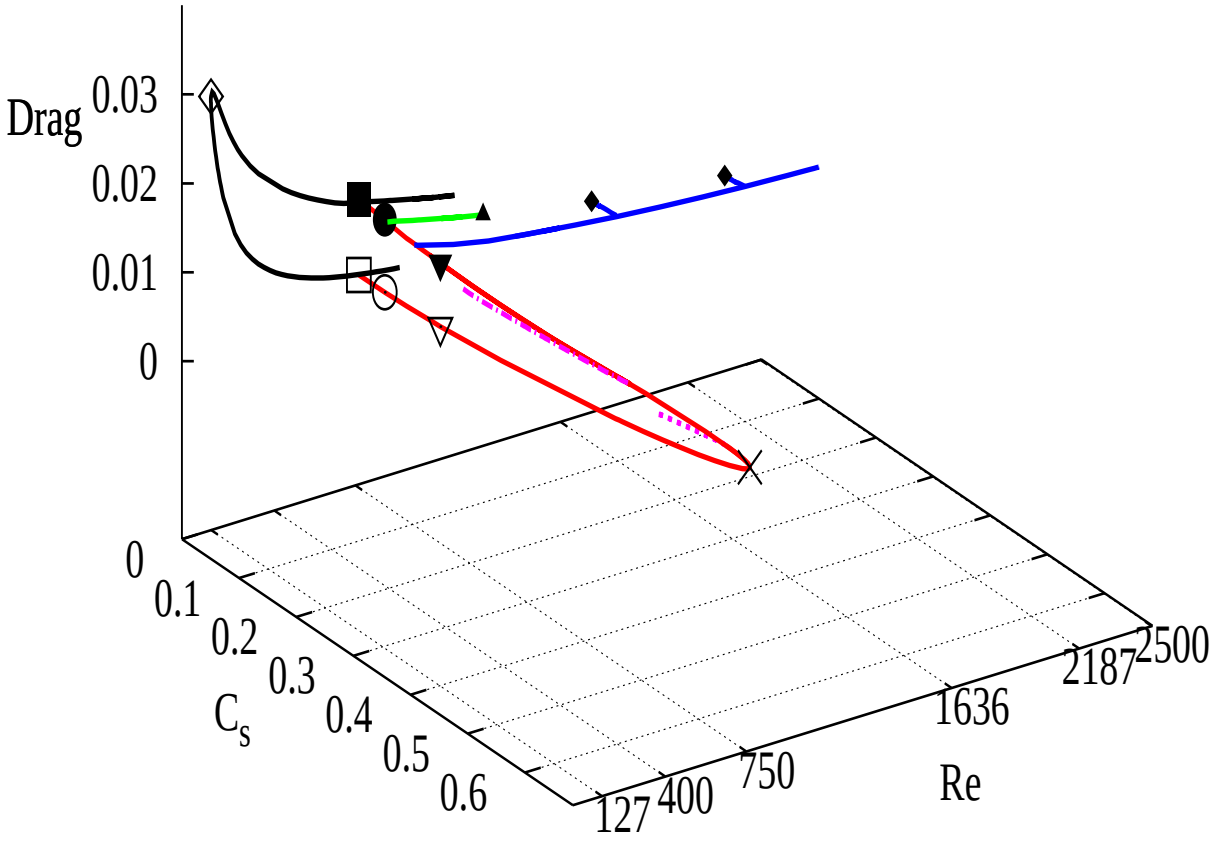

Figure 4.8: Continuation diagram of steady solutions in the parameters C_s (Smagorinsky coefficient) and Re (Reynolds number). The solid (red) line continuation in C_s has already been presented in figure 4.7. The continuation in Reynolds number at $C_s = 0$ (black line) describes the Navier-Stokes Nagata-Clever-Busse-Waleffe solution and finds the well-known saddle node bifurcation at Re = 126. It has been possible to directly continue the $C_s = 0.05$ solution from Re = 750 to Re = 1164 (green line). Coherent steady solutions at high Reynolds numbers are found by first continuing to larger Re solutions obtained for $C_s = 0.1$ and then continuing these solutions to $C_s = 0.05$ (blue line).

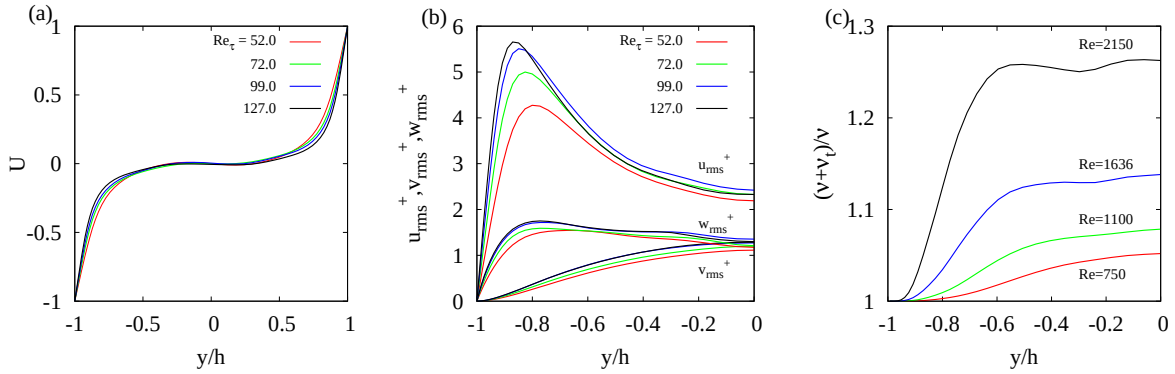

Figure 4.9: Upper branch steady solutions obtained for increasing Reynolds numbers for $C_s = 0.05$ in the LSM-Box. (a) mean flow, (b) *rms* velocity profiles and (c) *rms* eddy viscosity associated to subgrid scale motions.

steady solutions at higher Reynolds numbers, e.g. $\mathrm{Re}_\tau = 127$ corresponding to Re=2150. We concentrate on solutions on the upper branch which are relevant for the turbulent dynamics. Solutions on the lower branch are related to the transition problem which is probably less relevant at these high Reynolds numbers. A continuation in Reynolds numbers at $C_s = 0$ and $C_s = 0.05$ fails to converge for Reynolds numbers larger than $Re \approx 1164$ ($\mathrm{Re}_\tau \approx 74$) when $C_s = 0.05$. For the Reynolds numbers where the solutions converge (up to $Re_\tau \approx 74$) the two solutions are very similar. To circumvent this blockage point we followed an alternate path in the parameter space, as shown in figure 4.8. In particular, we were successful in continuing the $C_s = 0.1$ solution up to $Re \approx 2500$. We have then reduced C_s up to $C_s = 0.05$ at selected Reynolds numbers ranging up to $Re = 2187$. For this last Reynolds number, corresponding to $\mathrm{Re}_\tau \approx 128$, however we were able to reduce C_s only to $C_s = 0.06$. With the chosen resolution we were unable to continue the solutions to even larger values of the Reynolds numbers. We have not attempted to increase the numerical resolution for essentially two reasons. The first is merely computational. The dimension of our state vector is already larger than 60 000, which is at the upper end of what we can computationally afford in Newton-Krylov methods. Also, if the resolution is changed, so is the eddy viscosity, so that the branch computation should be probably restarted from scratch, which was not affordable in the limited time of this PhD. We therefore leave the very high Reynolds number issue to future study.

Continuation of the upper branch solutions to higher Re The mean and *rms* velocity profiles of the reference ($C_s = 0.05$ and $C_s = 0.06$) solutions obtained at these larger Reynolds numbers are displayed in figure 4.9. The mean flow associated to these solutions remains similar to the turbulent one also in its deformation associated to large Reynolds numbers. The streamwise velocity *rms* profile displays a slight increase of the streak amplitude in wall units and a slight shift of their maximum amplitude towards the wall. This shift towards the wall is consistent with what is observed in the *rms* profiles of DNS of turbulent flows. The change of the wall-normal and spanwise *rms* velocity profiles with the Reynolds number is however minor. From figure 4.10 we see that the structure of the steady solutions does not change much when the Reynolds number is increased. However, the eddy viscosity associated to the unresolved motions increases with the Reynolds number and is located mainly on the flanks of the low speed streak. The absolute levels of eddy viscosity are not huge even at Re = 2150 where the maximum of ν_t does not exceed 90% of the molecular viscosity for those solutions but, in contrast to from the Navier-Stokes case, the eddy viscosity is not spatially uniform.

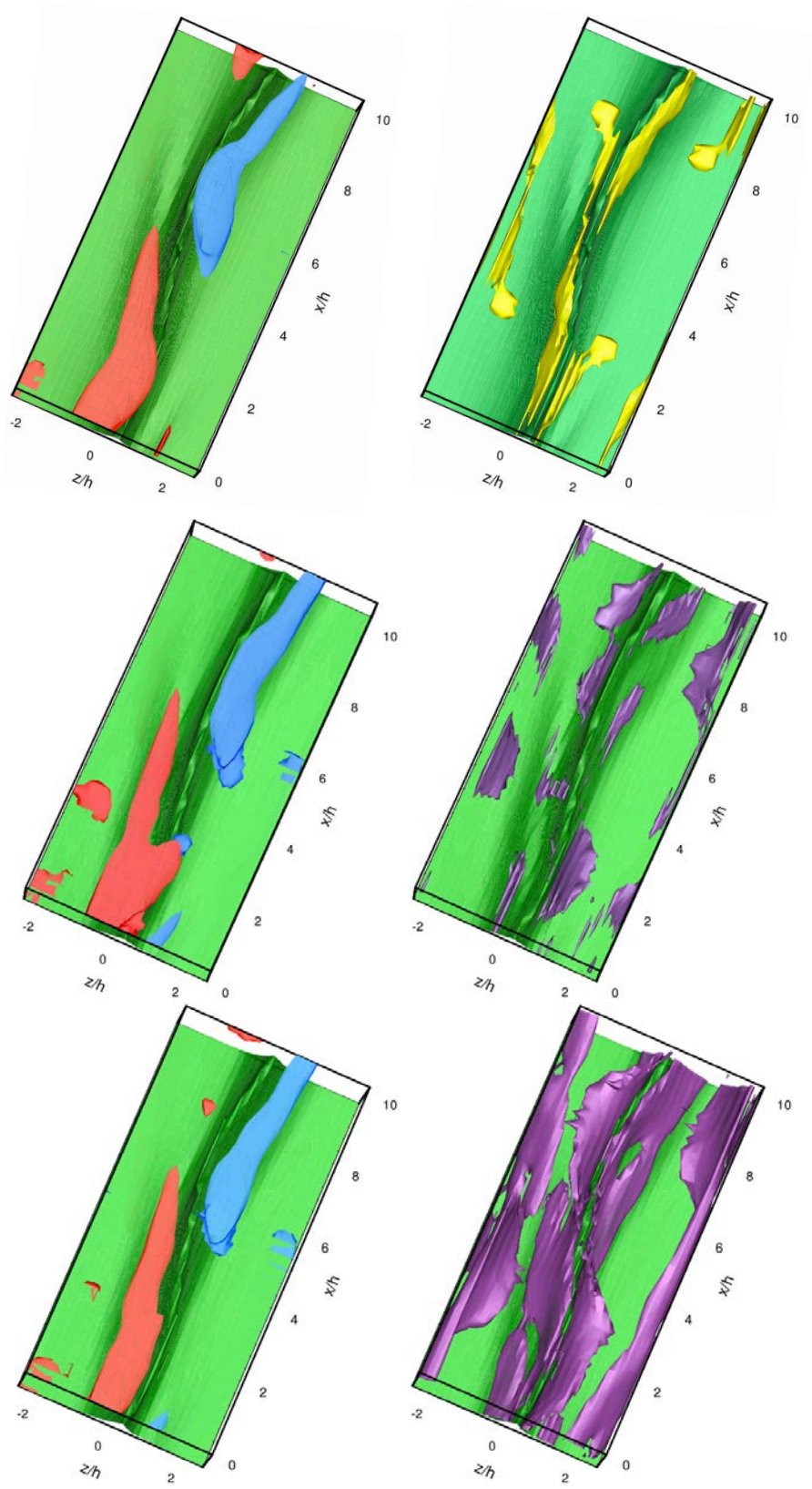

Figure 4.10: Visualisation of the upper branch LSM 'turbulent' steady solutions obtained with $C_s = 0.05$ and for increasing values of the Reynolds number: Re=750 (corresponding to $Re_\tau = 52$, top row), Re=1636 (corresponding to $Re_\tau = 99$, middle row), Re=2150 (corresponding to $Re_\tau = 127$, bottom row). The panels on the left represent the streaks and quasi-streamwise vortices: the green surface represents the values where the streamwise velocity is 50% of its maximum value while the blue and red surfaces correspond streamwise vorticity values equal to ±70% of the maximum. The panels on the right represent the streaks and the relative eddy-viscosity associated to the filtered small-scale motions. The green surface is the same as in the left panel, while the violet surfaces correspond to $\nu_t/\nu = 40\%$ and the yellow one to $\nu_t/\nu = 10\%$.

4.5 Scale separation: large-scale or near wall solutions?

In §4.4 it has been shown that large-scale steady solutions can be continued to higher Reynolds numbers in the $L_z \times L_x = 5.3h \times 11h$ LSM-Box, which has the dimensions of 'real' large-scale motions (LSM) observed in the turbulent regime. The upper branch solutions display features which are consistent with the observed large-scale motions even if, as is the case of all steady solutions found steady solutions, they do not capture alone the entire turbulent statistics except in the early transitional regime, say at Re=400. Nagata-Clever-Busse-Waleffe steady solutions are, however, often discussed with respect to the near-wall cycle. For instance, Waleffe (2003) emphasizes that the optimum parameters, for which the saddle-node bifurcation appears at the lowest Reynolds number, correspond to $\lambda_z^+ \approx 100$, which is characteristic of the wall cycle; Jiménez *et al.* (2005) and Kawahara *et al.* (2012) also discuss these structures with respect to the near-wall cycle dynamics despite the fact that the solutions are analyzed for Reynolds numbers lower than Re=600 at which no scale separation exists between the scales of the near-wall cycle and those of large-scale motions. One interesting question therefore is: can the Nagata-Clever-Busse-Waleffe solutions be continued into near-wall cycle structures in a way similar to what has been done in the LSM-Box? We address this issue in the case of the Navier-Stokes equations ($C_s = 0$). Solutions describing the near-wall cycle must scale in inner-units. Continuation of these solutions to higher Reynolds numbers therefore should be done keeping the box dimension *fixed in inner units*. As $L_z^+ = \mathrm{Re}_\tau L_z$, when Re_τ is increased, L_z must be decreased in order to keep constant L_z^+, and similarly for L_x.

The size of the LSM-Box at Re=400, for which the original solution of Waleffe (2003) is available is, in inner units, equivalent to $L_z^+ \approx 180$ and $L_x^+ \approx 360$. Therefore, we first continued the solution at Re=400 in the parameters L_x and L_z to achieve $L_z^+ \approx 100$ and $L_x^+ \approx 200$ which in external units corresponds to $L_z = 2.6$ and $L_x = 5.51$ (see also Gibson *et al.*, 2008). Then we performed a series of DNS to get an approximate relation between Re_τ and Re, which in plane Couette flow is found to be $\mathrm{Re}_\tau \approx 0.054\,\mathrm{Re} + 11.22$, for $\mathrm{Re} \in [400, 2150]$. A function $\mathrm{Re}_\tau(\mathrm{Re})$ is indeed necessary in order to convert L_z^+ and L_x^+ to L_z and L_x at a given Reynolds number Re (which is the actual parameter of the continuation). Finally, a continuation in Re is started from the Re=400 solution. At the $n-th$ step of the continuation a converged solution $\mathbf{u}^{(n)}$ has been obtained at $Re = Re^{(n)}$ where we know the friction velocity $u_\tau^{(n)}$ and the frictional Reynolds number $\mathrm{Re}_\tau^{(n)}$. The dimensions $L_x^{(n)}$ and spanwise length $L_z^{(n)}$ given in outer units are such that $L_z^+ \approx 100$ and $L_x^+ \approx 250$. The solution procedure then proceeds as follows;

1. Choose an appropriate Reynolds number Re^{n+1}, and compute an approximate Re_τ^{n+1}.

2. Predict the approximate frictional velocity $u_\tau^{n+1}/U_{ref} = Re_\tau^{(n+1)}/Re^{(n+1)}$

3. Predict the solution $\mathbf{u}^{n+1}$ at $Re^{(n+1)}$ as follows

$$\frac{\mathbf{u}^{n+1}}{u_\tau^{n+1}} = \frac{\mathbf{u}^n}{u_\tau^n} \tag{4.3}$$

   This relation is based on the assumption that the near wall solution would probably scale in inner units.

4. Compute the new box dimension in outer units such that:

$$L_z^{n+1} = L_z^n \left(\frac{Re_\tau^n}{Re_\tau^{n+1}} \right) \quad ; \quad L_x^{n+1} = L_x^n \left(\frac{Re_\tau^n}{Re_\tau^{n+1}} \right) \tag{4.4}$$

   This relation explicitly keeps the domain size constant in inner units.

Re	Re_τ	L_x^+	L_z^+	L_x	L_z	u^+_{max}	y^+_{max}
400	33.3	180 ∼ 190	80 ∼ 90	5.51	2.60	2.8	11.1
650	46.2	240 ∼ 250	103 ∼ 108	5.19	2.36	3.2	13.8
750	52.7	240 ∼ 250	105 ∼ 110	4.61	2.10	3.3	14.8
950	63.7	240 ∼ 250	98 ∼ 105	3.82	1.74	3.5	16.2
1100	71.2	240 ∼ 250	104 ∼ 110	3.51	1.60	3.7	18.2
1300	83.2	240 ∼ 250	98 ∼ 103	2.75	1.25	3.8	21.7
1600	99.1	240 ∼ 250	104 ∼ 110	2.44	1.11	3.9	23.4

Table 4.2: Computational domains fixed in inner units during continuation.

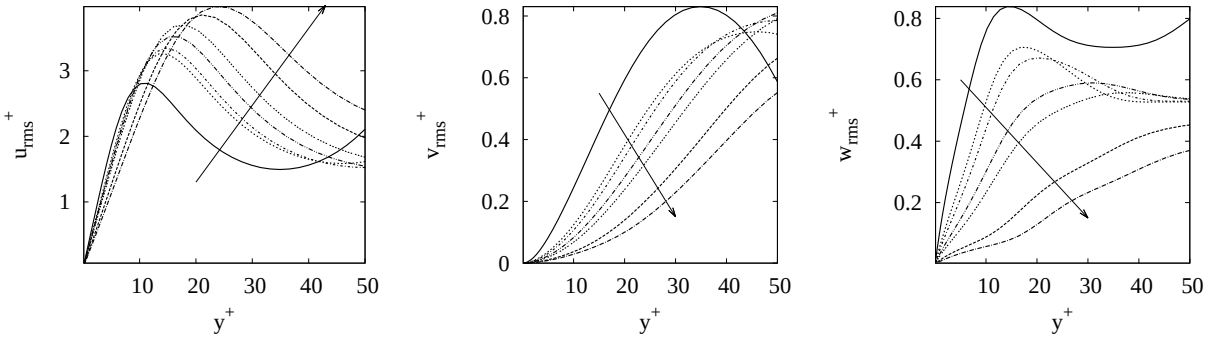

Figure 4.11: *rms* velocity profiles $u^+_{rms}(y^+)$, $v^+_{rms}(y^+)$ and $w^+_{rms}(y^+)$ for the set of data mentioned in table 4.2. The arrow indicates the increase in Reynolds number and simultaneous decrease in box size in outer units.

This strategy gives a very good initial guess for both the velocity field and box dimension at the selected Reynolds number, and the Newton-Krylov iterations converge in three to four iterations. Typical domain sizes considered during this 'near-wall cycle continuation' are reported in table 4.2 while the corresponding velocity profiles are reported in figure 4.11. From this figure it is apparent that the solutions continued in these near-wall minimal flow units do not converge to near-wall structures. For instance, the y^+ position of the maximum of the *rms* velocity profiles increases when Re_τ is increased, while they should instead remain constant as found by Jiménez & Moin (1991) in minimum flow unit simulations (see also Hwang, 2013). The Nagata-Clever-Busse-Waleffe solutions, therefore, do not seem to be connected to near-wall structures, at least in plane Couette flow, even if continued in periodic domains which remain constant in inner units while increasing the Reynolds number.

4.6 Discussion

In this chapter we have studied the dynamics of large-scale motions in a LSM-Box periodic domain with $L_x \times L_z = 10.9h \times 5.3h$ which is the 'optimum' domain considered by Waleffe (2003) and has the same dimensions as LSM motions. LSM survive the quenching of the near-wall cycle also in the LSM-Box. We have then looked for the edge state of coherent (overdamped) large-scale motions and have shown that:

- The edge state of LSM overdamped ($C_s = 0.14$) solutions of the LES is a steady solution (it is computed as nonlinear travelling wave and found to have zero phase speed).

- This lower branch solution can be connected by continuation in C_s to the Nagata-Clever-Busse-Waleffe branch of steady solutions of the Navier-Stokes equations.

- It is possible to reach the corresponding upper branch steady solutions at the reference LES parameter $C_s = 0.05$ by continuation in C_s, via a saddle-node bifurcation or by continuation of the Nagata-Clever-Busse-Waleffe upper branch solutions.

- Upper branch solutions at Reynolds numbers up to Re = 2150, corresponding to $\mathrm{Re}_\tau = 127$, well into the turbulent regime, can be computed using specific paths in the $\mathrm{Re} - C_s$ plane.

- The continuation of the Nagata-Clever-Busse-Waleffe upper branch solutions to high Reynolds numbers in minimal flow units with dimensions fixed in inner units to $L_x^+ \times L_z^+ \approx 250 \times 100$ does not result in structures with converging y^+-structure.

The Nagata-Clever-Busse-Waleffe upper branch solutions, originally computed at low to transitional ($\mathrm{Re} \approx 400$) Reynolds numbers,[2] seem therefore more related to the dynamics of large-scale motions and not to the near wall cycle in the fully developed turbulent regime.

The mean and *rms* velocity profiles of the coherent LSM steady solutions computed for the LES equations are similar to those of the Nagata-Clever-Busse-Waleffe solutions computed for the Navier-Stokes equations. One could be therefore tempted to interpret the LES solutions just as the well known Navier-Stokes solutions (re)computed at a lower Reynolds number corresponding to the increased viscosity due to the unresolved scales. However, such an interpretation would neglect the fact that the eddy viscosity of the unresolved motions is non-uniform in space (see figure 4.10) so that the effective Reynolds number $\mathrm{Re}_{eff} = U_w h/\nu_t(\mathbf{x})$ depends on space. Therefore, the resemblance of the Navier-Stokes and of the LES steady solution is not at all *a priori* obvious and further investigation with enhanced grids is needed to understand if this resemblance persists at higher Reynolds numbers.

[2]Slightly higher Reynolds numbers have been attained in successive studies. For instance Rincon *et al.* (2007*b*) have continued the Nagata-Clever-Busse-Waleffe upper branch up to Re = 600.

Chapter 5

Invariant structures at large scale in plane Poiseuille flow

Hwang & Cossu (2010*a*) had isolated self-sustained large-scale motions in a plane channel. However, finding invariant solutions in this specific flow has proved much more difficult than in plane Couette flow. In particular, straightforward edge tracking at $C_s = 0.3$ has not led to any simple solution, and has displayed a probably chaotic dynamics, similarly to what has been found in pipe flow by Schneider *et al.* (2007). We have therefore dedicated considerable effort to finding appropriate invariant solutions of the Navier-Stokes equations in this flow where travelling waves (TW) solutions have been previously found by a limited number of investigators (Ehrenstein & Koch, 1991; Itano & Toh, 2001; Waleffe, 2003; Zammert & Eckhardt, 2013) and few relative periodic orbit are currently known (Toh & Itano, 2003; Zammert & Eckhardt, 2013).

5.1 Relative periodic orbit in the Waleffe optimal domain

As a first step in our investigation we tried to (re)compute the TW Navier-Stokes solution ($C_s = 0$) found by Waleffe (2003) following our usual method: use bisection to access the lower branch solution and then use Newton-based pseudo-arclength continuation to access the whole lower and upper branch solutions. We consider the Waleffe (2003) optimum domain of extension $L_x \times L_z = 2\pi \times 2.416h$, for which the travelling wave solutions appear at the lowest Reynolds number, and Reynolds numbers ranging from Re = 3000 to 5000.

The search for the lower branch TW initially proved unsuccessful, probably because this solution, unlike in the Couette case, has multiple unstable modes and cannot therefore be accessed by a standard one-parameter bisection. We therefore enforced the mid-plane reflection symmetry $\{u, v, w\}(x, y, z) = \{u, -v, w\}(x, -y, z)$ and tried again the bisection using as initial condition the laminar Poiseuille solution perturbed by a pair of streamwise uniform counter-rotating vortices of amplitude A_1 and a sinuous perturbation of the spanwise velocity with amplitude A_2:

$$\mathbf{u}_0 = \{U_{lam}(y), 0, 0\} + A_1 \left\{0, \frac{\partial \psi_0}{\partial z}, -\frac{\partial \psi_0}{\partial y}\right\} + A_2 \{0, 0, w_{sin}\} \tag{5.1}$$

where

$$\psi_0(y, z) = \left(1 - y^2\right) \sin(\pi y) \sin\left(\frac{2\pi z}{L_z}\right); \quad w_{sin}(x, y) = \left(1 - y^2\right) \sin\left(\frac{2\pi x}{L_x}\right). \tag{5.2}$$

The stream-function $\psi_0(y, z)$ is associated to streamwise uniform vortices, while w_{sin} provides the (streamwise) sinuous perturbation. The initial velocity fields $\mathbf{u}_0$ are solenoidal, have the same volume flux as the laminar Poiseuille solution $U_{lam} = 1 - y^2$ and respect the enforced symmetry.

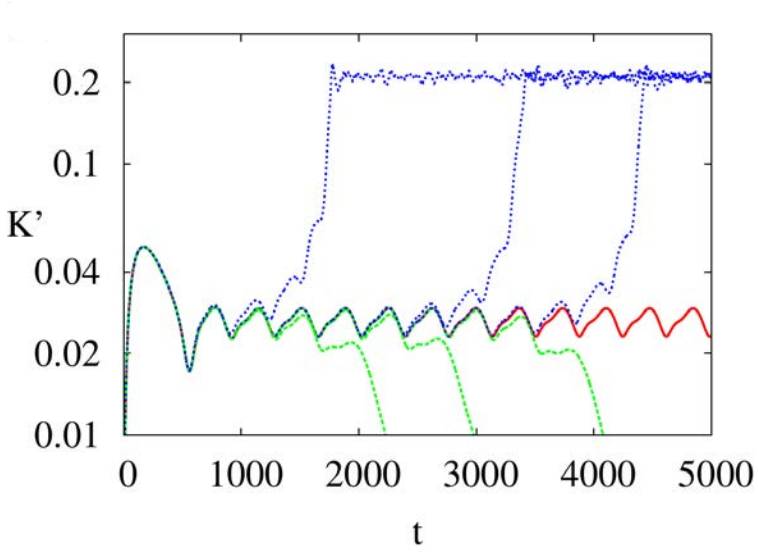

Figure 5.1: Temporal dependence of the total perturbation kinetic energy K' for selected iterations of the bisection process at Re = 3000. The solution on the edge rapidly converges to a periodic solution.

Re	$10^3\sigma_1$	$10^3\sigma_2$	$10^3\sigma_3$	$10^3\sigma_4$	$10^3\sigma_5$
3000	3.99	3.34	3.32	2.99	2.73
4000	3.39	1.34	1.16	1.06	1.03

Table 5.1: Real parts σ_j of the j-th Floquet exponents of the unstable modes of the RPO solutions.

The bisection was operated on A_1 with the ratio $A_2/A_1 = 1/10$ kept fixed to a relatively small value allowing the subcritical development of the streak instability (Cossu *et al.*, 2010, 2011). For this part of the study the Navier-Stokes equations were integrated using the `channelflow` code (Gibson *et al.*, 2008). Typically, results were obtained with $16 \times 41 \times 16$ points in the streamwise, wall-normal and spanwise directions and enforcing a constant volume flux during the simulation. We verified that the characteristics of the periodic solutions found by bisection on the coarse grid do not change when the number of collocation points is increased to $32 \times 65 \times 32$. The numerical results were further tested by recomputing the same periodic solutions with the different code `diablo` (Bewley, 2008). The convergence of the periodic solutions was validated and improved using Newton-based iterative methods and then their linear stability was analyzed using the in `channelflow` Viswanath (2007); Gibson *et al.* (2008) and Newton-Krylov `Peanuts` code, which can also perform the Floquet stability analysis of nonlinear solutions (see appendix B).

The relative periodic orbits. Unexpectedly, instead of finding the TW solution we were looking for, the edge tracking converged to a relative periodic orbit for all cases considered (see figure 5.1 for the Re = 3000 convergence) with a period which increases with Reynolds number ($T = 739$ for Re = 3000, $T = 1090$ for Re = 4000 and $T = 1418$ for Re = 5000). The periodic solutions were found to travel in the streamwise direction with a phase speed $C_x = 0.98$ for Re = 3000 and 0.985 for the two other cases. This indicates that the active part of the process is located near the channel centre. These periodic solutions are unstable. A Floquet linear stability analysis was performed at Re = 3000 and 4000, once the convergence of the periodic solution was improved to sufficient

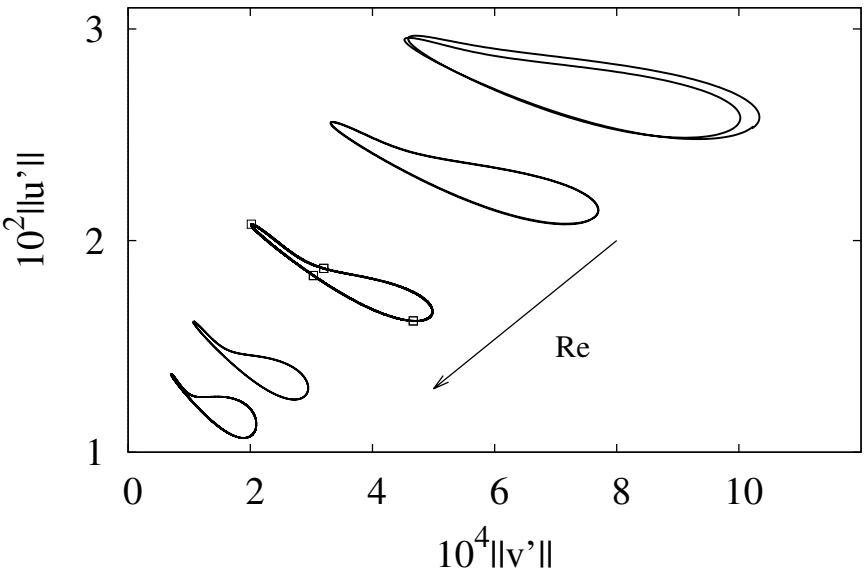

Figure 5.2: Converged periodic solutions represented in the $\|v'\|$-$\|u'\|$ plane for Re = 2000, 2500, 3000, 4000 and 5000 (top right to bottom left). The markers on the Re = 3000 cycle correspond to the snapshots reported in figure 5.3.

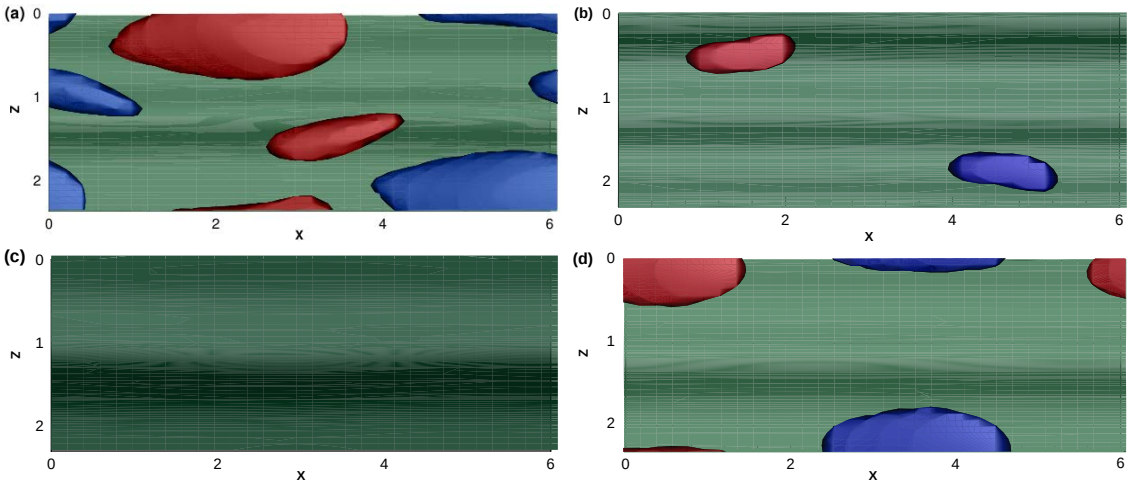

Figure 5.3: Snapshots of the converged periodic solution obtained at Re = 3000. Four snapshots are taken in correspondence to the points reported on the cycle in figure 5.2 starting from the bottom left point and then rotating counterclockwise. The snapshots are taken at respectively t = 0 (panel a), t = 120 (panel b), t = 230 (panel c) and t = 310 (panel d). Only the top half of the channel is considered. In green is the surface where the streamwise velocity is 75% of its maximum value in the whole channel. In colored blue and red are reported the surfaces where the streamwise vorticity is ±60% of its maximum value in panel (a) with the same value in all panels. In particular, no vortices are visible in panel (c) because they are of very low amplitude.

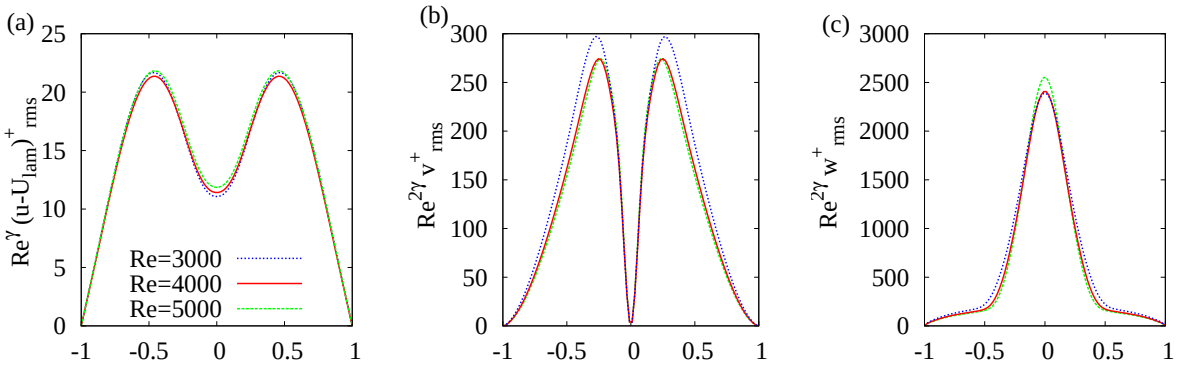

Figure 5.4: Rescaled *rms* amplitudes of the periodic velocity perturbations expressed in wall units and averaged over one period. The streamwise, wall-normal and spanwise components are reported in panels (a), (b) and (c), respectively. The solutions are rescaled using the value $\gamma = 0.8$.

accuracy using Newton iterations. If no symmetry is enforced, five unstable exponents are found, but only one of these modes (the most unstable) has the same symmetries as the periodic orbit solution. All the unstable Floquet exponents are real and their real part, reported in table 5.1, decreases for increasing Reynolds numbers.

The periodic self-sustained process. In figure 5.2 the converged periodic solutions are shown in the $\|v'\|$-$\|u'\|$ plane, where $\|u'\|^2 = (1/\mathcal{V}) \int_{\mathcal{V}} (u - U_{lam})^2 \, d\mathcal{V}$ and $\|v'\|^2 = (1/\mathcal{V}) \int_{\mathcal{V}} v^2 \, d\mathcal{V}$. The norm $\|u'\|$ of the streamwise perturbation velocity is representative of the amplitude of streamwise streaks, while $\|v'\|$ is representative of the amplitude of the quasi-streamwise vortices. The solutions rotate counter-clockwise in the cycles reported in figure 5.2. Starting from a point on the bottom-right of the cycle, where the amplitude of the vortices is maximum, the amplitude of the vortices initially decays while that of the streaks increases, due to the lift-up mechanism. The streaks then reach a maximum amplitude where they experience a breakdown during which their amplitude decays fast, while regenerating the vortices, which closes the loop of the classical self-sustained process (Hamilton *et al.*, 1995). The solution travels quite fast in the lower part of the cycle, as can be seen also in figure 5.1 where it is seen that the growth phase (lift-up) of $K' \approx \|u'\|^2$ is much slower than the decay phase (breakdown). The evolution of the flow structures during the cycle can be seen in the snapshots of the flow-field displayed in figure 5.3, taken in correspondence to the four points shown in figure 5.2. The converged periodic solutions have the shift and reflect symmetry $\{u, v, w\}(x, y, z) = \{u, v, -w\}(x + L_x/2, y, -z)$, which was not enforced on the initial condition. From the snapshots at $Re = 3000$ it is seen how every half-period the low speed streak and the quasi-streamwise vortices shift by half spanwise wavelength and then repeat the cycle exactly in the same way due to the shift and reflect symmetry of the solutions. One period therefore corresponds to two loops of the cycles reported in figure 5.2. This $T/2 - \lambda_z/2$ shift symmetry is preserved at higher Reynolds numbers but is lost at lower ones, as can be seen in figure 5.2.

Rms-velocity profiles and their Reynolds number scaling. From figure 5.2 we see that the amplitude of the relative periodic solutions decreases for increasing Reynolds numbers, which is typical of 'lower branch' solutions which live on the edge of chaos (see e.g. Kreilos *et al.* (2013) for the asymptotic suction boundary layer case). An examination of the root-mean-square velocity field perturbation, averaged over the horizontal planes and one temporal period, shows that most of the perturbation *rms* kinetic energy resides in the streamwise velocity component (streaks) with maximum amplitude located near $y \approx \pm 1/2$. The wall-normal and spanwise velocity *rms* profiles

are consistent with center-channel quasi-streamwise vortices. These periodic solutions, therefore, unlike previously found periodic-like solutions Toh & Itano (2003), are not localized near a single wall but in the bulk of the flow. When the Reynolds number is increased, the *rms* amplitude of the velocity field perturbation is seen to decrease. The velocity *rms* profiles remain approximately self-similar with amplitudes decreasing as $\mathrm{Re}^{-\gamma}$ for the streamwise velocity and $\mathrm{Re}^{-2\gamma}$ for the wall-normal and the spanwise velocity components, with $\gamma \approx 0.8$. The fact that the streaks amplitude is always larger than the vortex amplitude and that the ratio of streak to vortex amplitudes is almost proportional to the Reynolds number are additional indications that the non-normal amplification of streaks from the vortices plays an important role in the self-sustainment of these periodic solutions.

Another important point is that the self-similarity implies that the streaky structures associated with the relative periodic orbits do not migrate to the near wall region as the Reynolds number is increased. These structures which remain situated in the bulk of the flow for increasing Reynolds numbers and which are associated to quite low frequencies of oscillation are therefore compatible with large-scale motions.

5.2 Continuation in the spanwise box dimension L_z

We have been unable to continue the RPO solutions solutions discussed in §5.1 much below $Re = 2000$ and we have been therefore unable to find the 'low-Re origin' of these solutions . Similar attempts to continue the solutions to C_s values larger than 0.02 have also failed. In plane Couette flow, Kawahara & Kida (2001) obtained the 'gentle' periodic orbit by starting with Nagata (1990) solution and by then decreasing their domain size. We have therefore continued the solution by *increasing* the spanwise box size L_z in order to find if a TW solution could be reached in this way. Using a similar approach in the asymptotic suction boundary, Kreilos *et al.* (2013) found that the relative periodic orbit was transformed into a travelling wave via a saddle-node infinite period bifurcation (see e.g. Strogatz, 2001) often abbreviated into 'SNIPER bifurcation' (see e.g. Kreilos *et al.*, 2013).

5.2.1 The birth of a TW via an infinite-period global bifurcation.

We expect the time period to grow to very large values if a global bifurcation of the RPO is approached. To keep the computations manageable we therefore performed the L_z continuation at $Re = 2000$, where the period T is much smaller than for higher Reynolds numbers. The streamwise box dimension $L_x = 2\pi$ is kept constant. The RPO solution was computed in the usual way by edge tracking in the symmetric subspace for decreasing value of L_z. At $L_z \approx 3.6249$, instead of the RPO, the edge tracking converge to a travelling wave (TW) lying in the same symmetric subspace as the periodic orbits. In order to track the solution more accurately, we have continued the TW solution in L_z using pseudo-arclength continuation. The continuation reveals a saddle node bifurcation at $L_z^{SNIPER} = 3.55$, as shown in figure 5.5.

When approaching the global bifurcation the RPO temporal period T strongly increases, as shown in figure 5.6. From this is also seen that the increase of T is related to longer and longer quiescent phases.

Kreilos *et al.* (2013) found very similar bursting orbits in the asymptotic suction boundary layer (ASBL). They used an homotopy starting from plane Couette in the suction velocity parameter to reach the ASBL. When their travelling wave is continued in suction velocity, a lower branch is generated via a saddle node bifurcation, and slightly below the critical value of suction velocity they encountered bursting orbits with very large period. They showed that the edge state in Couette flow is connected by a heteroclinic connection to the $L_z/2$ spanwise shifted copy of itself, and these two are separated by a saddle in the same symmetric subspace. Therefore, there are

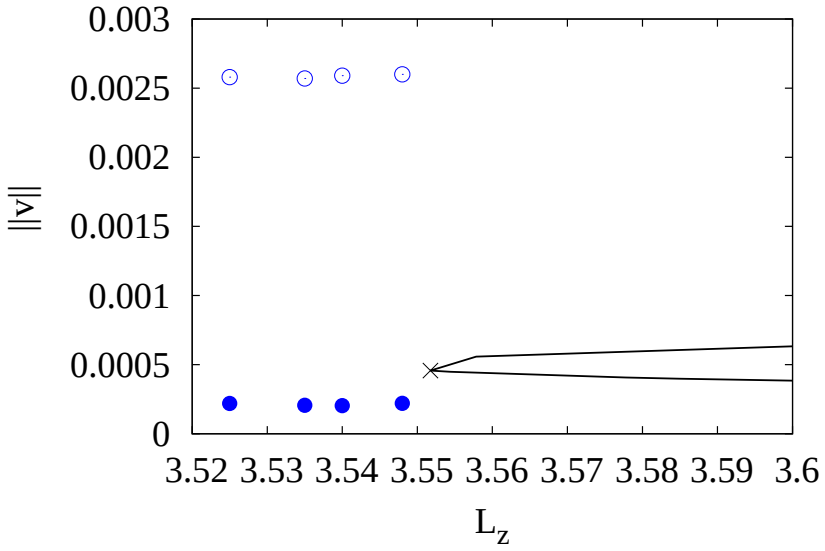

Figure 5.5: Bifurcation diagram in L_z, with $L_x = 2\pi$ and Re = 2000 where the RPO solution disappears in a global SNIPER bifurcation originating a pair of travelling waves. The RPO solutions is denoted by its maximum (empty symbols) and minimum (filled symbols) values of the spatially-averaged wall-normal velocity. The point where the upper and lower branch TW solutions are generated is denoted by the X symbol.

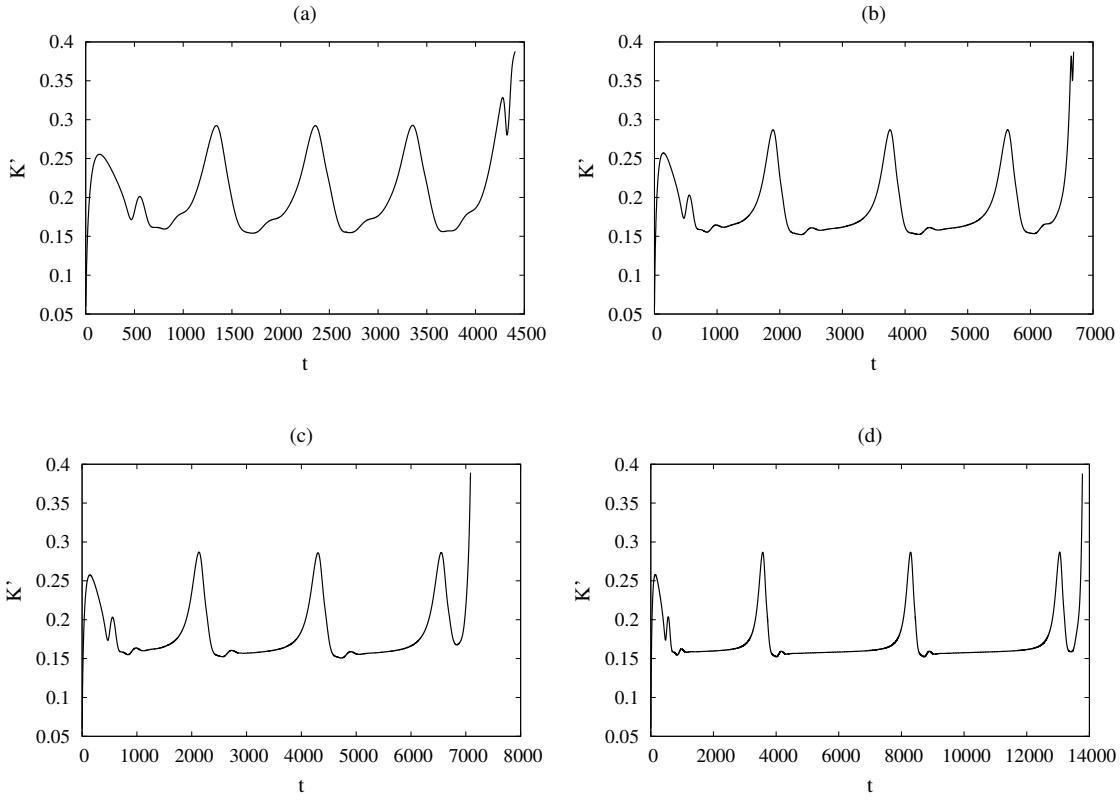

Figure 5.6: Pertubation energy of the RPO solutions from the edge-tracking procedure for the selected increasing (a to d panel) values of L_z corresponding to the symbols in figure 5.5. Remark the increasing maximum time displayed in the plots.

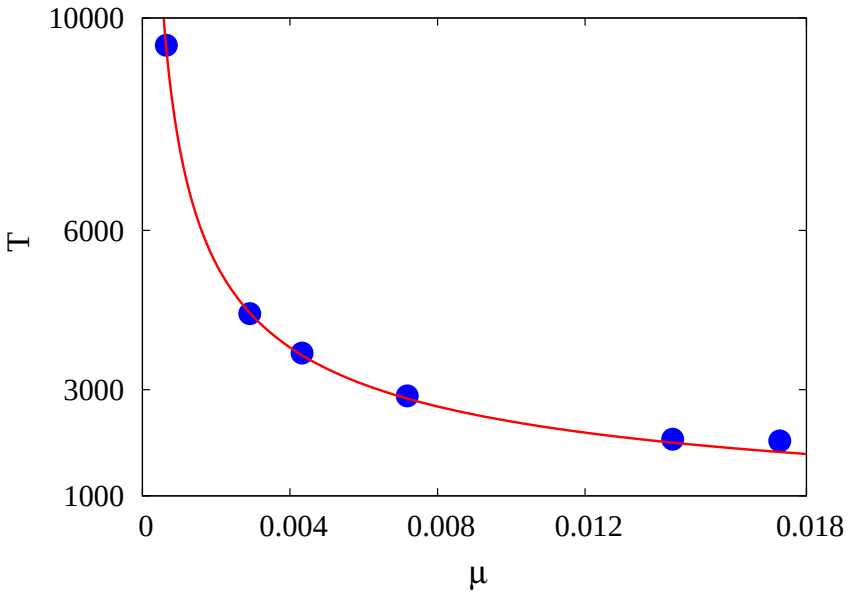

Figure 5.7: The variation of time period T close to the bifurcation point. The analytical fit (solid line) of a SNIPER bifurcation, $T \approx 240/\sqrt{\mu}$ agrees well with the computed data here. The four leftmost symbols correspond to the signals reported in figure 5.6.

four fixed points: two stable (upper branch, heteroclinically connected) and two unstable (lower branch, heteroclinically connected) which annihilate in a saddle-node infinite-period bifurcation (SNIPER), when suction velocity is increased. Tuckerman & Barkley (1988) performed the simulation of full time-dependent Boussinesq equation for a cylinder in search of travelling waves. They varied the Rayleigh number (R) and found that the periodic orbit encountered a bottleneck at a critical value R_c, where their period shoots to very high values, beyond R_c, finite amplitude travelling waves are produced via a global bifurcation (SNIPER).

To confirm that the bifurcation found is a SNIPER, we plot the time period T of the periodic solutions against the parameter $\mu = (L_z - L_z^{SNIPER})/L_z^{SNIPER})$ in figure 5.7. The hallmark of the SNIPER bifurcation is that the amplitude of the cycle essentialy stays *O(1)* while the time period diverges as $\mu^{-1/2}$ as the bifurcation point is approached point (see e.g. Strogatz, 2001). From figure 5.7 it is indeed seen that the period varies as $240/\sqrt{\mu}$ close to the bifurcation point while the RPO amplitude essentially remains constant, as shown in figure 5.5. We therefore confirm that the global bifurcation scenario observed here is saddle-node infinite-period (SNIPER) bifurcation.

5.2.2 Structure of the NTW

While the upper branch can be continued up to $L_z \approx 5.57$ (two other turning points are encountered at $L_z = 4.82$ and $L_z = 4.788$), it has been possible to continue the lower branch up to a much larger value of L_z ($L_z \approx 26$ as shown in figure 5.8).

Upper branch solution: towards turbulent LSM solutions The flow structures of the TW at the bifurcation ($L_z \approx L_z^{SNIPER}$), reported in panel *a* of figure 5.9, consists of the usual low speed streak flanked by positive and negative quasi-streamwise vortices. When these structures are continued along the upper branch to larger L_z, the number of structures is seen to increase. Roughly, three structures are present from just above the SNIPER point up to the maximum attained L_z. Indeed, at $L_z = 5.55$ the upper branch solution, reported in figure 5.9(b), contains three low speed streaks and three pair of quasi-streamwise vortices which correspond to a streak spacing $\lambda_z \approx 1.8$ which

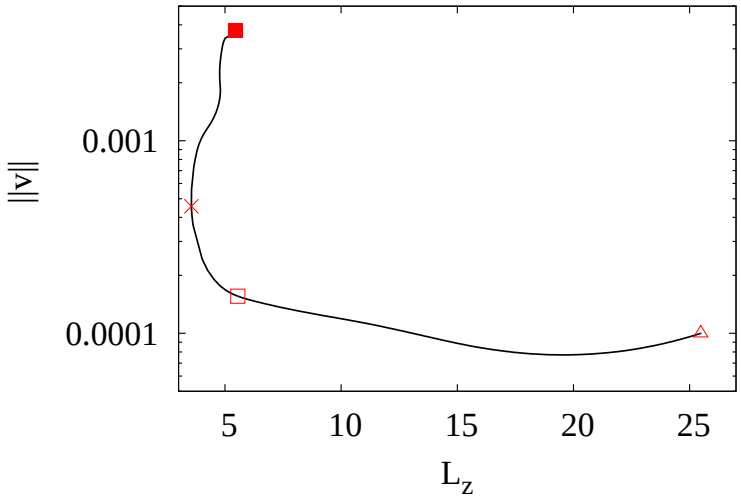

Figure 5.8: TW bifurcation diagram in L_z, with $L_x = 2\pi$ and Re = 2000. A part of this diagram is already reported in the right part of figure 5.5. The saddle node where the upper and lower TW branches originate is a SNIPER global bifurcation.

is in good agreement with the size of large-scale motions (LSM) in the turbulent channel (del Álamo & Jiménez, 2003; del Álamo *et al.*, 2004; Hwang & Cossu, 2010*c*). This spacing is confirmed by the analysis of the spanwise premultiplied spectrum of the streamwise velocity reported in figure 5.10. As seen from figure 5.11 the energy of the upper branch solutions increases for increasing L_z. However the *rms* profiles preserve a similar shape, which is also similar to that of the RPO solutions existing before the SNIPER bifurcation.

We have also continued the UB solutions from $C_s = 0$ to $C_s = 0.05$ using the same grid. This corresponds to the introduction of dissipative small scales. Proceeding along these lines makes sense because Re = 2000 is more than twice the value of the Reynolds number at which transition is usually observed. As shown in figure 5.12, the introduction of small scale dissipation does not significantly alter the solutions, except for a slight reduction of the maximum *rms* streamwise velocity.

Lower branch solution: spanwise localized structures When the TW issued from the SNIPER bifurcation is continued to larger L_z along the lower branch the number of structures (one at the bifurcation) remains fixed, unlike what is observed along the upper branch. When L_z is increased, the lower branch solution unique structure remains localized in the spanwise direction, leaving a large portion of the domain almost unperturbed as can be seen in figure 5.9*c*. This solution has been continued up to $L_z = 25.5$ without displaying any qualitative change during the continuation. The localized structures here arise 'naturally' through continuation without the need of the windowing function used e.g. by Gibson & Brand (2014).

The localized solutions of the lower branch are unstable (the unique unstable eigenvalue found is 1.7×10^{-3}). When the localized TW lower branch solution is perturbed along its unstable eigendirection, the dynamics becomes turbulent, while it becomes laminar when perturbed in the opposite direction as shown in figure 5.13. This indicates that the lower branch localized state (red cross in the figure 5.8) sits on the edge of chaos.

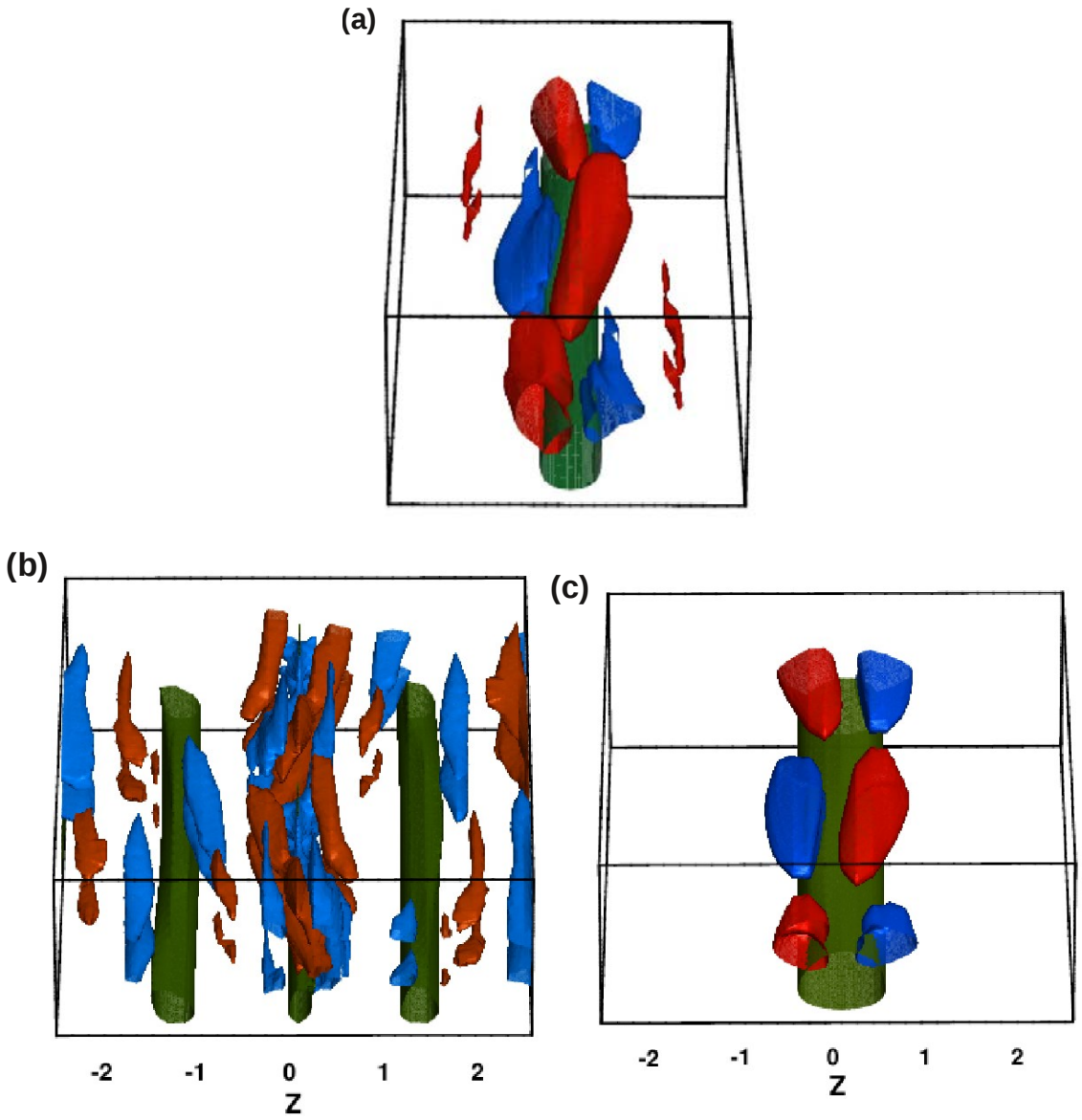

Figure 5.9: TW structures corresponding to: (a) saddle node $L_z \approx 3.55$ (X symbol in figure 5.8). (b) and (c) are, respectively, the upper (filled square symbol in figure 5.8) and lower branch (empty square symbol in figure 5.8) solutions computed at $L_z = 5.55$. The iso-surfaces at $u^+ = -2$ are plotted in green, while red and blue surfaces correspond to positive and negative streamwise vorticity at $\omega_x = \pm 0.5 max(\omega_x)$

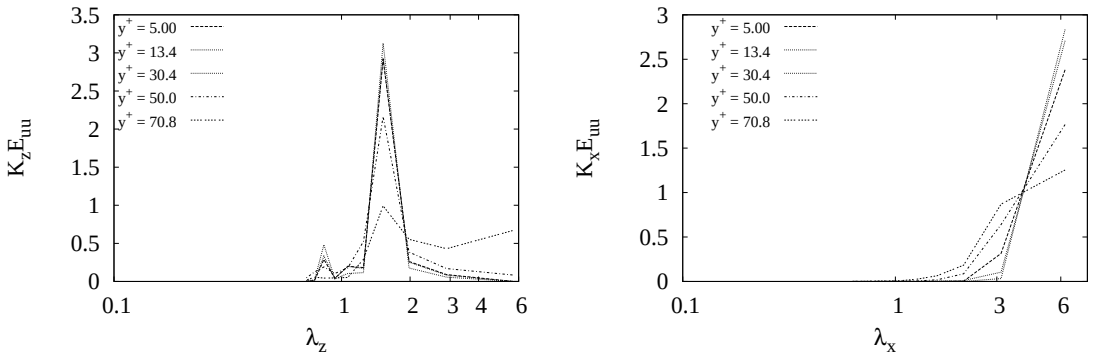

Figure 5.10: One-dimensional spanwise (left) and streamwise (right) premultiplied spectra of the streamwise velocity at $Re = 2000$ for the upper branch TW computed at $L_z = 5.55$ and displayed in figure 5.9(b).

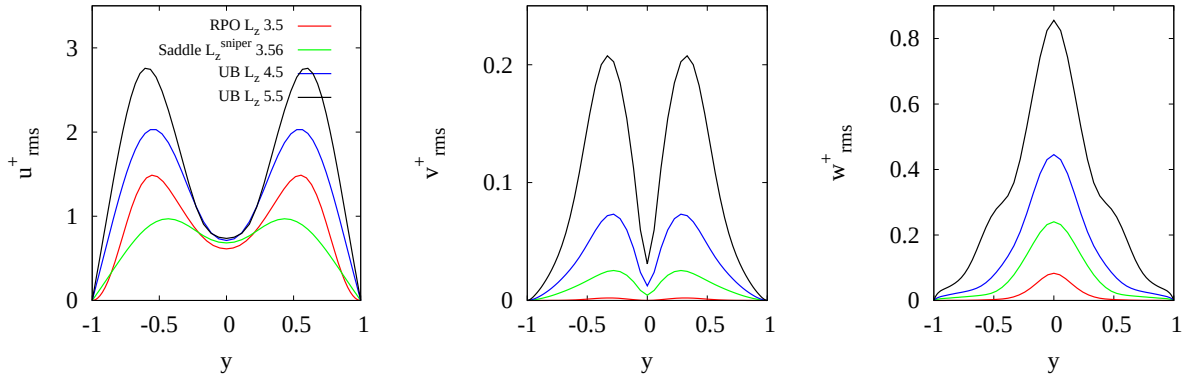

Figure 5.11: Comparison of the *rms* velocity profiles of the TW upper branch solutions for selected values of L_z to the profiles of the RPO before the SNIPER bifurcation.

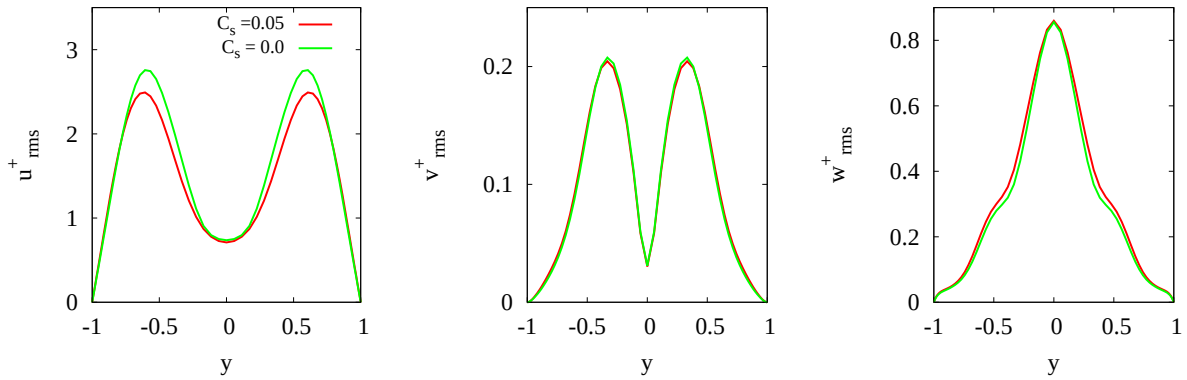

Figure 5.12: Comparison of the *rms* velocity profiles of the TW upper branch solutions for $C_s = 0$ and $C_s = 0.05$ (with $L_z = 5.55$ and Re = 2000).

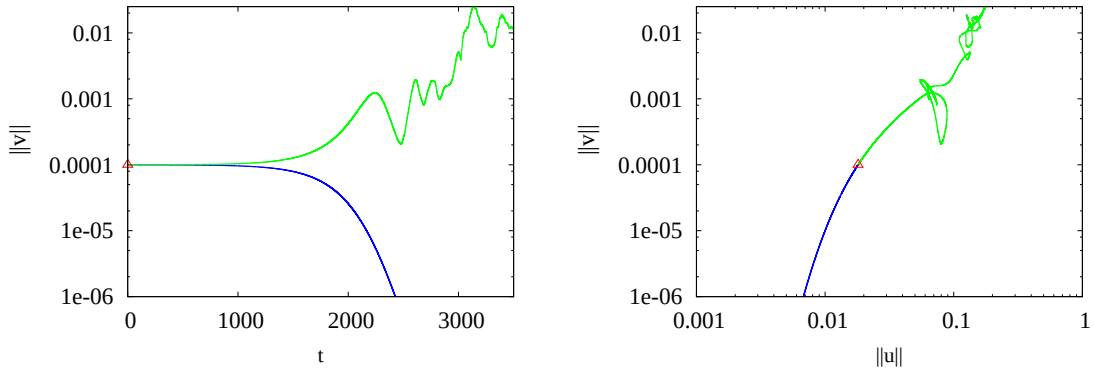

Figure 5.13: Trajectories initialized along the unstable eigendirection of the lower branch spanwise localized travelling wave ($L_x = 2\pi$, $L_z = 25$, Re = 2000) and represented in the $t - \|u'\|$ (left panel) and $\|u'\| - \|v'\|$ (right panel) planes respectively. When initialized along one direction of the unstable manifold the flow rapidly relaxes to the laminar Poiseuille solution (blue line). When initialized in the opposite direction, a turbulent state is attained (green line). This indicates that the lower branch localized state (red cross in the figure) sits on the edge of chaos.

5.3 Discussion

In this chapter we have discussed all the results obtained in plane Poiseuille flow. They can be summarized as follows:

- A (lower) branch of relative periodic orbits solutions of the Navier-Stokes equation ($C_s = 0$) has been found in plane Poiseuille flow at relatively large Reynolds numbers. It has not been possible to continue these solutions much below Re ≈ 2000.
- We show that the RPO solutions found are connected to travelling wave (TW) solutions via a global bifurcation (a saddle-node-infinite period bifurcation) when they are continued by increasing the spanwise size L_z of the numerical domain.
- The lower branch TW solution branch evolves into a spanwise localized state when L_z is further increased.
- The upper branch TW solutions develop multiple streaks with spanwise spacing consistent with large-scale motions in the turbulent regime.
- These upper branch solutions do not change much when they are continued to $C_s = 0.05$ at Re = 2000 where they represent turbulent coherent large-scale motions.

The dynamics of the RPO we have found (see also Rawat *et al.*, 2013, 2014) bears some resemblance to that of RPO solutions in the asymptotic boundary layer reported by Kreilos *et al.* (2013) for instance in their $T/2 - L_z/2$ shift property and with their bursting behaviour. This could indicate that this family of solutions is generic.

The saddle-node infinite period bifurcation found by increasing L_z is also of the same type of the bifurcation found by Kreilos *et al.* (2013) by homotopy between the Couette flow and the asymptotic suction boundary layer. This type of bifurcation has, however, already been detected in previous investigations of invariant solutions in fluid systems (see e.g. Tuckerman & Barkley, 1988).

The spanwise localization of the lower branch solution is also in accordance with the results of recent investigations that revealed the spanwise localization of other lower branch solutions (Schneider *et al.*, 2008; Duguet *et al.*, 2009, 2012; Khapko *et al.*, 2013; Gibson & Brand, 2014).

The most important result here probably pertains to the structure of the TW upper branch solution which is seen to develop multiple streaks in the spanwise direction and to preserve its structure in the presence of small scale dissipation. The wall-normal structure of the upper branch, just as the one of the found RPO, is reminiscent of large-scale motions in the outer region, and probably of the 'inactive' motions defined by Townsend (1976). Further investigations are therefore needed to determine if other TW or RPO solutions can be continued to the fully turbulent regime.

Chapter 6

Conclusions

It is useful to summarize here the main motivations and the main results of this thesis.

Summary of the motivations of this study. The main goal of this thesis was to compute invariant solutions corresponding to large-scale motions and understand their relevance to a variety of fully developed turbulent shear flows. The approach taken is the one of Hwang & Cossu (2010*c*, 2011) who have used a, possibly overdamped, static Smagorinsky model in large eddy simulations in order to filter out small scale motions and therefore be able to investigate self-sustained processes at large scales. The main results of the study are summarized below.

A self-sustained process at large scale in turbulent Couette flow (chapter 3). As a first step of the investigation, we have applied the approach of Hwang & Cossu (2010*c*) to turbulent Couette flow in very long and wide domains ($L_x \times L_z = 130h \times 12.5h$) at Reynolds numbers ranging from Re = 750 to Re = 2150. We find that large eddy simulations in very large and wide boxes at moderate Reynolds numbers are able to capture the most important features of turbulent Couette flow, namely the near-wall cycle and the large and very large-scale motions (LSM & VLSM). When the near-wall cycle is artificially quenched, the large-scale motions (LSM) do survive, exactly as found by Hwang & Cossu (2010*c*) in the turbulent channel. This further confirms that a self-sustained mechanism must be at work also at large scale and that it is probably based on the coherent lift-up effect predicted by del Álamo & Jiménez (2006); Pujals *et al.* (2009); Cossu *et al.* (2009); Hwang & Cossu (2010*a*,*b*); Willis *et al.* (2010) and observed by Pujals *et al.* (2010*b*). In what concerns the very large-scale motions (VLSM), we find that their characteristic peak is suppressed when motions at smaller scales are artificially quenched. This could imply either that their characteristic scale moves to longer wavelengths in overdamped simulations or that those motions are forced by motions at smaller scale. Additional investigations in longer numerical domains are needed to clarify this issue.

Coherent large-scale steady solutions in turbulent Couette flow (chapter 4). The second part of the investigation has dealt with the nature of the dynamics of large-scale motions (LSM) in turbulent Couette flow in a periodic domain of dimensions $L_x \times L_z = 10.9h \times 5.3h$. This domain is the 'optimum' domain considered by Waleffe (2003) and has the same dimensions as LSM motions which are characterised by $\lambda_x \approx 10 \sim 12h$ and $\lambda_z = 4.5 \sim 5.5h$. The considered Reynolds numbers here range from Re = 127 (saddle node bifurcation of the Nagata-Clever-Busse-Waleffe solutions) to Re = 2150, which is well into the turbulent regime. After showing that, also in the LSM-Box, LSM also survive the quenching of the near-wall cycle, we have looked for the edge state of coherent (overdamped) large-scale motions and have shown that the edge state found in overdamped ($C_s = 0.14$) simulations is a non-trivial steady solution (it is found as a travelling with

zero phase speed). Most importantly we have also shown that this lower branch solution can be connected, by continuation in C_s, to the Nagata-Clever-Busse-Waleffe branch of TW solutions of the Navier-Stokes equations and that it is possible to reach the corresponding upper branch TW solutions at the reference LES parameter $C_s = 0.05$ through a saddle node bifurcation at large C_s or a saddle-node bifurcation at low Reynolds number. We have been able to compute 'turbulent' ($C_s = 0.05$) upper branch solutions at Reynolds numbers up to $\mathrm{Re} = 2150$ using specific paths in the $\mathrm{Re} - C_s$ plane. Finally, the continuation of the Nagata-Clever-Busse-Waleffe upper branch solutions to high Reynolds numbers in minimal flow units with dimensions fixed in inner units to $L_x^+ \times L_z^+ \approx 250 \times 100$ does not result in structures consistent with near wall structures issued from DNS in minimal flow units. The Nagata-Clever-Busse-Waleffe solutions seem therefore more related to the dynamics of large-scale motions and not to the near wall cycle in the fully developed turbulent regime. The coherent steady solutions computed for the LES equations are similar to the Nagata-Clever-Busse-Waleffe solutions computed for the Navier-Stokes equations but, contrary to the latter, they take into full account the fact the eddy viscosity of the unresolved motions is non-uniform in space (see figure 4.10) and is dependent on the solution itself. Further investigation with enhanced grids is needed to understand if the resemblance of Navier-Stokes and the LES steady solutions persists at higher Reynolds numbers and for other types of solutions.

Large scale symmetric RPO in plane Poiseuille flow (chapter 5). The first part of the study of plane Poiseuille flow has concerned relative periodic orbit (RPO) solutions of the Navier-Stokes equations. A (lower) branch of relative periodic orbits solutions of the Navier-Stokes equation ($C_s = 0$) has been found in plane Poiseuille flow at relatively large Reynolds numbers (up to $\mathrm{Re} = 5000$). It has not been possible to continue these solutions much below $\mathrm{Re} \approx 2000$ or to $C_s = 0.05$. The dynamics of these RPO is similar to that of RPO solutions in the asymptotic boundary layer reported by Kreilos *et al.* (2013) with respect to their $T/2 - L_z/2$ shift property and with their bursting behaviour. This could indicate that this family of solutions is generic. We have also shown that the RPO solutions are connected to travelling wave (TW) solutions via a global bifurcation (a saddle-node infinite period bifurcation) when they are continued by increasing the spanwise size L_z of the numerical domain. The infinite period saddle-node bifurcation found by increasing L_z is also of the same type of the bifurcation found by Kreilos *et al.* (2013) by homotopy between the Couette flow and the asymptotic suction boundary layer. This type of bifurcation has also been detected in previous investigations of invariant solutions in other fluid systems (Tuckerman & Barkley, 1988).

Large scale non-symmetric TW solutions in plane Poiseuille flow (chapter 5). We have then investigated the TW solutions issued from the saddle-node infinite period bifurcation. The lower TW solution branch evolves into a spanwise localized state when L_z in further increased, similarly to several recent studies on other wall-bounded shear flows (Schneider *et al.*, 2008; Duguet *et al.*, 2009, 2012; Khapko *et al.*, 2013; Gibson & Brand, 2014) in which spanwise localization of lower branch solutions has also been reported. The upper branch TW solutions develop multiple streaks which have a spanwise spacing consistent with the one of large-scale motions in the turbulent regime. These upper branch solutions do not change much when they are continued to $C_s = 0.05$ at $\mathrm{Re} = 2000$ where they represent turbulent coherent large-scale motions. The wall-normal structure of the upper branch, just as the one of the found RPO, is reminiscent of large-scale motions in the outer region, and probably of the 'inactive' motions defined by Townsend (1976). Further investigations are therefore needed to find if other TW or RPO solutions can be continued to the fully turbulent regime.

General conclusions and open questions. This study is a second step, after that of Hwang & Cossu (2010*c*, 2011), towards a 'dynamical systems' understanding of the large-scale dynamics in fully developed turbulent shear flows. The key ingredient is to model small-scale motions and to only resolve large-scale motions in order to compute invariant TW or RPO solutions. Artificial over-damping has been used to quench an increasing range of small-scale motions and prove that the motions at large scale are self-sustained. It has also been used as a continuation parameter useful to reach upper branch solutions. This approach would not have been possible if, as conjectured in some previous investigations, large-scale motions in wall bounded shear flows are forced by mechanisms based on the existence of active structures at smaller scale. Our results indicate that Nagata-Clever-Busse-Waleffe upper branch solutions, computed for the Navier-Stokes equations can be continued to higher Reynolds numbers (at least up to Re = 2150 in plane Couette flow) which are well in the turbulent regime. Less trivial upper branch solutions, computed in plane Poiseuille flow, have also been continued in a similar way without any major difficulty. However, at the time of writing of this manuscript, we have not yet been able to continue RPO solutions from Navier-Stokes solutions to filtered motions in reference LES. An important open question is therefore to know which other NTW or RPO Navier-Stokes solutions can be continued in a similar way.

The interest of the invariant solutions obtained in the LES equations is that, contrary to the Navier-Stokes solutions, they take into full account the spatial and Reynolds number dependence of the eddy viscosity associated with unresolved small scale motions.

An interesting question, which is left for future work, is to know how much time is spent in the neighbourhood of these solutions by the large-scale 'filtered' motions solutions of LES simulations. One could indeed hope that the increase in effective viscosity, i.e. the decrease of the effective Reynolds number in fully developed turbulent large-scale flows, could bring back the effective large-scale dynamics close to the transitional case where a few invariant solutions are probably sufficient to capture essential features of the flow (see e.g. Kawahara & Kida, 2001).

Another important result is that very large-scale motions (VLSM), contrary to large-scale motions (LSM), do not survive a moderate over-damping. This would suggest that these motions are not self-sustained and are not an aggregate of large-scale motions. The mechanism by which they sustain must therefore involve also motions at much smaller scale. Future work could focus on the identification of the precise mechanism by which VLSM sustain.

Finally, the method used in this thesis could help to shed light on the very large Reynolds and magnetic Reynolds number behaviour of a magneto-hydrodynamic self-sustained process active in Keplerian shear flows (Rincon *et al.*, 2007*b*,*a*, 2008; Herault *et al.*, 2011; Riols *et al.*, 2013), with possible practical implications for the understanding of the physics of astrophysical accretion disks (Riols *et al.*, 2014).

Appendix A

Computing invariant solutions

A.1 Newton based iterative methods

The search for invariant solutions of Navier-Stokes equation such as travelling waves or a relative periodic orbits, require us to solve nonlinear equations of the form $\mathbf{F}(\mathbf{\Phi}) = \mathbf{0}$.

Newton iterations. A Taylor series expansion of $\mathbf{F}(\mathbf{\Phi})$ around the current solution $\mathbf{\Phi^i}$ gives

$$\mathbf{F}(\mathbf{\Phi^i} + \delta\mathbf{\Phi^i}) = \mathbf{F}(\mathbf{\Phi^i}) + \nabla\mathbf{F}(\mathbf{\Phi^i}) \cdot \delta\mathbf{\Phi^i} + \text{H.O.T.} \tag{A.1}$$

if the left hand side is set to zero and higher-order terms are neglected we get

$$\mathbf{J}(\mathbf{\Phi^i}) \cdot \delta\mathbf{\Phi^i} = -\mathbf{F}(\mathbf{\Phi^i}) \quad ; \quad \mathbf{\Phi^{i+1}} = \mathbf{\Phi^i} + \delta\mathbf{\Phi^i}, \tag{A.2}$$

where $\mathbf{J} = \nabla\mathbf{F}$ is the Jacobian matrix, $\mathbf{\Phi^i}$ is the state vector and $\delta\mathbf{\Phi^i}$ is the correction done at current Newton step. Iterations are stopped when:

$$\frac{\|\mathbf{F}(\mathbf{\Phi^i})\|}{\|\mathbf{\Phi^i}\|} \leq r_{tol}. \tag{A.3}$$

Krylov-subspace methods: Solving the linear system in A.2 can be prohibitively memory and time consuming for the typical 3D states we consider in this thesis. Even simply forming the Jacobian $\mathbf{J}$ explicitly, e.g. using finite difference, can be a challenge in itself. To solve this problem a widely used approach is to recur to subspace reduction methods relying only on calls to a matrix-vector multiplication, where the matrix is the one at hand (in our case the Jacobian operator). Krylov-subspace is obtained by sequence of matrix-vector multiplication

$$\mathbf{K}_j = \text{span}(\mathbf{r}_i, \mathbf{J}\mathbf{r}_i, \mathbf{J}^2\mathbf{r}_i, ...\mathbf{J}^{j-1}\mathbf{r}_i), \tag{A.4}$$

where $\mathbf{r}_i = -\mathbf{F}(\mathbf{\Phi^i}) - \mathbf{J}\delta\mathbf{\Phi^i}$ is the residual at i_{th} Newton iteration. The *Generalized minimum residual method* (**GMRES**) is a Krylov subspace method which composes $\delta\mathbf{\Phi}$ from the subspace spanned by Krylov vectors, such that it minimizes the residual $\|\mathbf{F}(\mathbf{\Phi}) + \mathbf{J}\delta\mathbf{\Phi}\|$ in a least-square sense. At every j_{th} **GMRES** iteration new update can be approximated as

$$\delta\mathbf{\Phi_j} = \sum_{k=0}^{j-1} c_k(\mathbf{J})^k\mathbf{r}_i. \tag{A.5}$$

From A.5 it is clear that to compute new update all we need is the matrix-vector multiplication $(\mathbf{J})^k\mathbf{r}_i$, which can be computed using a finite difference approximation

$$\mathbf{J}\phi \approx \frac{\mathbf{F}(\mathbf{\Phi} + \mathbf{h}\phi) - \mathbf{F}(\mathbf{\Phi})}{\mathbf{h}}, \tag{A.6}$$

where h is a small pertubation parameter. The error in the Jacobian-vector multiplication is proportional to h. If h is too big $\mathbf{J}\phi$ is poorly approximated and if too small the finite difference is not reliable due to floating-point roundoff error. In the present study we have determined the optimal range of values for h using trial and error. It is found to be in the range of $1e-4$ to $1e-8$. The convergence criterion for the Krylov iteration is set by the relative decrease in the residual norm. Suppose $\mathbf{r}_0$ is the residual vector at the starting of the Newton step and $\mathbf{r}_j$ is the residual vector after j_{th} **GMRES** iteration then if

$$\frac{||\mathbf{r}_j||}{||\mathbf{r}_0||} \leq g_r. \tag{A.7}$$

Line search algorithm: The main idea behind the Newton-Krylov subspace method is to decrease the residual norm $||\mathbf{F}(\mathbf{\Phi})||$ to a sufficiently low value. Sometimes, taking the full Newton update $\delta\mathbf{\Phi}$ need not decrease the residual norm and we may go out of the ball of convergence of Newton method. The direction of decrease of the residual is in the Newton direction $\delta\mathbf{\Phi}$, so we can move in that direction in small substeps

$$\mathbf{\Phi^{i+1}} = \mathbf{\Phi^i} + \alpha\delta\mathbf{\Phi^i}. \tag{A.8}$$

The aim of the line search algorithm is to find α in the range $[0, 1]$ such that the new residual $||\mathbf{F}(\mathbf{\Phi^i} + \alpha\delta\mathbf{\Phi^i})|| < ||\mathbf{F}(\mathbf{\Phi^i})||$. We define a function

$$\psi(\alpha) = ||\mathbf{F}(\mathbf{\Phi^i} + \alpha\delta\mathbf{\Phi^i})|| \quad ; \quad \psi'(\alpha) = \nabla\mathbf{F} \cdot \delta\mathbf{\Phi}. \tag{A.9}$$

The core of every line search techniques is to approximate $\psi(\alpha)$ with a polynomial and minimize it with respect to α in the Newton direction. To start the minimization procedure we require an initial guess α_0 which in our case is 0.01. At the first step we construct a quadratic polynomial with $\psi(0)$, $\psi(\alpha_0)$ and $\psi'(0)$ available to us.

$$\psi(\alpha) = \left(\frac{\psi(\alpha_0) - \psi(0) - \alpha\psi'(0)}{\alpha_0^2}\right)\alpha^2 + \psi'(0)\alpha + \psi(0). \tag{A.10}$$

The new trial value α_1 is the minimizer of this quadratic polynomial. In the subsequent steps a cubic polynomial is constructed based on the information from the quadratic step

$$\psi(\alpha) = a\alpha^3 + b\alpha^2 + \psi'(0)\alpha + \psi(0). \tag{A.11}$$

The value of a and b can be calculated by equating A.11 to $\psi(\alpha_0)$ and $\psi(\alpha_1)$. Minimization of this cubic polynomial provides the new trial value α_2. This process is repeated until $||\mathbf{F}(\mathbf{\Phi^i} + \alpha\delta\mathbf{\Phi^i})|| < ||\mathbf{F}(\mathbf{\Phi^i})||$.

A.2 Parameter Continuation

Solutions of Navier-Stokes equation are function of various parameters like Reynolds number, size of the domain, forcing etc. Sometimes, we are interested in the effect of the variation of these parameters on the solutions of N-S equation, on such occasions we need to express $\mathbf{\Phi}$ as a function of parameter λ. For such problems general form of nonlinear function can be written as

$$\mathbf{F}(\mathbf{\Phi}, \lambda) = \mathbf{0}. \tag{A.12}$$

The basic tool behind most of the continuation techniques is the implicit function theorem, which states that if A.12 is satisfied and the Jacobian $\mathbf{J}(\mathbf{\Phi}, \lambda)$ is non singular, then $\mathbf{\Phi}$ can be solved in terms

of λ and $d\mathbf{\Phi}/\mathbf{d}\lambda$ can be found differentiating implicitly. In the case of numerical continuation, A.1 is restated as

$$\mathbf{J}(\mathbf{\Phi^i}, \lambda) \cdot \delta\mathbf{\Phi^i} = -\mathbf{F}(\mathbf{\Phi^i}, \lambda) \quad ; \quad \mathbf{\Phi^{i+1}} = \mathbf{\Phi^i} + \delta\mathbf{\Phi^i}. \tag{A.13}$$

In the course of the present study we have implemented three types of numerical continuation

1. *Euler-Newton* continuation.
2. *Quadratic-predictor-Newton* continuation.
3. *Quadratic-predictor-Keller* continuation with some required modifications for tangent computations.

Euler-Newton continuation: Staring from the known solution $(\mathbf{\Phi_0}, \lambda_\mathbf{0})$ we predict the next solution as $\mathbf{\Phi^0} = \mathbf{\Phi_0} + (\mathbf{d\Phi}/\mathbf{d}\lambda)\delta\lambda$ and use it in A.13 as an initial guess. The derivative $(d\mathbf{\Phi}/\mathbf{d}\lambda = \mathbf{\Phi}_\lambda)$ can be computed using finite difference from the last two known solutions or by solving

$$\mathbf{J} \cdot \mathbf{\Phi}_\lambda = -\mathbf{F}_\lambda. \tag{A.14}$$

This procedure allow us to take large steps in λ when the solution is away from the turning points. But, at the turning points the Jacobian $\mathbf{J}$ becomes singular and therefore A.14 becomes unsolvable.

Quadratic-predictor-Newton continuation: To circumvent the singularity encountered at turning points we parametrize both $\mathbf{\Phi}$ and λ as a function of arc-length parameter s instead of parameterizing the solution $\mathbf{\Phi}$ by λ. Let s be the arc-length parameter and consider $\mathbf{\Phi}(s)$ and $\lambda(s)$ as a function of s. Now to advance the solution in parameter space from s_0 to s_1 we use the arc-length condition

$$\left\| \frac{\partial \mathbf{\Phi}}{\partial s} \right\|^2 + \left\| \frac{\partial \lambda}{\partial s} \right\|^2 = 1, \tag{A.15}$$

to compute a small increment $ds = \sqrt{\|d\mathbf{\Phi}\|^2 + \|d\lambda\|^2}$ along the solution curve. To start the quadratic predictor the first three initial solution points are obtained for three different but close values of λ. Neville's algorithm is used for polynomial interpolation, which gives a unique polynomial of degree 2 for three initial guesses. This polynomial can interpolate or extrapolate the solution along the solution branch. We predict the next point in the solution branch and use Newton-Krylov subspace method as a corrector. In this method we do not have to calculate the tangent vector along the branch and if started at some distance from the singular point this method can easily pass through the singular points to capture other branches. However, we have encountered some cases for which this method fails to work, specially during the continuation of large scale traveling waves with respect to the Smagorinsky constant C_s.

Quadratic-predictor-Keller Continuation: This method is the combination of Quadratic-predictor and Keller pseudo arc-length continuation (Chan & Keller (1982)). In this method, we take $\mathbf{\Phi}(s)$ and $\lambda(s)$ to be functions of the arc-length parameter s. Differentiation of $\mathbf{F}(\mathbf{\Phi}, \lambda) = \mathbf{0}$ with respect to s gives

$$\mathbf{F}_u \dot{\mathbf{\Phi}} + \mathbf{F}_\lambda \dot{\lambda} = 0. \tag{A.16}$$

We define the arc-length constraint as

$$\left\| \frac{\partial \mathbf{\Phi}}{\partial s} \right\|^2 + \left\| \frac{\partial \lambda}{\partial s} \right\|^2 = 1, \tag{A.17}$$

which when linearized reduces to the equation of a plane

$$\mathcal{N} \equiv (\mathbf{\Phi}(s) - \mathbf{\Phi}(s_0)) \cdot \dot{\mathbf{\Phi}}(s_0) + (\lambda(s) - \lambda(s_0)) \cdot \dot{\lambda}(s_0) - \triangle s = 0. \tag{A.18}$$

This plane is perpendicular to the tangent $(\dot{\mathbf{\Phi}}(s_0), \dot{\lambda}(s_0))$ at a distance $\triangle s$ from $(\mathbf{\Phi}(s_0), \lambda(s_0))$. Plane $\mathcal{N}$ intersect the solution curve $C(s)$ if the curvature of C is not too large and s is small enough. Newton's method is used to solve the following linear system at each iteration:

$$\begin{pmatrix} \mathbf{F}_u & \mathbf{F}_\lambda \\ \dot{\mathbf{\Phi}}(s_0) & \dot{\lambda}(s_0) \end{pmatrix} \begin{pmatrix} \triangle \mathbf{\Phi} \\ \triangle \lambda \end{pmatrix} = - \begin{pmatrix} \mathbf{F}(\mathbf{\Phi}, \lambda) \\ (\dot{\mathbf{\Phi}}(s) - \mathbf{\Phi}(s_0)) \cdot \dot{\mathbf{\Phi}}(s_0) + (\lambda(s) - \lambda(s_0)) \cdot \dot{\lambda}(s_0) - \triangle s \end{pmatrix}. \tag{A.19}$$

To mix quadratic predictor with Keller method we modified both of them. Let $\mathbf{\Phi}_2$, $\mathbf{\Phi}_1$ and $\mathbf{\Phi}_0$ be the three initial solutions to start the quadratic interpolation and s_2 , s_1 and s_0 are the corresponding arc-length coordinates. Let $\mathbf{\Phi}_{new}$ be the quadratic extrapolate and assume $\dot{\mathbf{\Phi}}_0$ and $\ddot{\mathbf{\Phi}}_0$ are the first and second order derivatives at $\mathbf{\Phi}_0$. We calculate derivatives using finite differences

$$\dot{\mathbf{\Phi}}_0 = \frac{\mathbf{\Phi}_0 - \mathbf{\Phi}_1}{s_0 - s_1} \quad ; \quad \ddot{\mathbf{\Phi}}_0 = \frac{1}{s_{new} - s_1} \left(\frac{\mathbf{\Phi}_{new} - \mathbf{\Phi_0}}{s_{new} - s_0} - \frac{\mathbf{\Phi}_0 - \mathbf{\Phi_1}}{s_0 - s_1} \right). \tag{A.20}$$

Using the information we have about the derivatives we use the Taylor series expansion to update the new initial guess as follows:

$$\mathbf{\Phi}_{new} = \mathbf{\Phi}_0 + \dot{\mathbf{\Phi}}_0 ds + \frac{1}{2} \ddot{\mathbf{\Phi}}_0 (ds)^2. \tag{A.21}$$

Similarly initial guesses for λ_{new} and $\dot{\lambda_0}$ can be obtained. We save tangent vectors and use them in equation A.19 at each Newton iteration. Among the three continuation techniques mentioned here, this method is found to be the most effective, as it apparently always passes smoothly through the singular points.

A.3 Linear Stability Analysis of Invariant Solutions

Let us write the evolution equation of our dynamical system as

$$\frac{d\mathbf{\Phi}}{dt} = \mathbf{F}(\mathbf{\Phi}). \tag{A.22}$$

Depending upon the type of invariant solution the linear stability investigation require certain modifications, however, the fundamental idea remains unchanged.

Equilibrium solutions: An infinitesimal pertubation ϕ' is added to the equilibrium solution $\mathbf{\Phi_0}$ and $\mathbf{F}$ is Taylor expanded near $\mathbf{\Phi}_0$.

$$\frac{d(\mathbf{\Phi}_0 + \phi')}{dt} = \mathbf{F}(\mathbf{\Phi}_0) + \frac{d\mathbf{F}}{d\mathbf{\Phi}}\Big|_{\mathbf{\Phi}_0} \phi' + O(\|\phi'\|^2). \tag{A.23}$$

Truncating at first order and considering that $\mathbf{F}$ and $d\mathbf{\Phi}/dt$ are zero at equilibrium point Φ_0, subsequently A.23 is reduced to

$$\frac{d\phi'}{dt} = \underbrace{\frac{d\mathbf{F}}{d\mathbf{\Phi}}\Big|_{\mathbf{\Phi}_0}}_{\mathcal{A}} \phi', \tag{A.24}$$

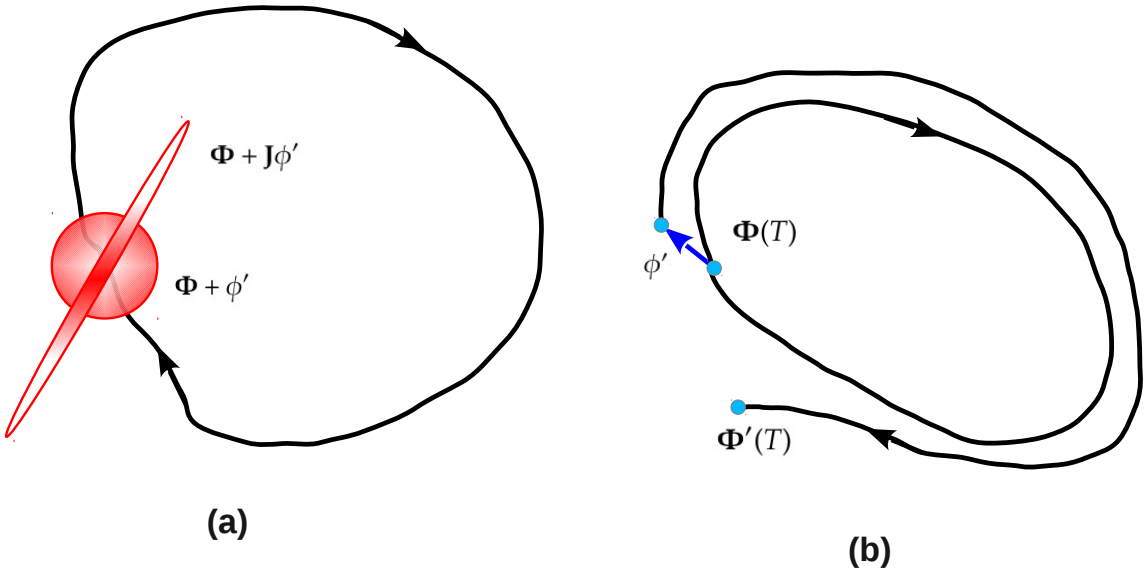

Figure A.1: Panel (a) : The Jacobian matrix **J** transform an infinitesimal neighborhood of **Φ** into an ellipsoid, with the diameter stretched along the unstable eigen direction $\psi^{(j)}$ of **J** by Floquet multiplier $\Lambda^{(j)}$. Panel (b): All the initial condition that are not confined to the center and stable manifold are repelled by an unstable periodic orbit. (see Cvitanovic *et al.* (2012))

where $\mathcal{A}$ is known as the stability matrix. Whether the pertubation amplitude $\|\phi'\|$ grows or decays with time depends upon the eigen spectrum of $\mathcal{A}$. Let us assume that $c^{(j)}$ are the eigenvalues of $\mathcal{A}$ and $\psi^{(j)}$ are the eigenvectors. The pertubation state vector can be expanded over the eigenvalue basis as $\phi'(t) = \sum_{j=0}^{N} q^{(j)}(t)\psi^{(j)}$, where components $q_j(t)$ are the modal amplitudes. Using modal expansion in A.24 and after some manipulation we get:

$$\phi'(t) = \underbrace{e^{\mathcal{A}t}}_{\mathbf{J}} \phi'(0), \tag{A.25}$$

where **J** is the Jacobian matrix also known as the propagator. The eigen values ($\Lambda^{(j)}$) of the propagator are called characteristic or Floquet multipliers and are related to the eigen values of stability matrix $\mathcal{A}$ as $\Lambda^j = e^{c_r^j + ic_i^j}$.

Periodic orbits: Another important class of invariant solutions is that of periodic orbits of period $T : \forall t : \mathbf{\Phi}(t+T) = \mathbf{\Phi}(t)$. When linearized about an arbitrary point lying on the trajectory we get $\phi'(t) = \mathcal{A}(t)\phi'$, where the stability matrix $\mathcal{A}$ has T periodicity i.e. $\mathcal{A}(t+T) = \mathcal{A}(t)$. Following a similar path as described in last section for equilibrium solutions (see Cvitanovic *et al.* (2012) for a detailed explanation.) $\phi'(t+T)$ is related to $\phi'(t)$ by :

$$\phi'(t+T) = \mathbf{J}(\mathbf{\Phi})\phi'(t). \tag{A.26}$$

Floquet multipliers of the Jacobian matrix $\mathbf{J}(\mathbf{\Phi})$ are independent of the starting point of the periodic orbit. If the Floquet multipliers $\Lambda^{(j)}$ of the Jacobian **J** are all distinct we can by denote $\psi^{(j)}$ the corresponding linearly independent Floquet vectors that satisfy:

$$\mathbf{J}\psi^{(j)} = \Lambda^{(j)}\psi^{(j)}. \tag{A.27}$$

The pertubation state vector can be expanded over the basis of Floquet vectors like $\phi'(t) = \sum_{j=0}^{N} q^{(j)}(t)\psi^{(j)}$, using this relation along with A.25 in A.24 gives:

$$q(t+T) = \Lambda^{(j)} q(t). \tag{A.28}$$

After m number of periods and taking the norm gives $||q(t+mT)|| = |\Lambda^{(j)}|^m ||q(t)||$. Hence the solution is linearly unstable if at least one Floquet multipliers $|\Lambda^{(j)}| > 1$, while linear stability requires that $|\Lambda^{(j)}| < 1$, i.e. all the Floquet multipliers lie inside the unit circle.

Appendix B

Codes used for DNS, LES and to find invariant solutions

B.1 CHANNELFLOW

`Channelflow` is a public domain code[1] primarily developed by J.F Gibson (Gibson *et al.*, 2008). In `channelflow` the Navier-Stokes equations are solved in terms of perturbations for a known laminar solution $U(y)\mathbf{i}_x$ associated to the base pressure gradient $P_x\mathbf{i}_x$. The total fields are therefore given by $\mathbf{u}(\mathbf{x},t) = U(y)i_x + \mathbf{u}'(\mathbf{x},t)$ and $p = P + p'$ and the Navier-Stokes equations are solved in the following form:

$$\frac{\partial \mathbf{u}'}{\partial t} + \mathbf{u}\cdot\nabla\mathbf{u} = -\nabla p + \nu\nabla^2\mathbf{u}' + \left[\nu\frac{\partial^2 U}{\partial y^2} - P_x\right] i_x. \tag{B.1}$$

These equations are spatially discretized using a Fourier-Chebyshev pseudospectral formulation. Dealiasing is used in the periodic directions with the 3/2 rule. A third-order accurate semi implicit scheme is used for time integration. We have verified that the same solutions are found with 2nd-order semi-implicit Crank-Nicolson, Runge-Kutta algorithm. During the simulations the CFL number was maintained in the range $[0.2 - 0.4]$.

Channelflow has its own subroutines to calculate invariant solutions and to perform their stability analysis and parameter continuation in plane Couette and Poiseuille flow. The routines implement the algorithm used by Viswanath (2007) which is based on a globally convergent Newton-Krylov subspace method which applies 'hookstep' trust-region adjustment to Newton steps.

B.2 DIABLO

`Diablo` is a public domain code developed at UC San Diego (Bewley *et al.*, 2001) which integrates both the Navier-Stokes and the LES equations. We have used `diablo` mainly to perform large-eddy simulations. A static Smagorinsky model is implemented in the LES module (see also Hwang & Cossu, 2010*c*, 2011). The damping function $D = 1 - \exp(-(y^+)^2/(A^+)^2)$, with $A^+ = 25$ is used to drive the eddy viscosity associated with the residual motions to zero at the wall. The Navier-Stokes and LES equations are discretized in space by a pseudo-spectral Fourier method in streamwise and spanwise directions and second-order accurate finite differences in the wall-normal direction. The grid in the wall normal direction is stretched by a hyperbolic tangent 'density' function to sufficiently resolve the near-wall region. Dealiasing is used in the periodic directions with 2/3 rule. The solutions are advanced in time by a fractional-step algorithm where the

[1] See `http://www.channelflow.org/dokuwiki/doku.php` for details.

nonlinear terms are explicit and integrated with a third-order Runge-Kutta method while the linear terms are implicit and are advanced using the second-order Crank-Nicolson method. During integrations we have kept the CFL number in the range [0.3 – 0.5].

The ability of `diablo` to accurately search for invariant solutions was tested by recomputing the travelling waves of Nagata (1990) and Waleffe (2003) in plane Couette flow and Itano & Toh (2001) in Poiseuille flow by using an edge-tracking bisection technique.

B.3 PEANUTS

`PEANUTS` is a Newton solver based on Krylov subspace methods implemented via the `PETSc` and `Slepc` libraries. These libraries make intensive use of parallel execution. A significant amount of work during this thesis has been devoted to interfacing this code with the DNS/LES integrators `channelflow` and `diablo`. In this process, we have kept PEANUTS separated from the DNS and LES codes, and essentially called them as external functions. PEANUTS requires a one dimensional (real) state vector. However ChannelFlow and Diablo deal with multidimensional representations of fields. Therefore, interfacing the codes requires the implementation of mapping from a multidimensional field view to one dimensional state vector (and conversely). Given the differences in representations used by the DNS/LES code, this turned out to be a rather difficult and time-consuming task.

Let us describe the 'state vector building' process in the case of relative periodic orbits, where we have three components of the velocity field, one scalar pressure field and four additional scalars: the time period T, the spanwise and streamwise shift $s_z = C_z T$ and $s_x = C_x T$ and the continuation parameter λ. The fields issued from DNS and LES can be stored in either physical space on in terms of (spatial) Fourier modes. We prefer the use of the spectral representation because of the fast convergence of higher harmonics. To start the DNS-LES simulation we need three velocity components and the pressure field at all the grid points. The continuity equation enables us to compute the third velocity component from the other two. The usual Poisson equation is used to compute the pressure field. Therefore we use only the streamwise (u) and spanwise (w) velocity fields to form the state vector. Let us continue the discussion focusing on `diablo`. Suppose N_x, N_y and N_z are the grid points in physical space and $\widehat{u}$, $\widehat{v}$, $\widehat{w}$ are the Fourier modes of the three velocity components in streamwise (x), wall normal (y) and spanwise (z) direction respectively. We save first the real part and then the imaginary part of the streamwise velocity followed by the real and imaginary part of the spanwise velocity. As `diablo` used 2/3 dealiasing rule the effective number of degrees of freedom (DOF) after dealiasing becomes $(1 + N_x/3)$ and $(1 + 2N_z/3)$ in streamwise and spanwise direction respectively. The no-slip boundary condition reduces the effective number of DOF in wall normal direction to $(N_y - 2)$. Therefore, the total number of modes becomes $4((1 + N_x/3) \times (Ny - 2) \times (1 + 2N_z/3))$, where the multiple 4 accounts for two velocity components and their real and imaginary part. In plane Couette and Poiseuille flow the imaginary part of the zero-zero harmonic modes $\widehat{u}(0, y, 0)$ and $\widehat{w}(0, y, 0)$ is zero, therefore the effective size of the state vector reduces to: $N_v = 4((1+N_x/3)\times(Ny-2)\times(1+2N_z/3)) - 2(N_y - 2)$ The additional four scalar unknowns are appended at the end of state vector $\mathbf{\Phi}$, making its effective length equal to $N_v + 4$.

In order to fix the spatial and temporal phases of the solution, as discussed in §2.5, we use the following three phase conditions stated by Viswanath (2007):

$$\left\langle \delta\mathbf{\Phi}_i, \frac{\partial \mathbf{\Phi}_i}{\partial x} \right\rangle = 0, \quad \left\langle \delta\mathbf{\Phi}_i, \frac{\partial \mathbf{\Phi}_i}{\partial z} \right\rangle = 0, \quad \left\langle \delta\mathbf{\Phi}_i, \frac{\partial \mathbf{\Phi}_i}{\partial t} \right\rangle = 0, \tag{B.2}$$

where the angle brackets represent the usual inner product. The two first conditions imply that the correction $\delta\mathbf{\Phi}_i$ done at each Newton iteration must be such that it does not translate $\mathbf{\Phi}_i$ in

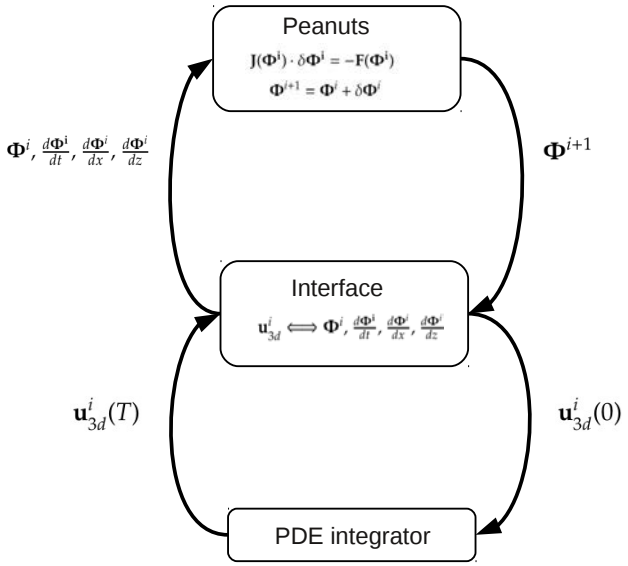

Figure B.1: Flowchart of PEANUTS integration with the PDE integrator

streamwise (x) and spanwise (z) direction. The third condition enforces that $\delta\mathbf{\Phi}_i$ is orthogonal to $\partial\mathbf{\Phi}_i/\partial t$ to ensure that the Newton correction is not a simple translation in time along the targeted periodic orbit.

Before attempting to use this code with the Navier-Stokes and LES solvers we have performed some tests on simple model equations. In particular, we have recomputed the periodic solution of Kuramoto-Sivashinsky equation reported by Lan & Cvitanovic (2008). The code has been further tested on phase-winding solutions of the Complex Ginzburg-Landau equation.

Finally, in order to test the `PEANUTS-diablo` interface we interpolated the invariant solution obtained by Gibson *et al.* (2008) to the `diablo` grid and sucessfully converged them. In the case of periodic orbits, our test case was on the Viswanath (2007) and Kawahara & Kida (2001) solutions. The stability analysis module of `PEANUTS-diablo` was also successfully tested against the already documented Floquet exponents of the Viswanath (2007) periodic orbits and the Nagata (1990) equilibrium solution.

Bibliography

ADRIAN, R. J. 2007 Hairpin vortex organization in wall turbulence. *Phys. Fluids.* **19**, 041301.

ADRIAN, R. J., MEINHART, C. D. & TOMKINS, C. D. 2000 Vortex organization in the outer region of the turbulent boundary layer. *J. Fluid. Mech.* **422**, 1–54.

DEL ÁLAMO, J. C. & JIMÉNEZ, J. 2003 Spectra of the very large anisotropic scales in turbulent channels. *Phys. Fluids* **15**, L41.

DEL ÁLAMO, J. C. & JIMÉNEZ, J. 2006 Linear energy amplification in turbulent channels. *J. Fluid Mech.* **559**, 205–213.

DEL ÁLAMO, J. C., JIMÉNEZ, J., ZANDONADE, P. & MOSER, R. D. 2004 Scaling of the energy spectra of turbulent channels. *J. Fluid Mech.* **500**, 135–144.

ANDERSSON, P., BRANDT, L., BOTTARO, A. & HENNINGSON, D. 2001 On the breakdown of boundary layers streaks. *J. Fluid Mech.* **428**, 29–60.

ARTUSO, R, AURELL, E & CVITANOVIC, P 1990 Recycling of strange sets: I. cycle expansions. *Nonlinearity* **3**, 325.

AVSARKISOV, V., HOYAS, S., OBERLACK, M. & GARCIA-GALACHE, J.P. 2014 Turbulent plane couette flow at moderately high reynolds number. *J. Fluid Mech.* **751**, R1.

BAMIEH, B. & DAHLEH, M. 2001 Energy amplification in channel flows with stochastic excitation. *Phys. Fluids* **13**, 3258–69.

BECH, K.H. & ANDERSSON, H.I. 1994 Very-large-scale structures in dns. In *Direct and Large-Eddy Simulation I* (ed. PeterR. Voke, Leonhard Kleiser & Jean-Pierre Chollet), pp. 13–24. Springer Netherlands.

BEWLEY, T.R. 2008 *Numerical Renaissance: Simulation, Optimization and Control*. San Diego (CA): Renaissance Press.

BEWLEY, T. R., MOIN, P. & TEMAM, R. 2001 DNS-based predictive control of turbulence: an optimal benchmark for feedback algorithms. *J. Fluid Mech.* **447**, 179–225.

BLACKWELDER, R. F. & KOVASZNAY, L. S. G. 1972 Time scales and correlations in a turbulent boundary layer. *Phys. Fluids.* **15**, 1545–1554.

BULLOCK, K. J., COOPER, R. E., & ABERNATHY, F. H. 1978 Structural similarity in radial correlations and spectra of longitudinal velocity fluctuations in pipe flow. *J. Fluid Mech.* **88**, 585–608.

BUTLER, K. M. & FARRELL, B. F. 1992 Three-dimensional optimal perturbations in viscous shear flow. *Phys. Fluids A* **4**, 1637–1650.

CHAN, T.F.C. & KELLER, H.B. 1982 Arc-length continuation and multi-grid techniques for nonlinear elliptic eigenvalue problems. *SIAM J. SCI. STAT. COMPUT.* **3**, 173–194.

CHANDLER, G.J. & KERSWELL, R.R. 2013 Invariant recurrent solutions embedded in a turbulent two-dimensional Kolmogorov flow. *J. Fluid Mech.* **722**, 554–595.

CLEVER, R.M. & BUSSE, F.H. 1997 Tertiary and quaternary solutions for plane Couette flow. *J. Fluid Mech.* **344**, 137–153.

CLEVER, R. M. & BUSSE, F. H. 1992 Three-dimensional convection in a horizontal fluid layer subjected to a constant shear. *J. Fluid Mech.* **234**, 511–527.

CORRSIN, S. & KISTLER, A. L. 1954 The free-stream boundaries of turbulent flows. *Technical Note* **3133**, 120–130, nACA.

COSSU, C., CHEVALIER, M. & HENNINGSON, D.S. 2010 Secondary optimal growth and subcritical transition in the plane Poiseuille flow. In *Seventh IUTAM Symposium on Laminar-Turbulent Transition* (ed. P. Schlatter & D.S. Henningson), pp. 129–134. Springer.

COSSU, C., L., BRANDT, BAGHERI, S. & HENNINGSON, D. S.. 2011 Secondary threshold amplitudes for sinuous streak breakdown. *Phys. Fluids* **23**, 074103.

COSSU, C., PUJALS, G. & DEPARDON, S. 2009 Optimal transient growth and very large scale structures in turbulent boundary layers. *J. Fluid Mech.* **619**, 79–94.

CVITANOVIC, P., ARTUSO, R., MAINIERI, R., TANNER, G. & VATTAY, G. 2012 *Chaos: Classical and Quantum*. Niels Bohr Institute, Copenhagen 2012.

CVITANOVIC, P. & GIBSON, J.F. 2010 Geometry of the turbulence in wall-bounded shear flows: periodic orbits. *Phys. Scr.* **T142**, 014007.

DEARDORFF, P. E. 1970 A numerical study of three-dimensional turbulent channel flow at large Reynolds numbers. *J. Fluid Mech.* **41**, 453–480.

DUGUET, Y., PRINGLE, C.C.T. & KERSWELL, R.R. 2008*a* Relative periodic orbits in transitional pipe flow. *Phys. Fluids* **20** (11), 114102.

DUGUET, Y., SCHLATTER, P. & HENNINGSON, D.S. 2009 Localized edge states in plane Couette flow. *Phys. Fluids* **21** (11), 111701.

DUGUET, Y., SCHLATTER, P., HENNINGSON, D.S. & ECKHARDT, B. 2012 Self-sustained localized structures in a boundary-layer flow. *Phys. Rev. Lett.* **108** (4), 044501.

DUGUET, Y., WILLIS, A. P. & KERSWELL, R. R. 2008*b* Transition in pipe flow: the saddle structure on the boundary of turbulence. *J. Fluid Mech.* **613**, 255–274.

ECKHARDT, B., SCHNEIDER, T.M., HOF, B. & WESTERWEEL, J. 2007 Turbulence Transition in Pipe Flow. *Ann. Rev. Fluid Mech.* **39**, 447.

EHRENSTEIN, U. & KOCH, W. 1991 Three-dimensional wavelike equilibrium states in plane Poiseuille flow. *J. Fluid Mech.* **228**, 111–148.

ELLINGSEN, T. & PALM, E. 1975 Stability of linear flow. *Phys. Fluids* **18**, 487.

FALCO, R. E. 1977 Coherent motions in the outer region of turbulent boundary layers. *Phys. Fluids* **20**, S124–S132.

FARRELL, B. F. & IOANNOU, P. J. 1993*a* Optimal excitation of three-dimensional perturbations in viscous constant shear flow. *Phys. Fluids* **5**, 1390–1400.

FARRELL, B. F. & IOANNOU, P. J. 1993*b* Stochastic forcing of the linearized Navier-Stokes equation. *Phys. Fluids A* **5**, 2600–9.

FARRELL, B. F. & IOANNOU, P. J. 1996 Generalized stability theory. *J. Atmos. Sci.* **53**, 2025–2053.

FLORES, O. & JIMÉNEZ, J. 2006 Effect of wall-boundary disturbances on turbulent channel flows. *J. Fluid Mech.* **566**, 357–376.

FLORES, O., JIMÉNEZ, J. & DEL ÁLAMO, J.C. 2007 Vorticity organization in the outer layer of turbulent channels with disturbed walls. *J. Fluid Mech.* **591**, 145–154.

GIBSON, J.F. & BRAND, E. 2014 Spanwise-localized solutions of planer shear flows. *J. Fluid Mech.* **745**, 25–61.

GIBSON, J. F., HALCROW, J. & CVITANOVIC, P. 2008 Visualizing the geometry of state space in plane Couette flow. *J. Fluid Mech.* **611**, 107–130.

GUALA, M., HOMMEMA, S. E. & ADRIAN, R. J. 2006 Large-scale and very-large-scale motions in turbulent pipe flow. *J. Fluid Mech.* **554**, 521–541.

GUSTAVSSON, L. H. 1991 Energy growth of three-dimensional disturbances in plane Poiseuille flow. *J. Fluid Mech.* **224**, 241–260.

HAMILTON, J.M., KIM, J. & WALEFFE, F. 1995 Regeneration mechanisms of near-wall turbulence structures. *J. Fluid Mech* **287**, 317–348.

HEAD, M. R. & BANDYOPADHYAY, P. 1981 New aspects of turbulent boundary-layer structure. *J. Fluid Mech* **107**, 297–338.

HERAULT, J., RINCON, F., COSSU, C., LESUR, G., OGILVIE, G. I. & LONGARETTI, P.Y. 2011 Periodic magnetorotational dynamo action as a prototype of nonlinear magnetic field generation in shear flows. *Phys. Rev. E* **84**, 036321.

HITES, M. H. 1997 Scaling of high-Reynolds number turbulent boundary layers in the national diagnostic facility. Ph. D. Thesis, Illinois Inst. of Technology.

HRISTOVA, H., ROCH, S., SCHMID, P. J. & TUCKERMAN, L. S. 2002 Transient growth in Taylor-Couette flow. *Phys. Fluids* **14** (10), 3475–3484.

HUTCHINS, N. & MARUSIC, I. 2007*a* Evidence of very long meandering features in the logarithmic region of turbulent boundary layers. *J. Fluid Mech.* **579**, 1–28.

HUTCHINS, N. & MARUSIC, I. 2007*b* Large-scale influences in near-wall turbulence. *Phil. Trans. R. Soc. A* **365**, 647–664.

HWANG, Y. 2013 Near-wall turbulent fluctuations in the absence of wide outer motions. *J. Fluid Mech.* **723**, 264–288.

HWANG, Y. & COSSU, C. 2010*a* Amplification of coherent streaks in the turbulent Couette flow: an input-output analysis at low Reynolds number. *J. Fluid Mech.* **643**, 333–348.

HWANG, Y. & COSSU, C. 2010*b* Linear non-normal energy amplification of harmonic and stochastic forcing in turbulent channel flow. *J. Fluid Mech.* **664**, 51–73.

HWANG, Y. & COSSU, C. 2010*c* Self-sustained process at large scales in turbulent channel flow. *Phys. Rev. Lett.* **105** (4), 044505.

HWANG, Y. & COSSU, C. 2011 Self-sustained processes in the logarithmic layer of turbulent channel flows. *Phys. Fluids* **23**, 061702.

ITANO, T. & TOH, S. 2001 The dynamics of bursting process in wall turbulence. *J. Phys. Soc. Jpn.* **70**, 703–716.

ITANO, T. & TOH, S. 2005 Interaction between a large-scale structure and near-wall structures in channel flow. *J. Fluid Mech.* **524**, 249–262.

JIMÉNEZ, J. 1998 The largest scales of turbulent wall flows. Annual research briefs. Center for Turbulence Research, Stanford University.

JIMÉNEZ, J. 2007 Recent developments on wall-bounded turbulence. *Rev. R. Acad. Cien. Serie A Mat.* **101**, 187–203.

JIMÉNEZ, J., DEL ÁLAMO, J.C. & FLORES, O. 2004 The large-scale dynamics of near-wall turbulence. *J. Fluid Mech.* **505**, 179–199.

JIMÉNEZ, J. & HOYAS, S. 2008 Turbulent fluctuations above buffer layer of wall-bounded flows. *J. Fluid Mech.* **611**, 215–236.

JIMÉNEZ, J., KAWAHARA, G., SIMENS, M. P., NAGATA, M. & SHIBA, M. 2005 *Phys. Fluids* **17**, 015105.

JIMÉNEZ, J. & MOIN, P. 1991 The minimal flow unit in near-wall turbulence. *J. Fluid Mech.* **225**, 213–240.

JIMÉNEZ, J. & PINELLI, A. 1999 The autonomous cycle of near-wall turbulence. *J. Fluid Mech.* **389**, 335–359.

JOVANOVIĆ, M. R. & BAMIEH, B. 2005 Componentwise energy amplification in channel flow. *J. Fluid Mech.* **543**, 145–83.

KAWAHARA, G. & KIDA, S. 2001 Periodic motion embedded in plane Couette turbulence: regeneration cycle and burst. *J. Fluid Mech.* **449**, 291–300.

KAWAHARA, G., UHLMANN, M. & VEEN, L. VAN 2012 The significance of simple invariant solutions in turbulent flows. *Annu. Rev. Fluid Mech.* **44**, 203–225.

KENDALL, J. M. 1985 Experimental study of disturbances produced in a pre-transitional laminar boundary layer by weak free-stream turbulence. *AIAA Paper* **85**, 1695.

KERSWELL, R. R. 2005 Recent progress in understanding the transition to turbulence. *Nonlinearity* **18**, R17–R44.

KERSWELL, R. R. & TUTTY, O.R. 2007 Recurrence of travelling waves in transitional pipe flow. *J. Fluid Mech.* **584**, 69–102.

KHAPKO, T., KREILOS, T., SCHLATTER, P., DUGUET, Y., ECKHARDT, B. & HENNINGSON, D. S. 2013 Localized edge states in the asymptotic suction boundary layer. *J. Fluid. Mech.* **R6**, 717.

KIM, J, MOIN, P & MOSER, R 1987 Turbulence statistics in fully developed channel flow at low Reynolds number. *J. Fluid Mech.* **177**, 133–166.

KIM, K. C. & ADRIAN, R. 1999 Very large-scale motion in the outer layer. *Phys. Fluids* **11** (2), 417–422.

KIM, W.W & MENON, S. 1999 An unsteady incompressible navier-stokes solver for large eddy simulation of turbulent flows. *Int. J. Numer. Meth. Fluids* **31**, 983–1017.

KITOH, O., NAKABAYASHI, K. & NISHIMURA, F. 2005 Experimental study on mean velocity and turbulence characteristics of plane Couette flow: low-Reynolds-number effects and large longitudinal vortical structures. *J. Fluid Mech.* **539**, 199.

KITOH, O. & UMEKI, M. 2008 Experimental study on large-scale streak structure in the core region of turbulent plane Couette flow. *Phys. Fluids* **20**, 025107.

KLINE, S. J., REYNOLDS, W. C., SCHRAUB, F. A. & RUNSTADLER, P. W. 1967 The structure of turbulent boundary layers. *J. Fluid Mech.* **30**, 741–773.

KOMMINAHO, J., LUNDBLADH, A. & JOHANSSON, A. V. 1996 Very large structures in plane turbulent Couette flow. *J. Fluid Mech.* **320**, 259–285.

KOVASZNAY, L. S. G., KIBENS, V. & BLACKWELDER, R. F. 1970 Large-scale motion in the intermittent region of a turbulent boundary layer. *J. Fluid Mech.* **41**, 283–325.

KREILOS, T. & ECKHARDT, B. 2012 Periodic orbits near onset of chaos in plane Couette flow. *Chaos* **22** (4), 047505.

KREILOS, T., VEBLE, G., SCHNEIDER, T. M. & ECKHARDT, B. 2013 Edge states for the turbulence transition in the asymptotic suction boundary layer. *J. Fluid Mech.* **726**, 100–122.

LAN, Y. & CVITANOVIC, P. 2008 Unstable recurrent pattern in kuramoto-sivashinsky dynamics. *Phys. Rev. E.* **78**, 026208.

LANDAHL, M. T. 1980 A note on an algebraic instability of inviscid parallel shear flows. *J. Fluid Mech.* **98**, 243–251.

LANDAHL, M. T. 1990 On sublayer streaks. *J. Fluid Mech.* **212**, 593–614.

LANGTON, CHRIS G. 1990 Computation at the edge of chaos: Phase transtions and energent computation. *Physica D* (42), 12–37.

LEE, M. J. & KIM, J. 1991 The structure of turbulence in a simulated plane Couette flow. In *Eighth Symp. on Turbulent Shear Flow*, pp. 5.3.1–5.3.6. Tech. University of Munich, Sept. 9-11.

MARUSIC, I. 2001 On the role of large-scale structures in wall turbulence. *Phys. Fluids* **13**, 735.

MARUSIC, I., MATHIS, R. & HUTCHINS, N. 2010 Predictive model for wall-bounded turbulent flow. *Science* **329** (5988), 193–196.

MASON, P.J. & CALLEN, N.S. 1986 On the magnitude of the subgrid-scale eddy coefficient in large-eddy simulations of turbulent channel flow. *J. Fluid Mech.* **162**, 439–462.

MATHIS, R., HUTCHINS, N. & MARUSIC, I. 2009 Large-scale amplitude modulation of the small-scale structures in turbulent boudnary layers. *J. Fluid. Mech.* **628**, 311–337.

MATSUBARA, M. & ALFREDSSON, P. H. 2001 Disturbance growth in boundary layers subjected to free stream turbulence. *J. Fluid. Mech.* **430**, 149–168.

McKeon, B. J., Swason, C.J., Zagarola, M. V., Donnely, R.J. & Smits, A. J. 2004 Friction factor for smooth pipe flow. *J. Fluid Mech.* **501**, 41.

Moffatt, H. K. 1967 The interaction of turbulence with strong wind shear. In *Proc. URSI-IUGG Coloq. on Atoms. Turbulence and Radio Wave Propag.* (ed. A.M. Yaglom & V. I. Tatarsky), pp. 139–154. Moscow: Nauka.

Nagata, M. 1990 Three-dimensional finite-amplitude solutions in plane Couette flow: bifurcation from infinity. *J. Fluid Mech.* **217**, 519–527.

Orszag, S. A. 1971 Accurate solution of the Orr–Sommerfeld stability equation. *J. Fluid Mech.* **50**, 689–703.

Orszag, S. A. & Patera, A. T. 1983 Secondary instability of wall-bounded shear flows. *J. Fluid Mech.* **128**, 347–385.

Park, J., Hwang, Y. & Cossu, C. 2011 On the stability of large-scale streaks in turbulent Couette and Poiseulle flows. *C. R. Méc.* **339**, 1–5.

Patel, V. C. & Head, R. 1969 Some observations on skin friction and velocity profiles in fully developed pipe and channel flows. *J. Fluid Mech.* **38**, 181–201.

Pope, S. B. 2000 *Turbulent flows*. Cambridge, UK: Cambridge U. Press.

Pringle, C. C. T. & Kerswell, R. R. 2007 Asymmetric, helical, and mirror-symmetric traveling waves in pipe flow. *Phys. Rev. Lett.* **99**, 207450.

Pujals, G., Cossu, C. & Depardon, S. 2010*a* Forcing large-scale coherent streaks in a zero pressure gradient turbulent boundary layer. *J. Turb.* **11** (25), 1–13.

Pujals, G., Depardon, S. & Cossu, C. 2010*b* Drag reduction of a 3D bluff body using coherent streamwise streaks. *Exp. Fluids* **49** (5), 1085–1094.

Pujals, G., García-Villalba, M., Cossu, C. & Depardon, S. 2009 A note on optimal transient growth in turbulent channel flows. *Phys. Fluids* **21**, 015109.

Rawat, S., Cossu, C. & Rincon, F. 2013 Relative periodic orbits in plane Poiseuille flow. In *Advances in Turbulence XIV: Proceedings of the 14th European Turbulence Conference, Lyon, France*. Springer.

Rawat, S., Cossu, C. & Rincon, F. 2014 Relative periodic orbits in plane Poiseuille flow. *C. R. Méc.* **342**, 485–489.

Reddy, S. C. & Henningson, D. S. 1993 Energy growth in viscous channel flows. *J. Fluid Mech.* **252**, 209–238.

Reddy, S. C., Schmid, P. J., Baggett, J. S. & Henningson, D. S. 1998 On the stability of streamwise streaks and transition thresholds in plane channel flows. *J. Fluid Mech.* **365**, 269–303.

Reddy, S. C., Schmid, P. J. & Henningson, D. S. 1993 Pseudospectra of the Orr-Sommerfeld operator. *SIAM J. Appl. Math.* **53**, 1547.

Reynolds, W. C. & Hussain, A. K. M. F. 1972 The mechanics of an organized wave in turbulent shear flow. Part 3. Theoretical models and comparisons with experiments. *J. Fluid Mech.* **54** (02), 263–288.

RINCON, F., OGILVIE, GI & PROCTOR, MRE 2007*a* Self-Sustaining Nonlinear Dynamo Process in Keplerian Shear Flows. *Phys. Rev. Lett.* **98** (25), 254502.

RINCON, F., OGILVIE, G. I. & COSSU, C. 2007*b* On self-sustaining processes in Rayleigh-stable rotating plane Couette flows and subcritical transition to turbulence in accretion disks. *Astron. & Astrophys* **463**, 817–832.

RINCON, F., OGILVIE, G. I., PROCTOR, M. R. E. & COSSU, C. 2008 Subcritical dynamos in shear flows. *Astron. Nashr.* **329**, 750–761.

RIOLS, A., RINCON, F., COSSU, C., LESUR, G., LONGARETTI, P.-Y., OGILVIE, G.I. & HERAULT, J. 2013 Global bifurcations to subcritical magnetorotational dynamo action in Keplerian shear flow. *J. Fluid Mech.* **731**, 1–45.

RIOLS, A., RINCON, F., COSSU, C., LESUR, G., OGILVIE, G. I. & LONGARETTI, P. 2014 Dissipative effects on the sustainment of a magnetorotational dynamo in Keplerian shear flow. *ArXiv e-print 1410.3406* .

SCHLICHTING, H. 1979 *Boundary-Layer Theory*. New York: Mc Graw-Hill.

SCHMID, P.J. & HENNINGSON, D. S. 1994 Optimal energy density growth in Hagen–Poiseuille flow. *J. Fluid Mech.* **277**, 197–225.

SCHMID, P. J. & HENNINGSON, D. S. 2001 *Stability and Transition in Shear Flows*. New York: Springer.

SCHNEIDER, T.M., GIBSON, J.F., LAGHA, M., DE LILLO, F. & ECKHARDT, B. 2008 Laminar-turbulent boundary in plane Couette flow. *Phys. Rev. E* **78**, 37301.

SCHNEIDER, T. M., ECKHARDT, B. & VOLLMER, J. 2007 Statistical analysis of coherent structures in transitional pipe flow. *Phys. Rev. E* **75**, 066313.

SCHOPPA, W. & HUSSAIN, F. 2002 Coherent structure generation in near-wall turbulence. *J. Fluid Mech.* **453**, 57–108.

SKUFCA, J.D., YORKE, J.A. & ECKHARDT, B. 2006 Edge of Chaos in a Parallel Shear Flow. *Phys. Rev. Lett.* **96** (17), 174101.

SMAGORINSKY, J. 1963 General circulation experiments with the primitive equations: I. the basic equations. *Mon. Weather Rev.* **91**, 99–164.

SMITH, J. R. & METZLER, S. P. 1983 The characteristics of low-speed streaks in the near-wall region of a turbulent boundary layer. *J. Fluid Mech.* **129**, 27–54.

STROGATZ, S. 2001 *Nonlinear dynamics and chaos: with applications to physics, biology, chemistry and engineering*. Perseus Books Group.

TILLMARK, N. & ALFREDSSON, H. 1994 Structures in turbulent plane Couette flow obtained from correlation measurements. In *Advances in Turbulences V* (ed. R. Benzi), pp. 502–507. Kluwer.

TOH, S. & ITANO, T. 2003 A periodic-like solution in channel flow. *J. Fluid Mech.* **481**, 67–76.

TOMKINS, C. D. & ADRIAN, R. J. 2003 Spanwise structure and scale growth in turbulent boundary layers. *J. Fluid Mech.* **490**, 37–74.

TOMKINS, C. D. & ADRIAN, R. J. 2005 Energetic spanwise modes in the logarithmic layer of a turbulent boundary layer. *J. Fluid Mech.* **545**, 141–162.

TOWNSEND, A. 1976 *The structure of turbulent shear flow*. Cambridge, UK: Cambridge U. Press, second edition.

TREFETHEN, L. N., TREFETHEN, A. E., REDDY, S. C. & DRISCOLL, T. A. 1993 A new direction in hydrodynamic stability: Beyond eigenvalues. *Science* **261**, 578–584.

TSUKAHARA, T., KAWAMURA, H. & SHINGAI, K. 2006 DNS of turbulent Couette flow with emphasis on the large-scale structure in the core region. *J. Turbulence.* **42**.

TUCKERMAN, L. S. & BARKLEY, D. 1988 Global bifurcation to travelling waves in axisymmetric convection. *Phys. Rev. Lett.* **61**, 408–411.

VISWANATH, D. 2007 The dynamics of transition to turbulence in plane Couette flow. *ArXiv physics/0701337* .

VISWANATH, D. 2008 The dynamics of transition to turbulence in plane couette flow. In *Mathematics and Computation, a Contemporary View* (ed. Hans Munthe-Kaas & Brynjulf Owren), *Abel Symposia*, vol. 3, pp. 109–127. Springer Berlin Heidelberg.

WALEFFE, F. 1995 Hydrodynamic stability and turbulence: Beyond transients to a self-sustaining process. *Stud. Appl. Math.* **95**, 319–343.

WALEFFE, F. 1997 On a self-sustaining process in shear flows. *Phys. Fluids* **9**, 883–900.

WALEFFE, F. 1998 Three-dimensional coherent states in plane shear flows. *Phys. Rev. Lett.* **81**, 4140–4143.

WALEFFE, F. 2001 Exact coherent structures in channel flow. *J. Fluid Mech.* **435**, 93–102.

WALEFFE, F. 2003 Homotopy of exact coherent structures in plane shear flows. *Phys. Fluids* **15**, 1517–1534.

WEDIN, H. & KERSWELL, R.R. 2004 Exact coherent structures in pipe flow: travelling wave solutions. *J. Fluid Mech.* **508**, 333–371.

WILLIS, A. P., HWANG, Y. & COSSU, C. 2010 Optimally amplified large-scale streaks and drag reduction in the turbulent pipe flow. *Phys. Rev. E* **82**, 036321.

ZAMMERT, S. & ECKHARDT, B. 2013 Periodically bursting edge state in poiseuille flow. *Fluid Dyn. Res.* **46**, 041419.

ZHOU, J., ADRIAN, R. J., BALACHANDAR, S. & KENDALL, T. M. 1999 Mechanisms for generating coherent packets of hairpin vortices in channel flow. *J. Fluid. Mech.* **387**, 353–396.